SYNTHESIS AND CHARACTERIZATION OF GRAPHENE-GOLD NANOCOMPOSITE COUNTER ELECTRODES FOR DYE-SENSITIZED SOLAR CELL APPLICATION

PAUL KIMEU NGUMBI

DOCTOR OF PHILOSOPHY

(Physics)

JOMO KENYATTA UNIVERSITY OF

AGRICULTURE AND TECHNOLOGY

2021

Synthesis and Characterization of Graphene-Gold Nanocomposite Counter Electrodes for Dye-Sensitized Solar Cell Application

Paul Kimeu Ngumbi

A thesis submitted in partial fulfillment of the requirements for the degree of Doctor of Philosophy in Physics of the Jomo Kenyatta University of Agriculture and Technology

2021

DECLARATION

This thesis is my original work and has not been presented for a degree in any other university.

Signature:.....……..…..... Date .....……...…

Paul Kimeu Ngumbi

This thesis has been submitted for examination with our approval as university supervisors.

Signature:.....……..…..... Date .....……...…

Dr. Simon W. Mugo, (PhD)

JKUAT, Kenya

Signature:.....……..…..... Date .....……...…

Dr. James M. Ngaruiya, (PhD)

JKUAT, Kenya

Signature:.....……..…..... Date .....……...…

Prof. Cecil K. King'ondu, (PhD)

SEKU, Kenya

DEDICATION

To my dad the late Bernard Ngumbi and my mum the late Agatha Mbeni.

ACKNOWLEDGEMENT

I would like to thank the Almighty God for granting me the strength and resources to go through my studies. “May your name be glorified”.

The work culminating in this thesis results from much support received from the many people with whom I interacted. Firstly, I thank JKUAT for granting me the opportunity to pursue this program through my advisors, Dr. Simon Mugo, Dr. James Ngaruiya and Prof. Cecil King’ondu. As a knowledgeable team, you introduced me to the fields of nanotechnology and provided guidance throughout my research period. Thank you for setting for me high standards in research work and ethics. You inspired and encouraged me to keep going forward even during the highs of challenges. You never gave up on me even when times presented it as the only option. To the staff at the Physics department, JKUAT, I say “Thank you for the many fruitful progress seminars which shaped my work”. Special thanks to all technical staff at the Physics, Chemistry, Food Science and Clinical Chemistry labs in JKUAT for your support during UV-Vis spectroscopy, optical microscopy, nanoparticles synthesis, and sample annealing processes. You were so generous and brotherly in sharing your time and ideas. To the graduate students at the school of Physical Sciences, the jokes we cracked during the many lab hours made life simpler.

The accomplishment of this work would not have been possible without the unending moral support and motivation from my siblings. You always encouraged me to be optimistic into the future even during the most stressful times. Thank you my dear wife Betty, and my lovely children. You endured the countless days I was too busy for you, the strained finances and dull moments over the study period. Your love and support is immeasurable. To all who believed in me, and who kept asking me when it would be over, I say “Thank you. It was worth”. To Sr. Anna, Thank you for faithful prayers.

I would like to thank the National Research Fund (NRF) of Kenya for supporting this research through Grant Grant No.: NACOSTI/RCD/ST&I/7TH CALL/PhD/088.

TABLE OF CONTENTS

LIST OF TABLES

LIST OF FIGURES

LIST OF APPENDICES

LIST OF ABBREVIATIONS AND ACRONYMS

0-D	Zero-dimensional
1-D	One-dimensional
2-D	Two-dimensional
3-D	Three-dimensional
AM	Air Mass
AuNPs	Gold Nanoparticles
CB	Conduction Band (s)
C_D	Optical Contrast Difference
C_R	Reflection Optical Contrast
C_T	Transmission Optical Contrast
CE	Counter Electrode
CNT	Carbon Nanotube
CVD	Chemical Vapor Deposition
DFM	Dark Field Microscopy
DI water	Deionized Water
DSSC	Dye-Sensitized Solar Cell
FF	Fill Factor
FLG	Few-Layer Graphene
FTIR	Fourier Transform Infrared Spectroscopy
FTO	Fluorine-doped Tin Oxide ($F:SnO_2$)
FWHM	Full Width at Half Maximum

Gr	Graphene
HOMO	Highest Occupied Molecular Orbital
HOPG	Highly Oriented Pyrolytic Graphite
IR	Infrared Band
LSPR	Localized Surface Plasmon Resonance
LUMO	Lowest Unoccupied Molecular Orbital
MLG	Multi-Layer Graphene
NREL	National Renewable Energy Laboratory (USA)
PA	Photoanode
PCE	Power Conversion Efficiency
PV	Photovoltaic
PVD	Physical Vacuum Deposition
QD	Quantum Dot
Ru	Ruthenium
SEM	Scanning Electron Microscopy
SLG	Single-Layer Graphene
SnO_2	Tin (IV) Oxide
TCO	Transparent Conducting Oxides
TEM	Transmission Electron Microscopy
TiO_2	Titanium Dioxide (Titania)
UV	Ultraviolet Region
VB	Valence Band

Vis	Visible Band
WE	Working Electrode
XRD	X-ray Diffraction

LIST OF SYMBOLS

T_a	Absolute temperature
$\pi\alpha$	Absorbance
a.u	Absorbance units
ω	Angular frequency
a_b^*	Bohr exciton radius
a_b	Bohr radius of hydrogen atom
k_B	Boltzmann constant $(1.38\times10^{-23} m^2 kg.s^{-2}K^{-1})$
J	Current density
J_{pm}	Current density at maximum power
γ	Damping coefficient
ε	Dielectric constant
ε_m	Dielectric constant of the medium
K	Dirac points
N719	di-tetrabutylammonium cis-bis(isothiocyanato) bis(2,2'-bipyridyl-4,4'-dicarboxylato)ruthenium(II)
ω_{sp}	Drude surface plasmon frequency
ΔV_{redox}	Electrolyte redox potential
q	Electron charge $(1.602\times10^{-19} C)$
$\mathbf{e^-/h^+}$	Electron/hole pairs
m_e	Electron rest mass

eV	Electron volt ($=1.6\times10^{-19}$ Joules)
E_g	optical band gap energy
S^*	Excited dye
C_{ext}	Extinction coefficient
E_F	Fermi energy level
ν	Frequency of photon
$\mathbf{HAuCl_4 \cdot 3H_2O}$	Gold (III) Chloride trihydrate (Chloroauric acid-$HAuCl_4$)
$\varepsilon_{\mathrm{Im}}$	Imaginary parts of the dielectric function
I_O	Intensity of incident signal
I_T	Intensity of transmitted signal
$\pi-\pi^*$	intra-band transitions
$\sigma-\sigma^*$	inter-band transitions
I^- / I_3^-	Iodide/triiodide redox couple
η	Light-to-electric energy conversion efficiency
P_{max}	Maximum power
C	Molar concentration
Ω/sq	Ohms/square
V_{oc}	Open circuit voltage
σ	Optical conductivity
S^+	Oxidized dye
$h\nu$	Photon energy

π	Pi- bonds
a_0	QD radius
Φ	Radiant flux
ε_{Re}	Real parts of the dielectric function
m^*	Reduced mass of exciton system
R	Reflectance
J_0	Reverse saturation current density
R_y	Rydberg energy
J_{sc}	Short circuit current density
$Na_3C_6O_7.2H_2O$	Sodium citrate tribasic dihydrate (Trisodium citrate-Na_3Ctr)
T	Transmittance
S	Unexcited dye
σ_0	Universal optical conductivity
V_{pm}	Voltage at maximum power
λ	Wavelength

ABSTRACT

With the increasing global demand for alternative energy, photovoltaic (PV) technology has undergone remarkable evolution extending over four PV generations. Currently, dye-sensitized solar cells (DSSCs), which fall within the 3rd generation are more versatile and relatively less costly compared to the dominant crystalline silicon (Si) technologies. These DSSCs bear the hope of becoming the future solution to the energy crisis. However, the poor catalysis within the electrodes makes DSSCs relatively inefficient hence ineffective for full commercial utilization. This study investigated the use of composite counter electrodes (CEs) by incorporating graphene (Gr) and/or plasmonic gold (Au) nanoparticles (NPs) with the aim to improve the efficiency of the conventional platinum (Pt) based DSSCs. Gold nanoparticles (AuNPs) in colloidal form with an average size of ~12 nm were prepared by chemical reduction method. The size evaluation was done using the resulting localized surface plasmon resonance (LSPR) peak wavelength values (518-520 nm) based on the UV-Vis spectra data. Graphene modules prepared by chemical vapor deposition (CVD) on a glass/Fluorine-doped tin oxide (FTO) were used as electrode substrates in this work. These modules depicted G and 2D bands at 1380 and 1700 cm^{-1} respectively under Raman spectroscopy, indicating low defect state of the Gr. Four different sets of composite CE modules namely FTO/Pt (CE1), FTO/Gr/Pt (CE2), FTO/Gr/AuNPs (CE3) and FTO/Gr/AuNPs/Pt (CE4) were prepared. The CEs recorded transmittance above 70% under UV-Vis spectroscopy, meeting requirements for back-electrode application in DSSCs. Photoanode (PA) modules consisting of titanium dioxide (TiO_2) on the FTO/Gr substrate were prepared by the doctor-blade method. Three DSSC modules were assembled based CEs CE2, CE3 and CE4 and their PV performance compared to the reference cell based on CE1. Both Gr and AuNPs were found to possess PV properties and enhanced the resulting DSSCs by 13.4 and 10.1% respectively. The DSSCs containing Pt (CE1, CE2, and CE4) performed better in terms of power conversion efficiency (PCE) due to the increased short circuit current densities (J_{sc}) and fill factors (*FF*). However, change in the open-circuit voltage (V_{oc}) was negligible. The CE4 based cell design presented the best PCE at 4.62%, In this composite DSSC, the J_{sc} (9.92 mA/cm^2), V_{oc} (0.68 V) and *FF* (0.69) values recorded representing 13.9%, 0.8% and 9.0% increase respectively compared to CE1. This represented a 24.9% PCE enhancement, which is the synergistic effect of Gr and AuNPs as a composite. This remarkable performance could be due to increased electrocatalytic activity resulting from the graphene matrix within the electrodes. It is also partly attributed to the suppressed carrier recombination resulting from the LSPR property of the Au contacts anchored on the Gr surface in the CE structure.

CHAPTER ONE

INTRODUCTION

1.1 Background

Today, conventional fuels which include natural gases, coal, petroleum, and other liquids, form the major sources of the global energy matrix (IEO, 2018). Figure 1.1 shows world energy consumption history and projection by source between the years 1990-2040.

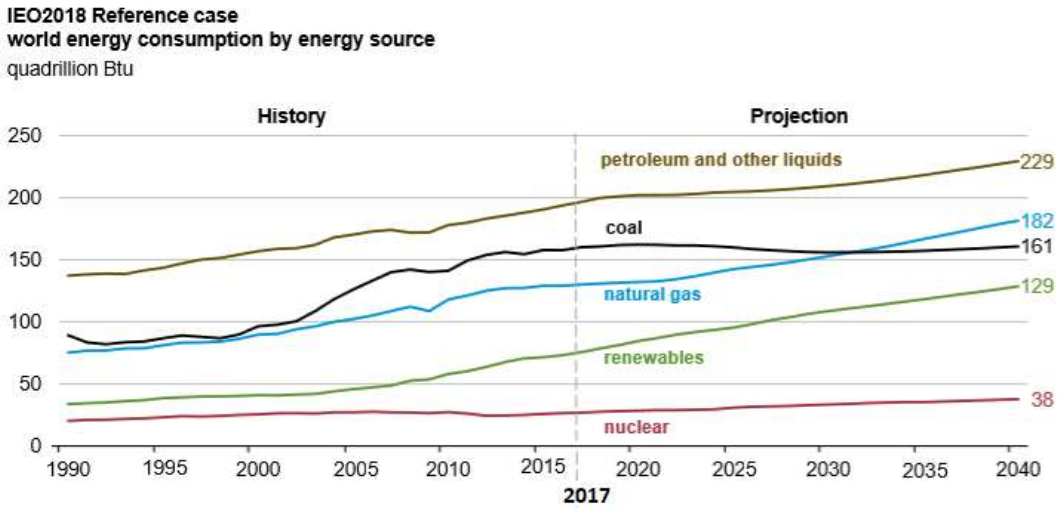

Figure 1.1: World energy consumption history and projection by source, 1990-2040 (Source: IEO, 2018).

With the world's ballooning population and economic development, the annual energy consumption continues to increase, with a projection of >700 quadrillion British thermal units (Btu) from the combined sources, an equivalent of 0.74 billion Terajoules (TJ) by 2040 (IEO, 2018). To generate energy equivalent to this world's annual consumption, about 22.7 billion tons of the non-regenerate and environmentally unfriendly fossil fuels would be required. The increasing global awareness of environmental pollution resulting from the combustion of these fossil fuels makes it indispensable for scientists to develop and promote alternative clean energy sources to lower its overdependence (Perera, 2018).

Solar energy stands out in most parts of the world as one of the best prospective candidates to meet the increasing energy demand. The amount of solar radiant energy that strikes the Earth's surface approximates to 3.9×10^{24} J/year (Wu *et al.*, 2008). This implies that, if all the sun's energy was to be harnessed, a one hour of insolation can supply enough energy to meet global human energy requirements for nearly one year. This amount of annual energy need can be extracted from the solar spectrum that reaches the earth's surface through the atmospheric gases (Zayat *et al.*, 2007) as shown in Figure 1.2.

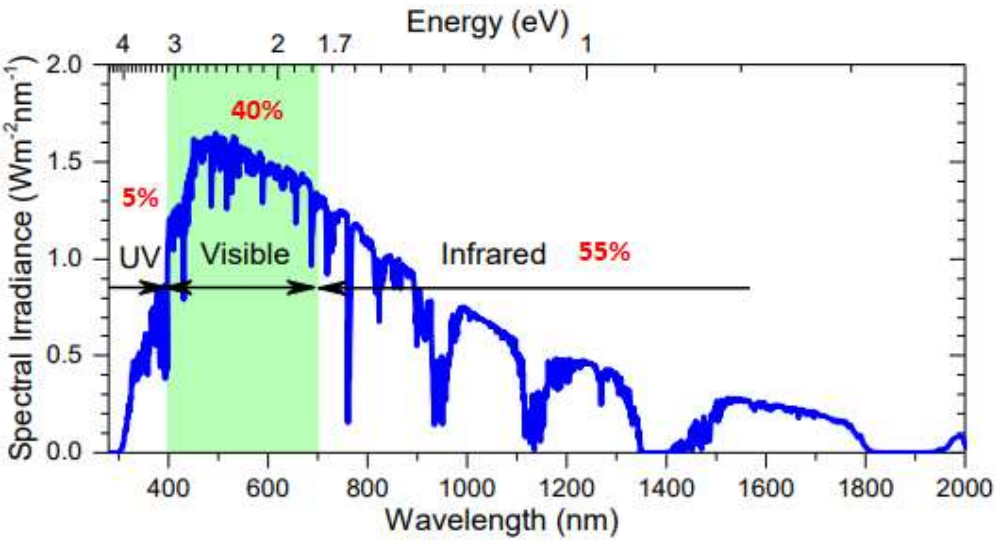

Figure 1.2: Solar spectrum reaching the earth's surface through the atmospheric gases (Source: Zayat *et al.*, 2007).

Figure 1.2 demonstrates that the most intense part of the spectrum is the visible light and makes up to 40% of the spectrum while around 55% of the radiation lies in the infrared region (Zayat *et al.*, 2007). Since solar energy is highly abundant, PV systems could provide enough global energy. Such systems must encompass new and novel materials for optimum harnessing of the energy over a wider range of the solar spectrum.

1.2 Statement of the Problem

The growing global environmental and energy challenge has created the need for green energy sources. The increasing research focus and fruition of DSSCs technology over the existing solid-state silicon cells arise from their reduced cost. Although there has been a remarkable cost reduction, researchers are currently working towards increasing the energy harvesting efficiency of the cells. Studies on improving structural designs and material engineering in the dominant Pt-based DSSCs are in progress. However, the reported efficiencies are quite low. This is due to the poor catalytic activity at the CE leading to reduced carrier regeneration and transport within the cell. To improve this efficiency, enhancing the efficiency of electron injection and reducing charge recombination within the SC structure is essential, in addition to increasing light concentration for maximum harvesting. Modifying the Pt-based CE to form a composite with other novel materials could improve its PV properties. This study aimed at synthesizing Gr/AuNPs nanocomposite as an interface for FTO and Pt within a DSSC CE, and hence evaluate the contribution of each component material to the overall performance of resulting DSSCs.

1.3 Justification of the Study

With the rising global demand for renewable energy, the key to its availability lies within the nanotechnology space. Dye-sensitized SCs, prospectively, could offer a viable solution, although the present DSSCs have fundamental challenges of low efficiency. To unlock this path, graphene and metallic NPs are at the center of research. Although most studies on graphene application in PVs have largely been prospective, they show that graphene can be engineered using metallic NPs. Contacting graphene with Pt and AuNPs could generate composite nanostructures with improved solar energy harvesting properties. Their structural and design modification could result in increased efficiencies.

Within the CE, the presence of graphene will enhance catalytic activity of the cell due to its excellent conductivity, (Rasheed *et al.*, 2016) hence improving charge transport with reduced electron-hole recombination within the DSSC. Moreover, its

thermal and mechanical stability allows the resulting devices to function under increased temperature without impairing their charge regeneration. Such material combination is an alternative to the overdependence on Si or bare Pt DSSCs, which are expensive and at the limit of miniaturization. Consequently, such graphene and plasmonic-based SCs, are projected to have higher efficiencies and simplicity in production.

1.4 Objectives

1.4.1 General Objective

To fabricate, characterize, and evaluate the performance of graphene-gold nanocomposite counter electrodes for dye-sensitized SCs applications.

1.4.2 Specific Objectives

1. To exfoliate graphene and evaluate the number of layers by optical microscopy.
2. To synthesize citrate reduced colloidal gold and determine nanoparticle size using UV-Vis spectroscopy.
3. To fabricate platinum, gold nanoparticles and graphene nanocomposites counter electrodes and evaluate their performance in DSSCs.
4. To assemble nanocomposite counter electrode-based DSSCs and evaluate the effect of graphene and gold nanoparticles in the DSSC photovoltaic performance.

1.5 Significance of the Study

This study aims at providing an alternative approach to fabrication of DSSCs with improved solar energy harvesting efficiency. This improvement could be achieved by utilizing the plasmonic effect of AuNPs and the high conductivity of Gr to the existing Pt films-based CE DSSCs. It will provide information on the efficiency enhancement effect of Gr and AuNPs in the assembled DSSCs when used in the composite CE. The outcome of this study will also be useful in synthesis of

crystalline and nanoporous PA, modified using Gr for DSSC applications. The modified cell could provide a reduced charge recombination, improved electron injection and transport through TiO_2, enhancing the overall efficiency of a DSSCs. The results from the study will add valuable information to help in future research and fabrication of DSSCs using nanomaterials.

CHAPTER TWO

LITERATURE REVIEW

2.1 Photovoltaic Technologies

PV technology through the development of solar cells (SCs) has been useful in photoelectric generation since the PV effect was discovered by Becquerel in 1839 (Becquerel, 1839). The PV technologies currently classify SC devices as first, second, third, and fourth-generation, denoted as 1G, 2G, 3G and 4G respectively depending on the materials and technology advances employed (Jayawardena *et al.*, 2013). Figure 2.1 shows the record PV-devices efficiencies over time and the associated material components as reported by the National Renewable Energy Laboratory (NREL) (NREL, 2019). Up to date, these nanomaterials, in addition to others, are still under investigation to actualize 4G.

The 1G of SCs consists of Si-bulk multijunction cells or simply pure crystalline-Si wafers with a thickness of 200–300 μm (Sampaio & González, 2017). Their record power conversion efficiency (PCE) is up to around 25-28% (NREL, 2019). Currently, Si-based SCs dominate the PV technology market (Sampaio & González, 2017), accounting for about 90% of the global market share (Peng & Lee, 2011). This dominance is aided by various factors, most important including; its abundance on earth, wide bandgap (1.12 eV) as a material, and ease of integration from the microelectronic industry (Subtil Lacerda & van den Bergh, 2016; Peng & Lee, 2011). Moreover, its long-term stability (25-30 years) and low maintenance make it more reliable. Although Si is currently abundant, Si-based SCs are relatively expensive due to the high production cost (Green, 2002). Further, they are heavy, bulky and rigid (Patil, 2017) prompting for more research to advance their positive attributes.

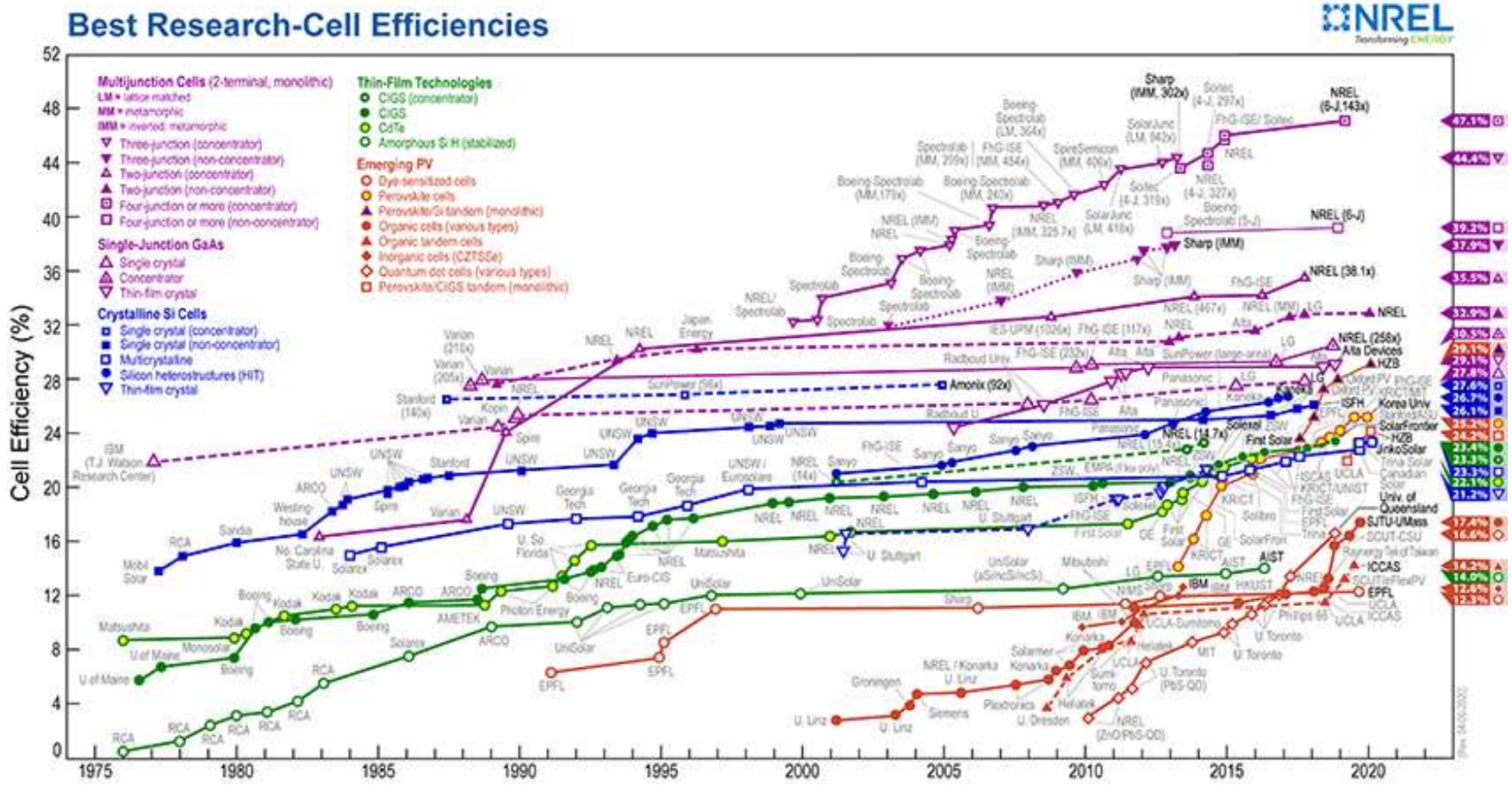

Figure 2.1: Record PV-devices efficiencies over time and the associated material components as reported by the National Renewable Energy Laboratory (Source: NREL, 2019)**.**

The 2G SCs, are based on direct band gap thin film semiconductor materials and technologies identified in 1G, with inclusion of the amorphous or polycrystalline Si, Copper Indium Gallium Selenide (CIGS) and Cadmium Telluride (CdTe) (Green, 2002; Jayawardena *et al.,* 2013). The aim was to reduce the bulk material cost associated with 1G PVs. Through the idea, the quality and quantity of material used reduced significantly. However, increasing absorption of the thin film to compensate for the reduced thickness of the photoactive layers remained a challenge. This resulted in their lower efficiencies, of up to 20% (NREL, 2019; Sampaio & González, 2017).

The efficiency challenges of the 2G necessitated development of the 3G SCs, which includes organic PV (OPV) technologies and DSSCs (Jayawardena *et al.,* 2013). These cells are still in demonstration level with research aiming at generating higher efficiencies at lower cost (NREL, 2019). Through such research, the concept of designing materials at nanoscale and scaling them up to macro-scale is being elevated in 3G. In this regard, focus is on enhancement of energy capture over the solar spectrum and optimization of charge collection to enhance charge and energy transfer processes. The organic (or polymer) materials with desirable PV properties, forms the core for 3G technology. However, DSSCs promise dominance in 3G PVs. Although the 3G SCs have presented significant success, improvements in performance of the resulting devices in terms of cost per watt are necessary. This ensures that the technology competes favorably with the previous PV generations. Currently, intensive investigations and development are on course for the 4G PVs, also referred to as “inorganics-in-organics” (Bai and Shen, 2012). This generation will combine the low cost aspect of the 3G cells and the excellent functionality and stability of novel inorganic and organic based nanomaterials.

With the DSSCs in 3G, vigorous studies are in progress with the aim of developing hybrid (composite) cells through inclusion of Quantum dots (QDs), carbon nanotubes (CNT) and polymers, metal NPs, Gr and various oxides. Such materials are expected to possess improved optoelectronic properties to enhance their PCE within the 4G while maintaining the morphology and architecture of the inexpensive 3G PVs (Luceño-Sánchez *et al.,* 2019). The operation of a DSSC has been found to mimic

photosynthesis in plants (Dodoo-Arhin *et al.,* 2013). As a result, their notable structural and design properties can easily be tailored, making them prospective candidates for combating global environmental and energy challenges (Kanchi *et al.,* 2014; Li *et al.,* 2012).

2.2 History and Growth of Dye-Sensitized Solar Cells

The first DSSC report by O'Regan and Grätzel, (1991) indicated that, sensitization of wide band gap semiconductors in SCs using dyes remarkably increased their energy conversion efficiency. DSSCs are the most predominant and almost mature technology in the 3G PVs (Jayawardena *et al.,* 2013). Moreover, up to now they are the only PV devices capable of separating the two varied cell operations namely, photo-energy harvesting and charge carrier transport, compared to conventional cells, which perform both functions simultaneously, hence requiring high purity materials like silicon, thereby making production costs high. Currently, a lot of research drive is towards the emerging DSSCs technologies. This is motivated by their simplicity in fabrication, low production costs, great aesthetic features and promising high solar energy conversion efficiencies (Snaith, 2010). Once fully commercialized, this technology is expected to present low cost and environmentally friendly SCs to the global market (Brown & Wu, 2009). Recent studies have reported DSSCs achieving an efficiency of 15% although the achievable efficiency for an ideal SC is over 30% upon harvesting photons from ultraviolet (UV) to near-infrared (NIR) regions (Ye *et al.,* 2015). The main limitation in these DSSCs is their long term instability and low electron mobility (Hendry *et al.,* 2006; Yella *et al.,* 2011). Evaluation of the structural materials and design of the DSSCs could provide a route for a viable solution to these limitations (Sharma *et al.,* 2018).

2.3 Structural Design of a Dye-Sensitized Solar Cell

Conventionally, the structure of a DSSC comprises three major components. This consist of a counter electrode (CE), a working electrode (WE), also known as a photoanode (PA), and an electrolyte containing an iodide/triiodide (I^-/I_3^-) redox couple (Dodoo-Arhin *et al.,* 2013; Wu *et al.,* 2014). Figure 2.2 shows the basic

structure of a DSSC (Weerasinghe *et al.,* 2013). The working electrode consists of a TiO_2 film on a transparent conductive oxide (TCO) and sensitized with light-harvesting dye molecules. The two electrodes sandwich the electrolyte and light enters the cell through the PA surface.

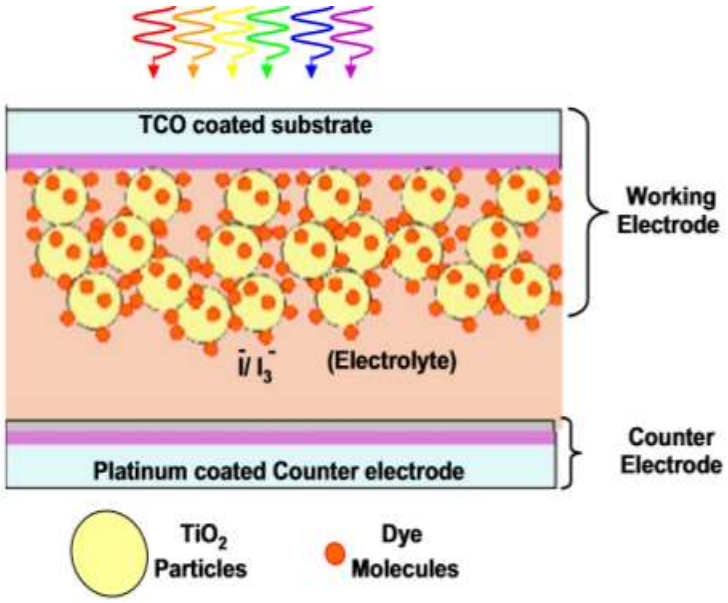

Figure 2.2: The basic structure of a DSSC (Source: Weerasinghe *et al.,* 2013).

2.3.1 The Counter Electrode

A CE comprises a TCO onto which a catalyst is deposited. In DSSCs, CEs play two critical roles which include facilitating charge regeneration and acting as a conduit in the collection and transfer of charge back to the electrolyte redox couple through the external circuit (Dodoo-Arhin *et al.,* 2013; Grätzel, 2001; Lan *et al.,* 2010; Ye *et al.,* 2015). For a CE to effectively execute such functions, it must be an excellent electron conductor and highly catalytic to simultaneously support regeneration of iodide I^- to retard recombination and also collect and transfer electrons (Dodoo-Arhin *et al.,* 2013; Grätzel, 2001; Sedghi & Miankushki, 2014).

Dominantly, Pt film-coated fluorine-doped tin oxide (FTO, F:SnO_2) is preferred for this purpose due to its high transparency, catalysis and high exchange current density (Boschloo & Hagfeldt, 2009; Gong *et al.,* 2011; Meyer *et al.,* 2018). Carbon materials, which have shown excellent PV properties, also find application in

DSSCs, where their composites with platinum are being engineered for possible application in CEs (Choi *et al.*, 2011; Guo *et al.,* 2015; Roy-Mayhew *et al.,* 2010). The stability and charge transfer resistances of the CE and hence its performance depends on the method used to deposit Pt on the FTO coated substrate. The Pt activity as a catalyst in presence of I^-/I_3^- redox couple has been reported to decrease over time due to the changes in catalytic properties (Mehmood *et al.,* 2014).

Some of the common methods used in Pt layer deposition include sputtering (Cheng *et al.,* 2013; Sharma *et al.,* 2018), thermal treatment of chloroplatinic acid in isopropanol (Roy-Mayhew *et al.,* 2010), electrochemical method (Ponken *et al.,* 2017), spin-coating (Lan *et al*., 2010) and doctor blade (Katumo *et al*., 2015). Although sputtering is common, an ultra-high vacuum environment is needed for best results. Additionally, more amounts of platinum is needed to generate one flat surface compared to the very small amount of Pt necessary to produce the catalytic effect required (Lan *et al*., 2010). For the widely used electrochemical, spin coating and doctor blade method, spread out paste results in platinum wastage (Padinger *et al*., 2000). In addition, control of the best parameters such as Pt layer thickness has been difficult leading to low CE transmittance (Ponken *et al.,* 2017). However, the doctor blade method is gaining popularity in research laboratories due to its low cost and simplicity (Katumo *et al*., 2015).

2.3.2 The Photoanode

The PA is a mesoporous film of semiconductor oxide sputtered on a conductive transparent glass material (Figure 2.2) and sensitized by use of a dye. Two main functions of the PA in a DSSC include; support for sensitizer loading and transport of the photo-excited electrons to an external circuit from the sensitizer dye. It is therefore necessary for it to have a large surface area necessary for dye loading, a wide band gap, and outstanding electron affinity (Kim *et al.,* 2014). Titanium dioxide, as a semiconductor oxide thin film, is the most promising and preferred photocatalytic material for a PA in most DSSCs since it meets the threshold. In addition, it is non-toxic and displays biological and chemical stability (Di Paola *et al.,* 2013) hence not prone to corrosion. Usually, TiO_2 occurs in three crystalline

phases: rutile, anatase and brookite, which have direct band structures (Gong *et al.*, 2012). Rutile TiO_2 is the most stable while anatase and brookite are metastable states, but easily convertible to rutile when treatment in heat (Gong *et al.*, 2012). The chemically active anatase form is the most commonly used in DSSCs (Di Paola *et al.*, 2013). Basically, when the surface of a semiconductor material is irradiated by light ($h\nu \geq E_g$), electron/hole pairs (e^- / h^+) are generated by promoting an electron from the valence band (VB) of the dye to its conduction band (CB) (Bessegato *et al.*, 2014). Once electrons from the highest occupied molecular orbital (HOMO) are excited to the lowest unoccupied molecular orbital (LUMO) of the dye, TiO_2 film accelerates the photo-excitons to the cell external circuit (Ye *et al.*, 2015).

Titanium dioxide has a wide band gap (~3.2 eV) which activates under UV light irradiation (Sclafani and Herrmann, 1996). Out of the total solar spectrum, the UV region covers only 5% while the broad visible region is approximately 40% (Figure 1.2). For sustainable photocatalytic processes, it is necessary to develop materials with excellent photo-response when irradiated with visible light to fully utilize the sunlight spectrum (Wei *et al.*, 2016). To achieve complete TiO_2 photoactivation under visible light irradiation, nanometer scale modifications have been studied for PV applications. These include introduction of a layer of NPs on the TiO_2 (Mayumi *et al.*, 2017), use of double layers of TiO_2 NPs (Tyas *et al.*, 2017), textural and structural modification by varying of the size of TiO_2 NPs (Ismagilov *et al.*, 2012) and many others. These aims at providing high surface area for increased dye loading, enhanced photon absorption, and creating a mesoporous structure (Zhang *et al*., 2007; Haynes *et al*., 2011) and serving as a ultraviolet (UV) light protector layer for unstable organic dyes (Hagfeldt *et al*., 2010), all with a view of improving cell efficiency.

Some of the techniques used in preparation of PAs include; chemical vapour deposition (CVD) (Asim *et al.*, 2014), physical vapour deposition (PVD) (Laurenti & Cauda, 2018), electrodeposition, spray pyrolysis (Heidari *et al.*, 2018), spin-coating (Sadikin *et al.*, 2017), screen printing (Ito, 2011), sol-gel and doctor-blade (Adawiyah & Endarko, 2017; Huynh *et al.*, 2009). However, the method of choice depends on the materials used, cost of preparation, and availability of preparation

equipment. Based on the coating method, the semiconductor oxide layers in DSSCs occur as continuous networks of ordered and disordered structures with pores of diameters in the range 2 - 50 nm, characteristic of mesoporous materials (Niu *et al.*, 2018). This enhances the specific surface area of the semiconductor hence increasing internal diffusion and reaction sites for dye adsorption (Sedghi & Miankushki, 2015).

Doctor blade method, which has been extensively employed on a laboratory scale fabrication of DSSCs was used in this work (Huynh *et al*., 2009). It is an economical method and minimizes the loss of particles during spreading (Ahmadi *et al*., 2014). Figure 2.3 depicts the main steps taken in doctor blading. This technique involves deposition of a film on a substrate by spreading a paste using a blade held at an angle. The steps involves; taping the conductive side of the substrate, deposition of the paste on a glass substrate, spreading of the paste and film drying (Ahmadi *et al*., 2014). The tape, preferably scotch magic tape, is used as a guide when spreading the paste, and also to control thickness of the resulting film (Mohamad, *et al*., 2017).

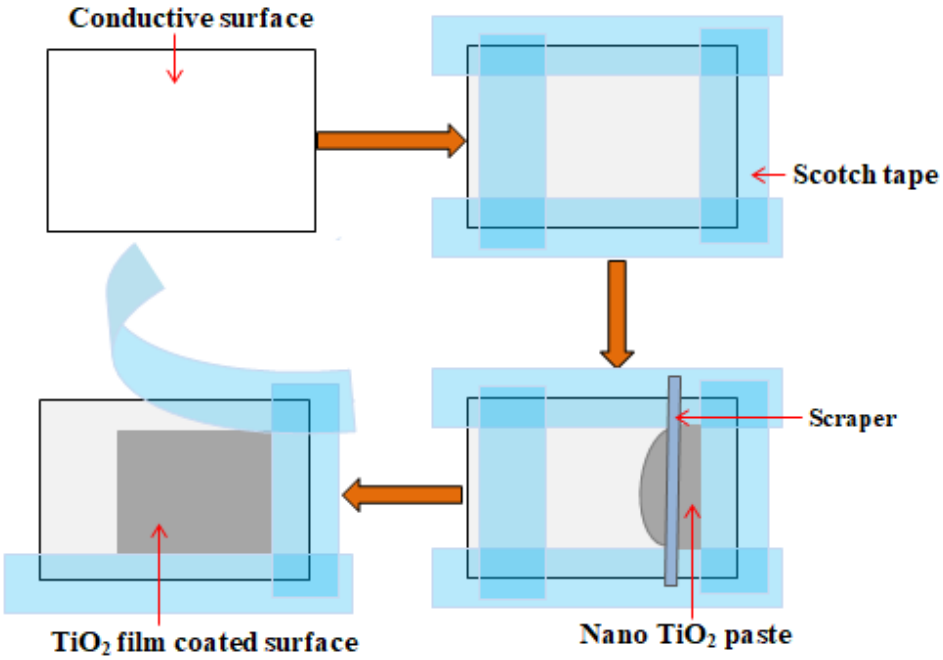

Figure 2.3: A cartoon illustration of the doctor blade method for TiO2 film

To ensure desirable crystal structure and sufficient porosity of the mesoporous film for the best contact at the TiO_2/dye/electrolyte interface, the drying of the TiO_2 coated module should be made slow before sintering is done (Gong *et al.,* 2012).

2.3.3 The Dye Sensitizer

Dye sensitizers form part of the most important materials in DSSCs that determine the performance of the SCs. They harvest photo-energy so as to excite electrons within the semiconductor interface (Ye *et al.,* 2015). For the sensitizer to load on the semiconductor material, it should possess the right chemical functional groups for good adsorption on to the semiconductor material. Moreover, for effective electrons injection into the TiO_2 and subsequent dye regeneration, desirable LUMO and HOMO levels are essential (Ye *et al.,* 2015). In addition to the excellent photo-stability and solubility for best energy harvesting, dyes should also possess high molar extinction coefficients over the Vis and NIR regions (Nivea *et al.,* 2014). Various sensitizers that have been synthesized and their performance evaluated in DSSCs include, the perovskite-based sensitizer, ruthenium-complex dyes, mordant dyes, quantum dot sensitizer, metal-free organic dyes and natural dyes (Shalini *et al.,* 2016; Ye *et al.,* 2015). Among these, Ru- and perovskite-based sensitizers have recorded remarkable performance (Shalini *et al.,* 2016; Ye *et al.,* 2015).

Although metal-free dyes could be possible candidates to replace Ru-dyes, lack of full understanding of their aggregation mechanism derails them from matching the Ru complexes in performance (Ye *et al.,* 2015). Consequently, Ru-based dyes are the most popular choice for research on DSSCs, where N719 (Ruthenizer 535-bisTBA) and N3 (Ruthenizer 535) have been widely investigated with excellent performance in DSSCs being reported (Bandara *et al.,* 2016). According to Ye *et al.,* (2015), a PCE value of 11.7% has been recorded from DSSCs based on Ru-complexes. Figure 2.4 shows the molecular structure of the two most common Ru-complexes, the N3 and N719 dyes depicting the same structure except that N719 has TBA^+ (tetrabutyl ammonium) substituting H^+ at two carboxyl groups (Mao *et al.,* 2012). So far, N719 is the most successful dye in DSSCs (Fattori, 2010; Shalini *et al.,* 2016).

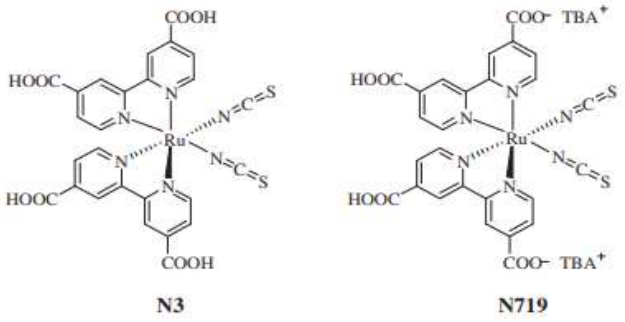

Figure 2.4: Molecular structure of the two common Ru-complexes N3 dye and N719 dye (Source: Mao *et al.*, 2012).

The remarkable performance exhibited by these two dyes is due to their high stability arising from the octahedral geometry in their molecular structure (Mao *et al.*, 2012). Such structure enables them to tolerate the attachment of various specific ligands in a controlled manner (Qin & Peng, 2012). Moreover, their wide energy levels covering wide light absorption spectrum, extending from the UV to NIR with respect to the TiO_2 PAs and the I^-/I_3^- redox complex makes them more successful (Hardin *et al.*, 2012).

2.3.4 The Liquid Electrolyte

The main role of an electrolyte in a DSSC is to allow electrons transport to the oxidized dye from the CE. For high-efficiency DSSCs, electrolytes need to possess high solubility and ionic mobility enough within organic medium, fast electron transfer kinetics with minimal over-potential at the CE, good interfacial contact and enough driving force for the dye regeneration process (Grätzel & Zakeeruddin, 2013; Mehmood *et al.*, 2014). The different categories of electrolytes in use include; liquid electrolytes, quasi-solid electrolytes, and solid-state electrolytes (Ye *et al.*, 2015). Liquid electrolytes are the most common in DSSCs. Electrolytes possess two charge carriers (positively and negatively charged ions), that occur in equal concentrations as opposed to semiconductors, where two charge carriers (electrons and holes) exist with one dominating upon doping. The most universally endorsed and dominant liquid electrolyte consists of a solvent into which I^-/I_3^- redox couple is dissolved. This is highly preferred due to its ability to effect faster oxidation (Ox) of the I^- and

reduction (Red) of I_3^- at the PA/electrolyte and electrolyte/CE interfaces, respectively, during electron transfer process (Ye *et al.*, 2015).

2.4 Structural Operation of a Dye-Sensitized Solar Cell

To develop materials with excellent structure and optimize them for best DSSCs operation, it is necessary to understand the chemical complexities of a DSSC at different levels of operation (O'Regan & Durrant, 2009). Figure 2.5 shows a schematic diagram of the structure and operational principle of a DSSC indicating the processes [1]–[8] involved during photo-energy conversion in a DSSC. The operational energetics and kinetics of a typical DSSC shown involves a competition between photocurrent generating forward processes [1]-[5] and electron recombination back processes [6]–[8] (Sharma *et al.*, 2018).

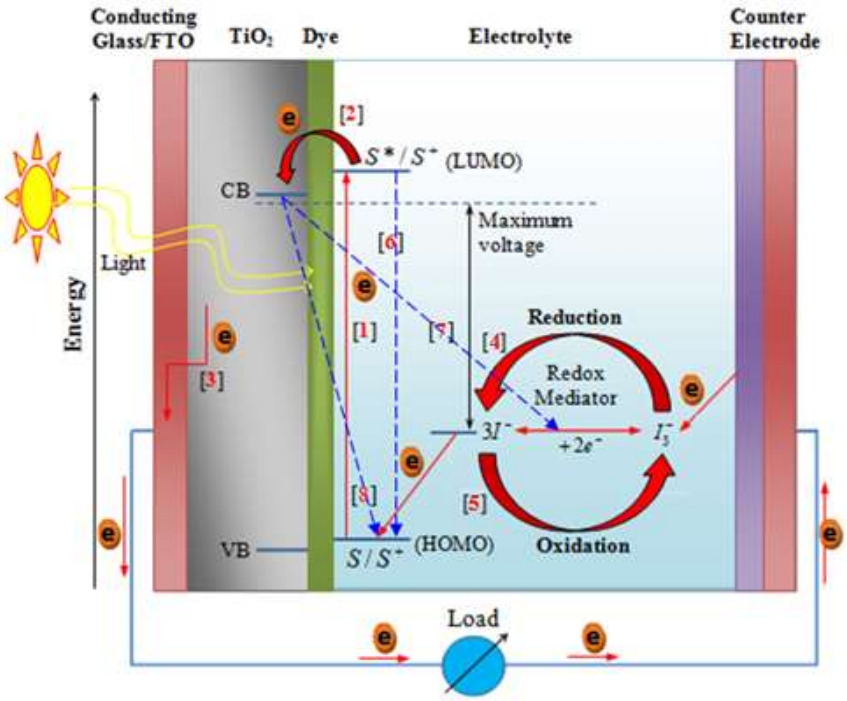

Figure 2.5: A schematic diagram of the structure and operational principle of a DSSC indicating the processes [1] – [8] involved during photo-energy conversion in a DSSC (Source: Sharma *et al*., 2018).

According to Grätzel, (2005), photocurrent generation a DSSC, is usually a competition between electron transfer kinetics by the desired forward processes and the inhibitory backward processes. As the forward processes promote photocurrent generation, the backward processes lead to e^{-}/h^{+} recombination, which limits charge injection, transfer and regeneration within the dye and electrolyte. However, for I^{-}/I_3^{-} system, electrons recombination (lifetimes) are usually long compared to other redox systems used, measured under one sun light intensity. This explains the success of this particular redox couple (Yang, 2017) and hence the continuous photocurrent generation as long as solar energy is present. The following section describes the cell processes, giving their corresponding equations.

2.4.1 Photocurrent Generating Processes [1] – [5]

Process [1]: Photo-energy absorption and dye excitation

This is the first step in photocurrent generation in a DSSC. In DSSCs, dyes meant to adsorb onto the surface of the nanocrystalline TiO_2 semiconductor film that coats the PA. When the Ru-complex photosynthesizer (*S*) absorb a photon of sufficient energy ($h\nu$), the electrons in the dye get excited from ground state (S/S^{+}) to a higher energy state (S^*/S^{+}). This process is described by equation (2.1);

$$S\left(on\ TiO_2\right)+h\upsilon \rightarrow S^{*}\left(on\ TiO_2\right) \quad \text{2.1}$$

Process [2]: Electron injection into the CB of the TiO_2

In this second step, the photoexcited dye (*S**) injects an electron into the CB of the TiO_2 which lies below the excited state of this dye. This injection process results in oxidation of the photosynthesizer (S^{+}) (Katoh, 2012), and is described by equation (2.2);

$$S^{*}\left(on\ TiO_2\right) \rightarrow S^{+}\left(on\ TiO_2\right)+e^{-}\left(on\ TiO_2\right) \quad \text{2.2}$$

An efficient dye needs to have a LUMO level higher than the CB of the TiO_2 to permit electron injection into the CB of TiO_2 and subsequent transfer into the

external circuit through the TiO_2 (Thavasi *et al.,* 2009). Otherwise, those electrons would recombine with the holes back in the HOMO of the dye (Hagfeldt *et al.,* 2010). Since Ru-complexes have ultrafast injection processes, the device's performance time scales compare well to the decay behavior of the excited dye state, back to the ground state (Shalini *et al.,* 2016; Thavasi *et al.,* 2009). This time ranges from 20 to 60 ns, and is the excited state lifetime of the Ru-complexes dye. For DSSCs, an enlarged TiO_2 surface area increases the number of contact points between TiO_2 and the dye, resulting in an improved cell performance (Velázquez-Martínez *et al.,* 2019). The success of TiO_2 in its operation greatly influences its solid-state properties such as porosity, surface area, crystallinity, electrical conductivity and surface morphology (Umale *et al.,* 2017). These properties depend on the success of preparation and treatment during synthesis.

Process [3]: Electron transport through TiO_2

The third step involves electron transport through the mesoporous TiO_2 film. Mesoporous DSSCs have been considered highly efficient in charge transport (Lee *et al.,* 2017). Once an electrons (e^-) is injected into the CB of the TiO_2, it diffuses through the bulk of the nanocrystalline TiO_2 to the back contact phase, commonly FTO. This process is shown by [3] in Figure 2.5 and described by equation (2.3);

$$e^-(on\ TiO_2) \rightarrow e^-(on\ FTO) \quad \text{.....2.3}$$

The external circuit then provides a path through which the electrons reach the CE via diffusion process, thereby powering an electrical load if connected.

Process [4]; Reduction of the redox couple

This process is represented by [4] in Figure 2.5 and takes place within the electrolyte. It involves iodide regeneration through reduction of the electron acceptors. In the presence of a thin catalytic layer of platinum deposited onto the supporting material over the substrate forming the CE, the oxidized redox mediator (I_3^-) diffuses toward this CE where it is reduced to I^- ions (Katoh *et al.,* 2007). For a DSSC, charge transfer process between the PA and CE are dictated by the

diffusion of I_3^- ions. This process is in the range of 10^3 s^{-1} (Rahman *et al.,* 2015) and described by two-level equations (2.4) and (2.5) below:

$$\frac{1}{2}I_3^- + e^-(Pt) \rightarrow \frac{3}{2}I^- \quad \text{.....2.4}$$

$$I_3^- + 2e^-(Pt) \rightarrow 3I^- \quad \text{.....2.5}$$

Process [5]: Dye regeneration

The fifth step involves dye regeneration, and represented by process [5] in Figure 2.5. At this point, the oxidized photosensitizer (S^+) is again regenerated through electron donation from the iodide in the electrolyte. The acceptance of an electron from the I^- ion redox mediator, results in regeneration of the ground state (*S*) of the dye. Consequently, the I^- ion get oxidized to I_3^-. This process is an electron transfer mechanism described by equation (2.6) below (Katoh *et al.,* 2007);

$$S^+(on\ TiO_2) + \frac{3}{2}I^- \rightarrow S(on\ TiO_2) + \frac{1}{2}I_3^- \quad \text{.....2.6}$$

A fast dye regeneration to the ground state occurs when an electron is accepted from I^- and oxidized to I_3^- (Sharma *et al.,* 2018). Thus, this process occurs within a time range of microsecond, faster than any recombination reaction or oxidized dye intrinsic lifetime in DSSCs (Katoh *et al.,* 2007).

2.4.2 Recombination Processes [6]–[8]

Process [6]; Decay of the excited dye to ground state,

The process is described by equation 2.7.

$$S^* \rightarrow S \quad \text{.....2.7}$$

Due to the fast (picoseconds) speed of electron injection into the TiO_2, recombination to the ground state is limited.

Process [7]: Recombination between the oxidized dye and the injected electrons

The speed of this process is in the order of 10^6 s^{-1} and results in a reduction in electron density within the semiconductor film of TiO_2 (Rahman *et al.*, 2015). This process changes the energy of the TiO_2 CB, a change that affects the resulting cell V_{oc} (Maluta, 2010). The process is described by equation 2.8 below;

$$S*(on\ TiO_2)+e^- \rightarrow S \quad \text{.....2.8}$$

Process [8]: Capture of the injected electrons by the triiodide

This is a back reaction process, and takes place within the electrolyte. It involves a capture of the injected electrons by the triiodide. The process is similar to the I^-/I_3^- couple reduction process at the CE and described by equation 2.9 below.

$$2e^-(Pt)+I_3^- \rightarrow 3I^- \quad \text{.....2.9}$$

During electron diffusion through the TiO_2 structure, some of the electrons get trapped on the surface of its particles of the TiO_2 hence recombine with I_3^- within the electrolyte. Since full coverage of the glass/FTO surface by the TiO_2 film may not occur during coating, the electrolyte reaching the FTO results in a leakage of electrons. The speed of this recombination process is 10^1 to 10^0 s^{-1} (Rahman *et al.*, 2015).

2.5 Photovoltaic Parameters: Short-Circuit Current Density, Open-Circuit Voltage, Maximum Power Density Output and Fill Factor

The standard technique of measuring a SC performance is to evaluate its photocurrent density-voltage ($J-V$) curve (Roy-Mayhew and Aksay, 2014). The current density (J), is often used since it normalizes PV parameters with respect to electrode area (active area), as opposed to actual current. A $J-V$ curve is generated by running a current through the cell at a variable external resistance. When a light spectrum of a well-defined intensity such as an AM1.5G solar simulator is applied to a SC, its $J-V$ response can be measured and PV parameters deduced (Roy-Mayhew

and Aksay, 2014). The various parameters used to characterize the performance of a PV module include; the short-circuit current density (J_{sc}), open-circuit voltage (V_{oc}), maximum power density output (P_{max}), fill factor (FF), and Photocurrent conversion efficiency (PCE) or simply, the cell efficiency (η) (Sharma *et al.,* 2018). Figure 2.6 shows a diagrammatic illustration of a typical *J-V* characteristic and power density curve, with the main parameters (V_{oc} and J_{sc}) necessary for evaluating solar cell efficiency indicated. The values of current density and voltage of the cell at P_{max} are represented by J_{pm} and V_{pm} respectively, as indicated and discussed thereafter.

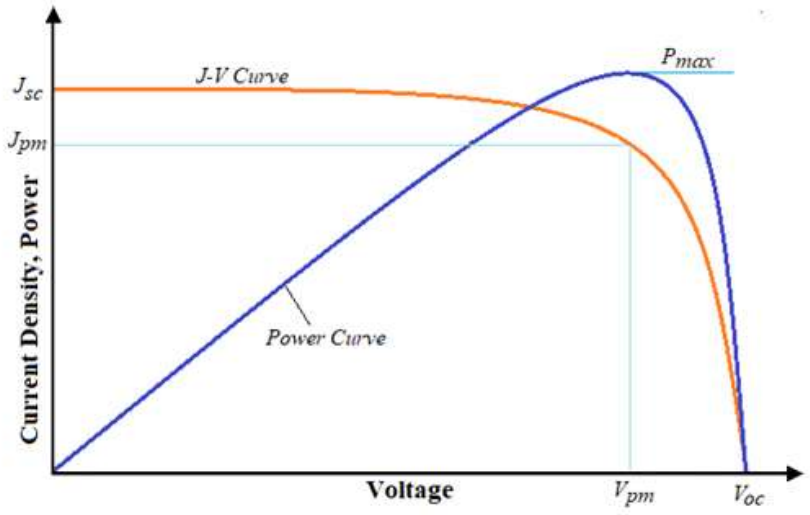

Figure 2.6: A diagrammatic illustration of a typical J-V curve, showing the current density and voltage of the cell at maximum power (p_{max}) represented by J_{pm} and V_{pm} respectively (Source: Sharma *et al.,* 2018).

When an electrical load is connected to a SC, a potential difference develops across its terminals. An SC then behaves in a similar manner to a diode, whereby, by applying a bias in dark, a current (referred to as dark current) flows. The corresponding dark current density (J_{dark}) is usually expressed by equation (2.10) (Wenham *et al.*, 2013);

$$J_{dark} = J_0\left[\exp\left(\frac{qV}{nk_BT_a}\right)-1\right] \quad \text{.....2.10}$$

where J_0 is the reverse saturation current density, V is the applied voltage, q is electron charge, k_B is the Boltzmann constant, T_a is the absolute temperature and n is the ideality factor (a number between 1 and 2).

The short-circuit current density, denoted as J_{sc}, is described as the current that passes through a SC of one square centimeter in area, at low impedance and zero cell external load (Shaikh *et al.,* 2019). Practically, J_{sc} is simply the current reading when the voltage reading is zero in a biased SC and results from the generated and collected photo-generated charge carriers (Sugano *et al.,* 2017). Basically, J_{sc} depends on the solar illumination, active area of the SC, the charge transfer probability of the cell module and the optical properties of the electrodes structure.

The net current density (J) is the difference between the J_{sc} and J_{dark} is given by equation (2.11) (Wenham *et al.,* 2013);

$$J = J_{sc} - J_{dark} = J_{sc} - J_0\left[\exp\left(\frac{qV}{mk_BT_a}\right) - 1\right] \quad \text{.....2.11}$$

It can be noted that, J_{sc} is directly proportional to the available sunlight hence equivalent to the photo-generated current density. This means that it depends on the level of dye adsorption onto the TiO_2 and on the chemical and electrical kinetic of the electrolyte redox couple (Wenham *et al.,* 2013).

When the contacts of a SC are isolated, the maximum voltage generated is the open-circuit voltage (V_{oc}). This means that measurement of V_{oc} is done when a load of infinite resistance is connected to the terminals of the cell. Under cell illumination, V_{oc} corresponds to the level of forward bias on SC resulting from SC junction bias with photo-generated current (Nelson, 2003). This correspondence is dictated by the energy difference between the Fermi levels (E_F) of the FTO/TiO_2 contact under illumination and the electrolyte redox potential (ΔV_{redox}) as shown by equation (2.12) (Shaikh *et al.,* 2019; McConnell, 2002);

$$V_{oc} = E_F - \Delta V_{redox} \quad \text{.....2.12}$$

where E_F is usually near the CB in n-type semiconductor materials.

Considering an open-circuit condition of the cell, then $J_{dark} = J_{sc}$ hence V_{oc} is given by equation (2.13) (Nelson, 2003);

$$V_{oc} = \frac{k_B T_a}{q} \ln\left(\frac{J_{sc}}{J_0} + 1\right) \quad \text{.....2.13}$$

This equation (2.13) shows that there exists a logarithmic increase in V_{oc} with light intensity.

The power density (P) established by a SC and delivered to the connected load in Watt/cm^2 at any given bias voltage is calculated along the J-V characteristic from the product of measured cell voltage (V) and current density (J), equation (2.14) (Sharma *et al.*, 2018).

$$P = J \times V \quad \text{.....2.14}$$

At the operating points (V_{oc} and J_{sc}), power density is always zero and P_{max} occurs between the two points for any SC. The current density and voltage at P_{max}, are denoted by J_{pm} and V_{pm} respectively, as shown in Figure 2.6. The two values are too important in evaluating cell efficiency.

The fill factor (FF) of a SC is the ratio of its maximum possible power output to the product of J_{sc} and V_{oc}. Graphically, FF is represented by the largest rectangle area that can fit in the plotted J-V curve (Sharma *et al.*, 2018) and given by equation (2.15);

$$FF = \frac{\text{maximum power density } (P_{\max})}{J_{sc} V_{oc}} = \frac{J_{pm} V_{pm}}{J_{sc} V_{oc}} \quad \text{.....2.15}$$

Typically, FF values range from 0.50 to 0.82 (Ginley and Cahen, 2011) and can also be expressed in percentage where the higher values are more preferred for best DSSC performance.

2.6 PCE Measurement and Enhancement in DSSCs

Although several measures characterize DSSCs, the universally adopted one is the total amount of electrical power generated by the cell for a given amount of solar power shining on it. The PCE or η is defined for a cell as the ratio of its energy output to its input solar energy (Sharma *et al.,* 2018). It is an essential parameter for confirming the performance of SC under testing and depends on the incident solar intensity (P_{in}) and the operating temperature of the SC. The overall PCE (%) under a light intensity of 100 mW cm^2 (AM1.5) is estimated based on J_{sc}, V_{oc}, FF, and P_{in} as given by equation (2.16);

$$\eta = \frac{P_{\max}}{P_{in}} \times 100\% = \frac{FF \times J_{sc} \times V_{oc}}{P_{in}} \times 100\% \quad \text{.....2.16}$$

The PCE value for any cell provides an insight into the overall functionality of its four main components (Ye *et al.,* 2015). With DSSCs promising reliability as a future energy source, various modifications have been carried out based on their functional principles, materials, and structural designs (Cheng *et al.,* 2013; Katumo *et al.,* 2015) to improve their photo-energy conversion efficiencies. Such includes electrodes material restructuring (Bhagwat *et al.,* 2017), change of electrolytes (Yella *et al.,* 2011) and use of varied dyes (Bandara *et al.,* 2016). In the last decade, much focus has been on the effect of the CE materials and designs on the performance of DSSCs upon electrochemical analysis (Cheng *et al.,* 2013; Meyer *et al.,* 2018), with significant improvements being recorded. However, there is more room for improvement according to the ongoing studies (Ghifari *et al.,* 2020). The focus of this work is on incorporating graphene, a carbonaceous material, and plasmonic AuNPs in DSSC CE structure to increase electron injection and regeneration with a view to improving their photocurrent generation.

2.7 Graphene in Photovoltaics

2.7.1 Graphene as an Allotrope of Carbon and as a Novel Material

Carbon, which is abundant on earth, is regarded as the basic building block of organic materials (Zhu *et al.*, 2009). It consists of various allotropes namely; diamond, graphite, fullerenes (C_{60}), CNT, and graphene (Castro Neto *et al.*, 2006). Graphene is regarded as the mother of these other forms of carbon through a stack of graphene layers (GL), rolled-up to a cylindrical form of graphene or balling into a sphere to form the different dimensions (Castro Neto *et al.,* 2006). Figure 2.7 illustrates the common naturally occurring carbon allotropes (Scarselli *et al.,* 2012).

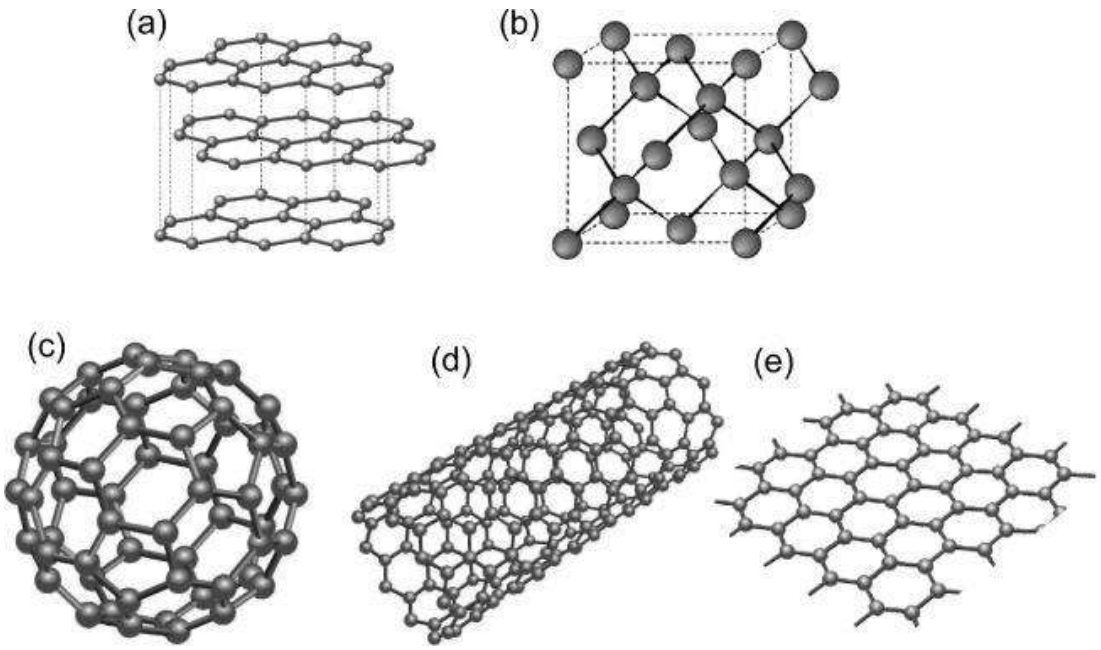

Figure 2.7: An illustration of some common naturally occurring carbon allotropes (a) Graphite: Layered graphene stacks, (b) Diamond: Cubic; with 4-coordinated sp^3 framework, (c) Fullerene: A 0-D structure, (d) Nanotube: A 1-D structure and (e) Graphene: A 2-D structure (Source: Scarselli et al., 2012)**.**

Graphite (Figure 2.7 a), is layered graphene stacks that forms a 3-D structure. Diamond (Figure 2.7 b), is a cubic structure displaying a 4-coordinated sp^3 framework. Fullerene (C60) (Figure 2.7 c), is a wrapped-up graphene or closed cage sp^2 molecule by introducing pentagons on the lattice to form a 0-D structure. Carbon

nanotube (Figure 2.7 d), is a cylindrical sheet or layers of sp^2 molecules forming a 1-D structure. Graphene (Figure 2.7 e) is a single atom thick graphitic layer showing sp^2 bonding with a honeycomb lattice structure and was the first truly two-dimensional (2-D) material to be discovered (Novoselov *et al.*, 2005).

Figure 2.8 shows a pictorial representation of (a) graphene geometry with armchair and zig-zag edges, (b) bonding configuration and (c) corresponding band diagram showing zero band gap (Lemme, 2009).

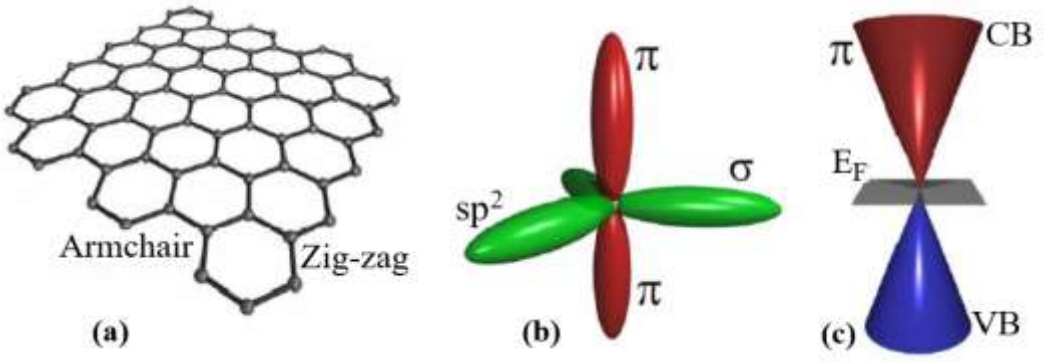

Figure 2.8: A pictorial representation of (a) graphene geometry, (b) bonding configuration and (c) corresponding band diagram showing zero band gap (Source: Lemme, 2009).

Through the sp^2- hybridization, each carbon atom bonds four of its neighboring valence electrons. One of the valence electrons occupies an orbital position perpendicular to the one-dimensional (1-D) sheet forming a delocalized π-bond system while the other three participates in σ-bonding with their close neighbors to generate the honeycomb structural lattice (Figure 2.8 b). The π-bond, which is a delocalized contrast to the localized σ-bonds, highly influences the electronic properties of the material (Fujii *et al.*, 2014) by allowing for the creation of a 2-D electron gas which has a high mobility within the sheets (Lemme, 2009). Since each of the carbon atoms constitutes a hexagonal form of one π-electron, a linear energy band structure in the low energy scale (below several *eV*) generated based on the tight-binding approximation.

2.7.2 Layered Graphene

Graphene, since its first isolation by exfoliation of graphite and subsequent definitive identification by Novoselov and Geim (Novoselov *et al.,* (2004) as a true 2-D material, further studies have revealed many of its intriguing properties above other carbon structures and materials. Table 1.1 shows some of its unique physical properties, which align it with PV applications. Some of the properties include; high charge carrier mobility, high thermal conductivity, high transparency, large specific surface area, outstanding mechanical properties, and zero band gap (Lee *et al.,* 2013).

Table 2.1: Some unique physical properties of graphene (Source: Lee *et al.,* 2013).

Charge carrier mobility	~2000 $cm^2/V.s$
Thermal conductivity	~5000 W/m.K
Transparency	~97.4%
Specific surface area	~2630 m^2/g
Young's modulus	~1TPa
Tensile strength	~1100 GPa
Bandgap	Zero

With such properties, graphene is viewed as a promising candidate for the post-silicon age especially in the field of optoelectronics (Novoselov *et al.,* 2004) in its pure or doped form with tests on possible applications being on the rise (Sood *et al.,* 2015). The fascinating optoelectronic properties of graphene could be attributed to its zero-energy band gap electronic structure (Castro Neto *et al.,* 2009). This causes electrons within it to hop at very high velocity ($\sim 1\times10^6\ m/s$) and with minimal scattering (Novoselov *et al.,* 2004). Electronically, graphene exhibits linear dispersion in terms of energy and momentum near the Fermi energy and hence can be modeled in terms of relativistic massless Dirac Fermions (Wallace, 1947). The light-matter interaction in it exhibit a simple optical absorption within the Vis-IR

spectrum with absorbance independent of frequency (Koshino and Ando, 2008) and given by equation (2.17);

$$\pi\alpha = 2.3\% \quad \text{……...……..……..……..……...…2.17}$$

with the fine structure constant α being given by equation (2.18);

$$\alpha = e^2/\hbar c \approx 1/137 \quad \text{……..……..……...……2.18}$$

where, $\hbar$ is the reduced Planck's constant while c is the finite speed of light (Kuzmenko *et al.,* 2008). The universal absorbance of graphene is equivalent to frequency-independent optical sheet conductivity as given by equation (2.19);

$$\sigma_o = \pi e^2/2h \quad \text{……..……...……...……2.19}$$

This optical sheet conductivity arises from chiral resonance of particle-antiparticle pairs upon absorption of a light photon (Mishchenko and Halperin, 2003). It is defined by the sum of the contributions of the intra-band $\pi - \pi^*$ and inter-band $(\sigma - \sigma^*)$ transitions equation (2.20) (Mak *et al.*, 2012);

$$\sigma = \sigma_{\pi-\pi^*} + \sigma_{\sigma-\sigma^*} \quad \text{……..……..……...……...……2.20}$$

The $\sigma - \sigma^*$ transitions are high-energy transitions involving short wavelengths (<150 nm) and do not occur within the UV-Vis region, while $\pi - \pi^*$ are low energy transitions occurring in the UV-Vis regime hence can be observed. For the $\pi - \pi^*$ transitions, optical conductance is a complex number equation (2.21);

$$\sigma_{\pi-\pi^*} = \sigma_r + i\sigma_i \quad \text{……..……..……...……2.21}$$

where σ_r and σ_i represent the real and imaginary optical conductance of graphene modeled using theoretical conductivity curves under non-interacting linear response theory prediction (Chang *et al.*, 2014; Stauber *et al.*, 2008).

For incident photon of $\lambda = 550\ nm$ at room temperature (T = 300K), $\sigma_{\pi-\pi^*} \approx \sigma_o$ while the energy gap between $\sigma - \sigma^*$ bands is $\approx 6\ eV$ (Saito *et al.*, 1998). Since this energy gap is larger than the energies of the photons in the Vis range, the $\sigma - \sigma^*$ transitions majorly result in a phase shift of optical waves that pass through the graphene sample. It thus contribute only to dispersion with the phase shift being negligibly treated (Saito *et al.*, 1998; Saleh and Teich, 2007). The transmittance $T(\omega)$ and the optical conductivity $\sigma(\omega)$ for single-layer graphene (SLG) are related as per equation (2.22) (Min and MacDonald, 2009; Nair *et al.*, 2008);

$$T(\omega) = \left(1 - \frac{4\pi}{c}\sigma_1(\omega)\right) \text{……..……..……..2.22}$$

This expression translates to equation (2.23);

$$\sigma_1(\omega) = \left(1 - T(\omega)\right)\frac{c}{4\pi} \text{ ……..2.23}$$

where, $1 - T(\omega) = A$ is the absorbance (Stauber *et al.*, 2008).

Therefore, optical conductivity $\sigma_1(\omega)$ of SLG sheet (Mak *et al.*, 2012) expressed in terms of absorbance gives, equation (2.24);

$$\sigma_1(\omega) = A\left(\frac{c}{4\pi}\right) \text{……..……..……2.24}$$

but $A \approx \pi\alpha$ (Stauber *et al.*, 2008).

Therefore,

$$\sigma_1(\omega) \approx \pi\alpha\left(\frac{c}{4\pi}\right) = \pi\left(\frac{e^2}{\hbar c}\right)\left(\frac{c}{4\pi}\right) \text{……..……..……2.25}$$

$$\sigma_1(\omega) \approx \frac{\pi e^2}{2(2\pi\hbar)} \text{ ……..……..……..……2.26}$$

Since $2\pi\hbar = h$, then,

$$\sigma_1(\omega) \approx \frac{\pi e^2}{2h} = \sigma_0 \quad \text{.....2.27}$$

2.7.3 Graphene – Light Interaction in Dye-Sensitized Solar Cells

Structurally, the graphene lattice possesses free π-electron orbitals, which provide additional energy transfer mechanisms including multiplication of charge carriers (Semonin *et al.,* 2011; Winzer *et al.,* 2010). When light energy impinges on a graphene-based cell, an electron-hole pair (e^-/h^+) is first created by the association of photon energy with the semiconducting Gr band gap (Gabor, 2013). The excess photon energy, instead of dissipation as heat, may cause collisions and scattering of the e^-/h^+ into the graphene lattice releasing a secondary pair ($E_g = 0$) (Gabor, 2013). These two e^-/h^+ can now create two more electrons resulting in four more, a process that repeats resulting in carrier avalanche multiplication effect (Winzer *et al.,* 2010). This effect makes it possible to construct PV cells with much higher energy conversion efficiency, a novelty if realized, could allow photo-energy harvesting by Gr based PV devices over the entire spectrum at minimal loss. Its high optical transparency and excellent electrical conductivity make it a material of choice especially for thin-film TCOs (Cai *et al.,* 2009). This permits maximum light to reach the active material with minimal resistance of the charge collector to take off the current generated. The amount of current generated in this case depends on the tuning level of the semiconductor.

The current practical DSSCs have shown low efficiencies (Grätzel, 2005) compared to the theoretical efficiency (Shockley and Queisser, 1961). The low PCE results from poor diffusion of the redox species and the limited charge separation, which leads to poor energy harvesting in the resultant cells (Jennings *et al.,* 2011; Wu *et al.,* 2017). Owing to the forgoing excellent properties of graphene (Table 2.1), a hybrid CE of Pt and Gr has been shown to enhance the PCE in DSSCs (Gong *et al.,* 2011; Yue *et al.,* 2013).

2.7.4 Graphene Synthesis Techniques

The three main methods currently employed in graphene synthesis include; mechanical exfoliation, chemical vapor deposition (CVD) of hydrocarbons on transition-metal-carbide surfaces, and epitaxial growth of graphene on SiC substrates. Basically, graphene sheets are stacked one over another by weak Van der Waals forces, which offer interaction energy of approximately 2 eV/nm in between any two layers. These interlayer forces must be broken in order to produce a high purity monolayer graphene (Huc *et al.,* 2008).

Mechanical exfoliation of graphene involves manual cleaving (microcleaving) of graphite to break these weak bonds and separate the individual graphene sheets or few-layer graphene as pioneered by Novoselov and Geim (Novoselov *et al.,* 2004). Using a scotch tape, graphene flakes are peeled-off the bulk graphite, in this case highly ordered pyrolytic graphite (HOPG). Repeated sticking and pulling of the tape strips further thins the flakes. Finally, the flakes are detached, cleaned and transferred onto an appropriate substrate surface. Since the optical properties of graphene nanosheets are greatly dependent on the stack thickness, a significant difference between the properties of single-layer graphene (SLG), bilayer graphene (BLG), few-layer graphene (FLG), multilayer graphene (MLG) and bulk graphite is evident (Ni *et al.,* 2007; Shmavonyan *et al.,* 2013). Different methods can be used to establish the number of stacked layers in FLG and MLG samples (Blake *et al.,* 2007; Ferrari *et al.,* 2006). However, identification and determination of atomic layers in FLG is a challenging task with most researchers being limited in such methods. Since exfoliation is not a well-controlled process, its success requires some experience and training to distinguish SLG, FLG and MLG). Due to the difficulty in controlling the flake thickness, size and location, cleaving samples with a large area for practical applications has not been effective. However, researchers are working towards actualizing it (Shmavonyan *et al.,* 2013).

Chemical vapor deposition method has also been widely employed to grow graphene onto a substrate. The CVD is a chemical process involving reactions between the gaseous phase reactants near the surface of a heated substrate to make thin films

(Choy, 2003; Reina *et al.,* 2009). The deposition process is flexible in nature, making CVD a method of choice in thin film deposition and coatings in optoelectronic devices (Choy, 2003). It is one of the most promising and relatively inexpensive synthesis methods for large-area, high-quality graphene. Some of the commonly exploited chemical reactions include oxidation, reduction, and pyrolysis (Chen *et al.,* 2010). The growth mechanism of these films is based on the 2-D nature of graphene and hence can be quite different from the traditional thin film technology (Muñoz & Gómez-Aleixandre, 2013).

Structurally, graphene has extremely strong in-plane carbon-carbon bonds and very weak out-of-plane bonds. This makes it weakly interactive with the substrates supporting it, for instance, graphene-metal interactions are in the range of the van der Waals interaction (<100 meV per carbon atom) (Bartelt & McCarty, 2012). In response to such weak interactions, formation interference patterns known as the Moiré patterns are commonly encountered during graphene synthesis (Tang *et al.,* 2013). Such patterns happen when two grids are overlaid at an angle on each other, in this case, the lattices of graphene and metal substrate (Mattevi *et al.,* 2011).

Epitaxial growth of graphene from a silicon carbide (SiC) substrates is another method that has been successfully explored (Berger *et al*., 2004; Shivaraman *et al.,* 2009). As a semiconductor, SiC possesses superior properties that include; a wide band gap, a high thermal conductivity, a high critical electric field and high electron mobility (Kimoto, 2019). These excellent properties make it highly applicable in electronic devices operating in high temperature and high-power environments (Chen *et al.,* 2010; Kimoto, 2019). Epitaxial growth on SiC is highly promising as a future method of graphene production on a large scale (Kim *et al*., 2009). It involves heating single crystal SiC substrates to high temperatures ranging from 1200 to 1600 °C in a vacuum (Shivaraman *et al.,* 2009). When two grids are overlaid, the film and substrate remain attached to each other with atoms of the different materials diffusing until they reach a kink site, where they are incorporated into one lattice (Shivaraman *et al.,* 2009).

Other methods include; use of colloidal suspension (Balandin et al., 2008), unzipping of CNTs (Kosynkin et al., 2009) and reduction of graphene oxide have been majorly exploited (Khalil et al., 2016). Some of the advantages and disadvantages of these graphene synthesis techniques are presented in Table 2.2 (Khalil et al., 2016).

Table 2.2: Advantages and disadvantages of some of the common synthesis procedures of graphene (Source: Khalil *et al.*, 2016)

Procedure	Beneficial Aspects	Limitations
Micromechanical exfoliation	• Simple process. • Few defects. • Excellent quality of graphene. • Suited for fundamental research.	• Poor reproducibility. • Not amenable for large scale production.
CVD	• Large area (up to ~1 cm^2). • Limited number of defects. • Mass production. • High quality graphene.	• Expensive. • Poor scalability.
Epitaxial growth	• High quality of graphene. • Few defects.	• High cost. • Requires high temp.
Colloidal suspension	• Scalable. • High volume of production. • Suitable for multipurpose chemical functionalization.	• Significant number of defects.
Unzipping of CNTs	• Scalable with controlled widths and edge structures. • Better control of chemical functionalization and edge quality.	• Low yield. • More expensive in respect to chemical exfoliation.
Reduction of graphene oxide	• Economical and facile technique.	• Significant number of defects.

2.7.5 Graphene Characterization: Microscopy and Spectroscopy Techniques

Since the inception of graphene, various techniques have been applied in the detection and characterization of single-layer to multilayer graphene with a view of understanding its many unique properties. Some of the common methods include;

optical microscopy (Blake *et al.,* 2007; Casiraghi *et al.,* 2007), transmission electron microscopy (TEM), scanning electron microscopy (SEM), atomic force microscopy (AFM) (Geim & Novoselov, 2007; Park *et al.,* 2012), UV-Vis and Raman spectroscopy (Ferrari, 2007; Gupta *et al.,* 2006), and scanning tunneling microscopy (STM) (Xu *et al.,* 2009). However, most of these methods are costly due to expensive equipment involved and the need for highly skilled personnel (Chen *et al.,* 2010). They are also time-consuming in terms of sample preparation, image processing and analysis, making them out of reach for many researchers. Earlier studies (John *et al.,* 2015) reported contrast spectra analysis of optical microscopy images as an efficient and easy-to-use method for identifying and determining the thickness of layered graphene samples. It is based on the optical contrast differences between the layered graphene samples and the glass substrate as a standard reference from which sample thickness can be easily evaluated.

Optical image contrast analysis offers an easy-to-use method to identify and classify stacked graphene samples according to the number of layers. In this case, the optical contrast differences between the MLG samples as shown in Figure 2.9 and the substrate for any 2-D material could be easily determined without using complex calculations (John *et al.,* 2015).

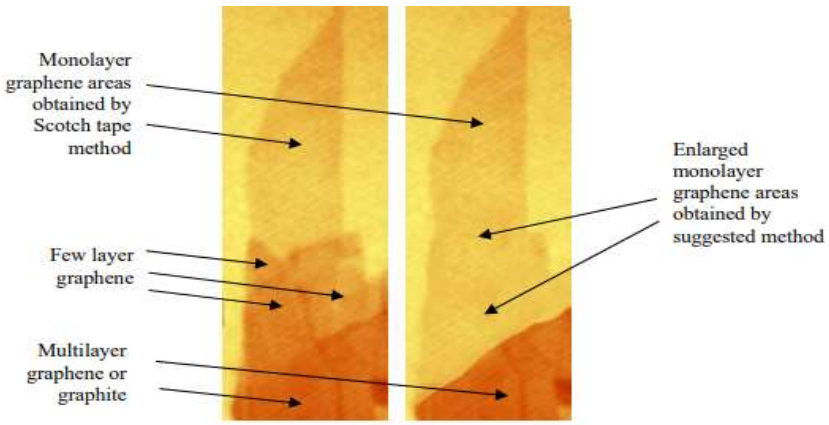

Figure 2.9: Optical images of exfoliated graphene flake showing contrast difference between monolayer, few-layer and multilayer graphene at 100X magnification (Source: Shmavonyan *et al.,* 2013)

Under optical microscopy, the contrast intensity occurring within the interface of air/substrate and the GL, can be viewed directly (Skulason *et al.,* 2010). In this case, the air/substrate interface intensity is the reference intensity. For exfoliated graphene flake, the optical intensities of the reflected or transmitted light through the GL, I_G, and intensity reflected or transmitted from the substrate, I_S, can be measured (Skulason *et al.*, 2010).

Based on these measurements, the reflection (C_R) or transmission (C_T) optical contrast can be calculated as in equations (2.28) and (2.29);

$$C_R = \frac{(I_S - I_G)}{I_S} = \frac{(R_S - R_G)}{R_S} \quad \text{.....2.28}$$

$$C_T = \frac{(I_S - I_G)}{I_S} = \frac{(T_S - T_G)}{T_S} \quad \text{.....2.29}$$

where R_G, T_G are the reflectance and transmittance spectra for the air/graphene/glass interface while R_S, T_S are the reflectance and transmittance spectra for the bare air/glass interface.

By choosing the right substrate thickness, a visible contrast could clearly identify individual GL from a flake (Jung *et al.,* 2007; Reina *et al.,* 2009). Application of *ImageJ* allows for the processing of such images by first presenting it in the red, green, blue (RGB) format. The optical transmittance is first captured with the image intensity scaled under 256 gray level where 0 represents the darkest while 255 represents the brightest region (Wang *et al.,* 2019). This is then converted to actual contrast based on the appropriate channel and according to equation (2.30);

$$C_{T\delta} = \frac{(T_{S\delta} - T_{G\delta})}{T_{S\delta}} \quad \text{.....2.30}$$

where δ represents the R, G, or B channels (Ni *et al.,* 2007).

Raman spectroscopy is a technique that is useful in the study of rotational, vibrational or other low-frequency modes (Jorio, 2012). Interaction between a laser beam and a molecule or atom may lead to; absorption, scattering or reflection (Childres *et al.*, 2013). Raman effect deals with inelastic photon scattering, whereby, a monochromatic laser interacts with the molecular vibrational modes and phonons in a sample, resulting in a down (Stokes) or up (anti-Stokes) shifts in the laser energy (Childres *et al.*, 2013). Every material has a unique shift in wavelength (Jorio, 2012). Figure 2.10 shows the three main energy shifts created during light scattering interactions. The larger fraction of the light scattered undergoes Rayleigh scattering where the emitted and incident photons have the same energy (Lin *et al.*, 2010).

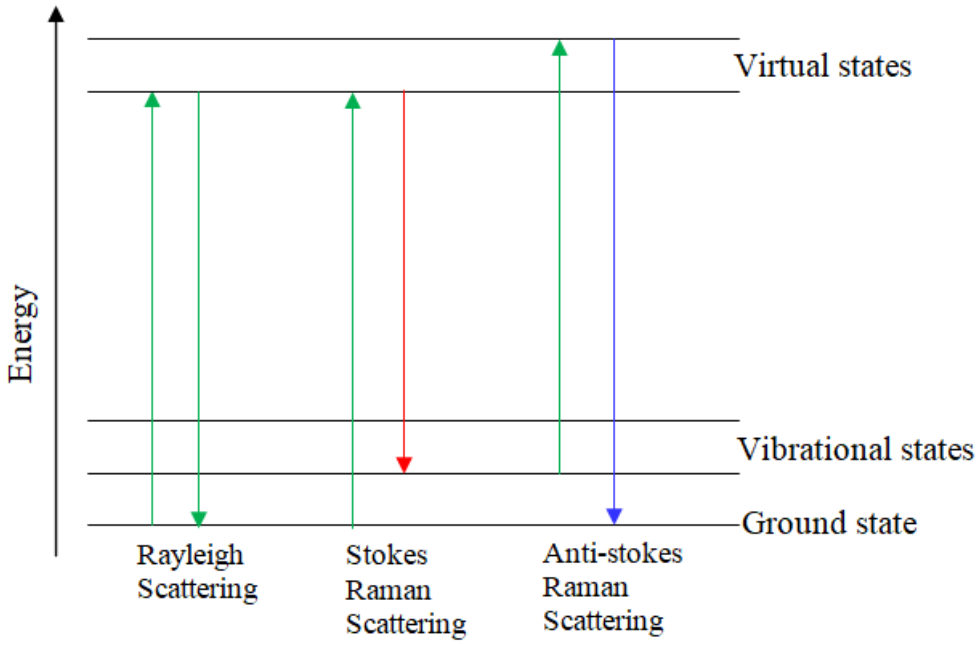

Figure 2.10: Energy shifts created in light scattering interactions, showing the vibrational modes. Stokes and anti-stokes results from inelastic scattering (Source: Lin *et al*., 2010)

In graphene and other sp^2 materials, identification of their vibrational modes (Qiu *et al.*, 2016) and subsequent characterization in terms of disorder, thickness, doping, strain, edge and grain boundaries, and thermal conductivity has been simplified by use of Raman spectroscopy (Jorio, 2012; Campos *et al.*, 2018). According to various studies, Raman spectroscopy is one of the easiest and most acceptable scientific ways

of identifying single layers in graphene (Qiu *et al.,* 2016; Wu *et al.,* 2018). The shifts in Stokes phonon energy resulting from laser excitation generates two important vibrational modes in the Raman spectrum, recognized as; G and 2D modes, with respective peaks existing at ~1580 cm^{-1} and ~2700 cm^{-1} (Ferrari *et al.,* 2006; Qiu *et al.,* 2016) and another called D band at 1350 cm^{-1} (Ferrari *et al.,* 2006).

Figure 2.11 (a–e) shows Raman spectra recorded in different points of the surface of the GL depicting the behavior of G and 2D modes (bands) for an SLG, FLG, MLG and bulk HOPG (Qiu *et al.,* 2016).

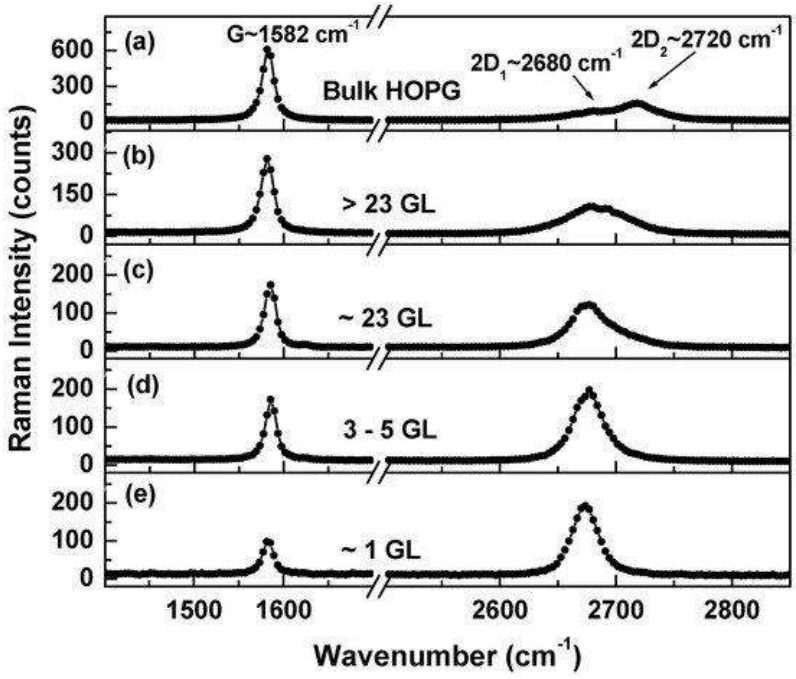

Figure 2.11: Raman spectra (a–e) recorded in different points of the Gr layer surface showing the trend of G and 2D bands for a SLG, a FLG, MLG and bulk HOPG (Source: Qiu *et al.,* 2016).

The Raman spectrum also shows an evolving position, shape, and intensity changes with the number of graphene layers (N) when recorded from different spots of the sample material. For bulk graphene, the 2D band is observed to split into $2D_1$ (~2680 cm^{-1}) and $2D_2$ (~2720 cm^{-1}) bands, arising from a second-order Raman scattering (Qiu *et al.,* 2016). However, as the number of layers decreases, a highly intense 2D band (2700 cm^{-1}) shifts to lower values observed (Wang *et al.,* 2017). This

demonstrates the intrinsic inhomogeneity of a Gr sample in terms of the number of layers. The ratio of G and 2D peak intensities (I_D/I_G), which has also been shown to vary with the decrease in GL, can also be employed to characterize the level of disorder in graphene (Childres *et al.*, 2013).

To understand the behavior and application of various materials, studying their optical properties such as absorbance, transmittance, reflectance, scattering, and fluorescence is important (Germer *et al.,* 2014). In DSSCs, these properties dictate the resulting PCE, and can be determined over the UV-Vis-NIR spectrum region using spectrophotometry techniques.

To measure a sample transmission, a single beam configuration is employed, and the transmission normalized against air as the reference to provide data based on the relationship between transmission, reflectance, and absorption as given by equation (2.31);

$$A = T + R \quad \text{.....2.31}$$

where; A = absorbance, T = transmittance and R = reflectance.

Therefore, from the single beam transmission spectra, the resultant transmittance equation (2.32) is given by;

$$T(\%) = \frac{I_{sample}}{I_{reference}} \times 100 \quad \text{.....2.32}$$

Since the spectrophotometer uses the incident radiant flux as the reference beam, the, reflectance measurements can be computed based on the most general definition that involves a ratio of the reflected radiant flux to the incident radiant flux, as in equation (2.33) (Palmer, 1995);

$$R(\%) = \frac{\Phi_r}{\Phi_i} \quad \text{.....2.33}$$

where Φ_i is the incident (usually air) while Φ_r is the reflected radiant flux.

2.8 Nanoparticles in Photovoltaics

2.8.1 Introduction to the Nanoworld

In his lecture, Richard Feynman brought to awareness the presence of "plenty of room at the bottom" (Feynman, 1992), through which the audience was charged to open up a new field of research in Physics. In this regard, the term nanotechnology was coined in the 1970s (Taniguchi *et al.,* 1974) with great progress and remarkable discoveries made in the "nanoworld" (Binnig and Rohrer, 1987; Kroto *et al.,* 1985). Nanoparticles are specified as particles having two or more dimensions and in the size range of 1 - 100 nm (Alanazi *et al.,* 2010).

Over time, studies have revealed that potential applications of nanomaterials are vast (Aruna *et al.,* 2015; Jain *et al.,* 2008; Wu *et al.,* 2018). The growing interest to study nanomaterials is footed on the fact that such materials show unique properties from their bulk material counterparts and that their properties can be tuned via size and shape control (Burda *et al.,* 2005; Dagher *et al.,* 2014). These unique properties bridge the bulk materials and the atomic structures (Jana *et al.,* 2016; Jayawardena *et al.,* 2013). For instance, a slab of gold is a yellowish conductor with a high melting point, while AuNPs are semiconductors with color variation from red to purple and a much lower melting point (Jana *et al.,* 2016).

2.8.2 Quantum Confinement (QC) in Nanoparticles

The concept of nanoscale is of importance in materials due to the QC effect of the electrons. Quantum confinement is defined as; "the changes in the atomic structure properties as a result of the direct influence of the ultra-small length scale on the energy band structure" (Kuchibhatla *et al.,* 2007). Such changes can be reflected in the optical properties or catalytic reactivity of the material. Nanomaterials express the QC functionalities where their properties can be tuned via size, chemical composition, binding strength between the core and ligand shell, overall charge, and stability within a given medium (Reimann & Manninen, 2002). Through QC, electrons can be described in terms of their energy levels, potential wells, energy

bands and band gaps (El-Sayed, 2004). Figure 2.12 shows a schematic representation of QDs due to the QC where the QC effect increases with decreasing QD size.

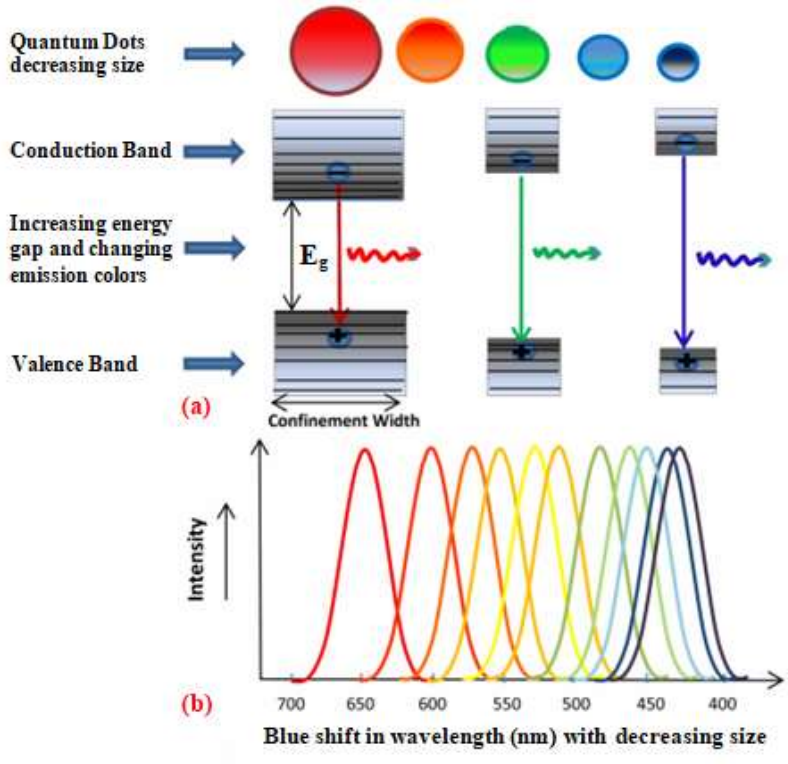

Figure 2.12: A schematic representation of energy level splitting in QDs due to the QC. The QC effect increases with decreasing QD size (Source: Koole *et al*., 2014).

The VB and CB are found to split into quantized energy levels as the size of a particle decreases (Figure 2.12 a) (Koole *et al*., 2014; McKittrick & Shea-Rohwer, 2014). Similarly, the energy gap increases, while the color of the emissions is found to change. In AuNPs, a blue shift in wavelength occurs (Figure 2.12 b). Upon QD excitation by a photon, a VB electron is promoted to the CB just like in the bulk nanomaterial. This generates an exciton (electron-hole pair). In the case of recombination, a radiative process may occur in which a photon is emitted, with its energy depending on the band gap energy.

Figure 2.13 below shows a representation of the exciton resulting from photon absorption in a QD.

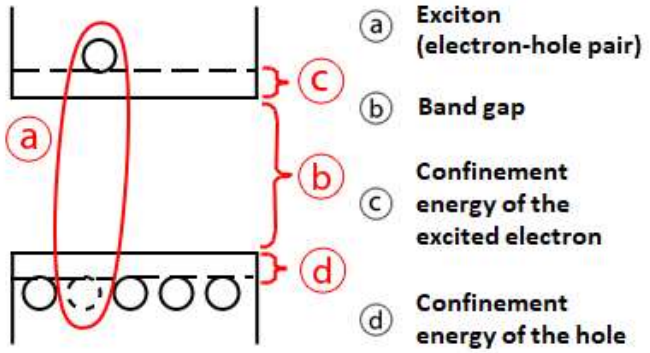

Figure 2.13: A representation of the exciton resulting from photon absorption in a QD (Source: McKittrick & Shea-Rohwer, 2014).

In a simplified model, the energy of the emitted photon when absorbed in a QD can be described as the sum of (a) the bound energy of the excitons, (b) the band gap energy and the confinement energies of the (c) excited electron and (d) hole (McKittrick & Shea-Rohwer, 2014).

The reduced size causes more confinement of the electron in a small space (quantum box) within the particle. The magnitude of resulting confinement energy can be described by equation (2.34).

$$E_{confinement} = \frac{\pi^2\hbar^2}{2a_0^2}\left(\frac{1}{m_e^*}+\frac{1}{m_h^*}\right) = \frac{\pi^2\hbar^2}{2m^* a_0^2} \quad \text{.....2.34}$$

where m^* is the reduced mass of the exciton system, a_0 is the radius of the QD, while m_e^* and m_h^* are the effective masses of the electron and hole respectively.

As the NP size reduce below the natural length scale of the e^-/h^+, an increase in band gap energy and quantization of the energy levels occurs. This length is also called the Bohr exciton radius (Barbagiovanni *et al.*, 2014) and defined as in equation (2.35):

$$a_b^* = \varepsilon \frac{m_e}{m^*} a_b \quad \text{.....2.35}$$

where ε is the material dielectric constant, m_e is the electron rest mass, a_b represents the Bohr radius of the hydrogen atom (~0.053 nm).

Due to the Coulombic attraction existing between the oppositely charged hole and electron of the exciton, there exist an associated additional energy called excitons energy ($E_{exciton}$) given by equation 2.36:

$$E_{exciton} = -\frac{1}{\varepsilon^2}\frac{m^*}{m_e}R_y \text{ ……..……..……2.36}$$

where R_y is the Rydberg energy (~13.6 eV) (Barbagiovanni *et al*., 2014).

For a fluorescing photon, the total energy can therefore be modeled as the sum of the QD band gap energy, the quantum confinement energy, and the bound exciton energy, as given in equation 2.37.

$$E_{total} = E_g + E_{confinement} - E_{exciton} = E_g + \frac{\pi^2\hbar^2}{2m^* a_0^2} - \frac{1}{\varepsilon^2}\frac{m^*}{m_e}R_y \text{ ……...2.37}$$

In such a case, over the Vis region, the band gap emission shifts from red to blue emission as the particles in the clusters decrease in size. Additionally, in the size regime less than ~10-100Å, NPs are highly controllable, hence can be easily optimized for a variety of applications (Melville and Kapelewski, 2015).

2.9 Noble Metal Nanoparticles

Metallic NPs are synthesized from different metal precursors. Noble metals commonly used in DSSC CE include Pt, Au and Silver (Ag). For Au and Ag, their high electro-catalytic activity properties have also been investigated and employed in the reduction of redox couples in liquid electrolytes (Ye *et al.,* 2015). Nanoparticles of noble metals, such as those of Au and Ag and whose sizes are smaller than the light wavelength, strongly absorb and scatter the visible spectrum due to the dipolar excitations occurring as localized surface plasmon resonance (LSPR) (El-Sayed, 2001; Jain *et al.,* 2008). This is due to the collective oscillation of free electrons

within the CB from one NP surface to the other when such electrons interact with light (Long *et al.*, 2009; Marinakos *et al.*, 2007; Willets and Van Duyne, 2007).

Within the nanoparticle surface, such plasmon resonances permit enhancement and manipulation of large resonants of the local electromagnetic fields inside and near the NP (He and Lu, 2014; Moskovits, 1985; Sokolov *et al.*, 1998). Figure 2.14 shows an illustration of plasmonic excitation through polarization of metallic NPs.

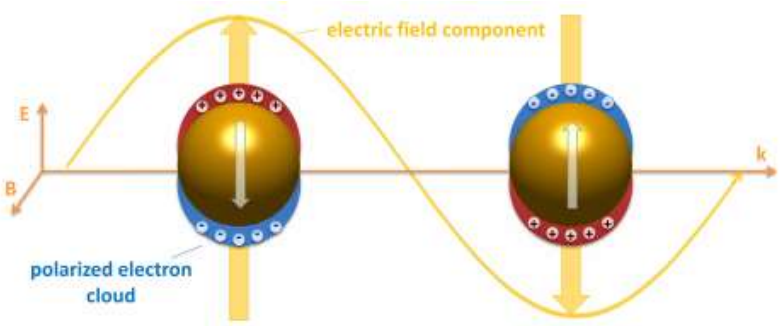

Figure 2.14: An illustration of plasmonic excitation through polarization of metallic NPs. At resonance, the plasmons oscillate with a phase difference of 90° (Source: Trügler, 2016).

When an electromagnetic radiation interacts with a metallic NP of size in the order of magnitude as the Bohr radius, the electron gas charges and moves to the opposite sides of the NP surface generating a restoring force. The dipole of the free electrons then oscillates with similar frequency to attain a phase difference of 90° at resonance. (Trügler, 2016).

2.9.1 Colloidal gold Nanoparticles

As a solid, gold presents itself as a yellowish-gold colored element with a dense and soft structure. Its atomic number is 79 and a standard atomic weight of ~197 g/mol. Gold melts at 1064.63 ^{o}C, boils at 2807 ^{o}C, it's inert and shows stability in most media. It is also known to have high thermal and electrical conductivity (Jain *et al.*, 2008; Link and El-Sayed, 2000). On the other hand, at nanoscale, electrons in AuNPs oscillate at a frequency capable of absorbing the visible light. This absorption gives rise to the observed vivid characteristic colors of AuNPs, with the LSPR features

showing sensitivity to the NPs size, shape, and concentration (Jain *et al.,* 2008; Link & El-Sayed, 2000; Mie, 1976). As such, implementations of noble metallic NPs such as gold in optoelectronics have stimulated great research interests fundamentally. This aims at exploiting the many applications it promises in photovoltaics (Atwater, 2007; Polman & Atwater, 2012), surface enhanced Raman scattering (SERS) (Moskovits, 1985), developing of new medical diagnostic techniques (Anker *et al.,* 2008) and various photocatalytic processes (Zhang *et al.,* 2013).

For larger NPs (diameter D ≥ 20 nm), the resonant peak energy decreases as the NPs sizes increase (Jain *et al.,* 2008). As the size of NPs increases, the distance between them decreases due to aggregation resulting in peak broadening and red-shifting (Zuber *et al.,* 2016). Moreover, due to their large optical cross-section, they scatter much of incident light creating an electromagnetic retardation effect (Berciaud *et al.,* 2005). On the other hand, for smaller NPs (D < 20 nm), their intrinsic size effects dominate while their extrinsic size-effects are neglected (Moskovits, 1985). Usually, the size-dependent properties of nanomaterials directly relate to surface atoms. Thus, by combining the intensity of the SPR peak, peak wavelength and broadening, the size of AuNPs can be determined (Zuber *et al.,* 2016).

When light is incident on small-sized AuNPs, it excites surface plasmons in the NPs. For individual particles, Mie Gustav (1976) theoretically described this classical effect in terms of extinction cross-section. By considering a metal sphere, surrounded by a frequency-dependent dielectric and homogeneous medium, Mie solved Maxwells equations for a plane wave incident on the sphere. For spherical NPs with diameters (D) less than one-tenth the wavelength of incident light, the significant solution derived from Mie theory in terms of extinction coefficient is given by equation (2.38) (Kheirandish *et al*., 2020);

$$C_{ext} = \frac{3\pi^2 D^3 \varepsilon_m^{3/2}}{\lambda} \frac{\varepsilon_{\mathrm{Im}}}{\left(\varepsilon_{\mathrm{Re}} + 2\varepsilon_m\right)^2 + \varepsilon_{\mathrm{Im}}^2} \quad \text{.....2.38}$$

where; λ is the incident radiation wavelength and ε_m is the dielectric constant of the medium, while $\varepsilon_{\mathrm{Re}}$ and $\varepsilon_{\mathrm{Im}}$ are the real and imaginary parts of the dielectric function for metallic NPs, respectively.

For a non-conducting material, the frequency-dependent dielectric $\varepsilon(\omega)$ function is described by the Drude model given by equation (2.39);

$$\varepsilon(\omega) = 1 - \frac{\omega_{sp}^2}{\left(\omega^2 + i\omega\gamma\right)} = 1 - \frac{\omega_{sp}^2}{\left(\omega^2 + \gamma^2\right)} + i\frac{\omega_{sp}^2\gamma}{\omega\left(\omega^2 + \gamma^2\right)} \quad \text{.....2.39}$$

where ω is the angular frequency, γ is a damping coefficient and ω_{sp} is the Drude surface plasmon frequency, given by equation (2.40) (Arboleda *et al.*, 2016);

$$\omega_{sp} = \left(\frac{ne^2}{\varepsilon_0 m_e}\right)^{\frac{1}{2}} \quad \text{.....2.40}$$

Equation shows $\varepsilon(\omega)$ is expressed as equation (2.41);

$$\varepsilon(\omega) = \varepsilon_{\mathrm{Re}}(\omega) + i\varepsilon_{\mathrm{Im}}(\omega) \quad \text{.....2.41}$$

where;

$$\varepsilon_{\mathrm{Re}} = 1 - \frac{\omega_{sp}^2}{\omega^2 + \gamma^2} \quad \text{.....2.42}$$

$$\varepsilon_{\mathrm{Im}} = \frac{\omega_{sp}^2\gamma}{\omega\left(\omega^2 + \gamma^2\right)} \quad \text{.....2.43}$$

In metallic NPs, the position of SPR is controlled by $\varepsilon_{\mathrm{Re}}$. For small NPs (<10 nm), and whose sizes are much less than the wavelength of the light, dipole behavior is exhibited hence contributes more to dielectric response. Therefore, from the extinction coefficient equation, the occurrence of dipole response frequency is maximized by the resonant condition called Fröhlich condition of LSPR (Khlebtsov, 2008) and given by equation (2.44);

$$\varepsilon_{\mathrm{Re}} + 2\varepsilon_m = 0 \quad \text{.....} \quad 2.44$$

The resonance line width, referred to as full width at half maximum (FWHM) describes the SPR broadening (Amendola and Meneghetti, 2009). The FWHM is described by $\varepsilon_{\mathrm{Im}}$, which occurs through damping. For noble metal NPs such as Au, both $\varepsilon_{\mathrm{Re}}$ and $\varepsilon_{\mathrm{Im}}$ depends on the size of NPs, FWHM broadening and LSPR position.

For colloidal NPs in an organic medium such as Na_3Ctr, their optical properties responses are altered by their respective properties and salt concentration. Again, from Drude model, the size dumping factor γ_s is given by equation (2.45) (Kolwas and Derkachova, 2013);

$$\gamma_s = \frac{v_F}{l_0} \quad \text{.....} \quad 2.45$$

where v_F is the Fermi velocity, equal to $1.4 \times 10^6 ms^{-1}$ for gold, and l_0 is the mean free path.

For NPs $D << l_\infty$, LSPR dominates resulting in more surface interaction of electrons $2Av_F / D$, creating a new size-dependent damping given by (Arboleda *et al.*, 2016);

$$\gamma_s(D) = \gamma_0 + \frac{2Av_F}{D} \quad \text{.....} \quad 2.46$$

where A is a factor on the metal properties and describes scattering processes within the particle, and γ_0 is the damping constant for free electrons.

Since the number of plasmons is proportional to the NP volume, the size dependent correction in γ(D) increases with the surface-to-volume ratio i.e. 1/D. The interband transitions of bound electrons also contributes to the dielectric function, $\varepsilon(\omega)$. These transitions are expressed in a standard Lorentz form (Arboleda *et al.*, 2016) as;

$$\varepsilon_{ib}(\omega) = 1 + \frac{\omega_1^2}{\left(\omega_0^2 + \omega^2 + i\omega\gamma_b\right)} \quad \text{.....2.47}$$

where ω_0 is the frequency of the oscillating bound electron upon applied electric potential, γ_b is the damping of bound electrons and ω_1 is the frequency related to the density of bound electrons. The resultant metal dielectric function containing the free electrons term $\varepsilon(\omega)$ and bound electrons term $\varepsilon_{ib}(\omega)$ becomes;

$$\varepsilon(\omega) = \varepsilon_{ib}(\omega) + 1 - \frac{\omega_{sp}^2}{\left(\omega^2 + i\omega\gamma_b\right)} \quad \text{.....2.48}$$

2.9.2 Synthesis Methods for Colloidal AuNPs

Colloidal gold is a solution containing micro- or nano-sized gold particles suspensions. Presently, much attention has been on synthesis and characterization of metallic NPs with small and uniform sizes for various applications (Dagher *et al.*, 2014; González *et al.*, 2005; Polte, 2015). Several physical, chemical, photochemical and biological methods have been proposed and used to prepare NPs (Slepička *et al.*, 2020). These methods are classified as dispersing, involving top-down methods or condensing, also referred to as bottom-up methods.

Dispersion methods involve destruction of the material crystal lattice (Slepička *et al.*, 2020). Through a top-down approach, larger molecules are decomposed into smaller units first, before conversion into the appropriate NPs. One of the commonly employed dispersion methods is the PVD, which employs laser ablation and cathode sputtering (Kabashin *et al.*, 2003; Siegel *et al.*, 2012). In an aqueous solution of β-cyclodextrin (CD) compound, laser ablation of a gold metal plate produces stable AuNPs, exhibiting LSPR peak at 520 nm (Kabashin *et al.*, 2003). Room temperature metal sputtering also generates reproducible AuNPs with narrow size distribution (Siegel *et al.*, 2012). Although the PVD methods show viability of a wider spectrum of NPs that may be prepared, they require expensive apparatus making them out of reach for many laboratories. Biosynthesis or green synthesis of environmentally

friendly AuNPs has shown potential for high yields, although the resulting NPs are more applicable in bio-systems with their toxicities not well understood (Jain *et al.*, 2006; Parveen *et al.*, 2016).

Condensation methods are based on chemical reactions and follow the route of; reduction in solution followed by NP precipitation, formation and stabilization (Polte, 2015; Slepička *et al*., 2020). For small and uniform aqueous metallic NPs, chemical reduction of a metal salt in aqueous form by a reducing agent is the most widely used synthesis method (Polte, 2015). Some of these reducing agents include sodium citrate, sodium borohydride, phosphor or hydrogen (Agunloye *et al.*, 2018; Pal *et al.*, 2015). This reduction technique is based on classical nucleation theory, which is purely thermodynamic and explains the growth of particles (Thanh *et al.*, 2014; Turkevich *et al.*, 1951). According to Turkevich, aqueous Au (III) solution is reduced close to the boiling point (~100 ^{o}C) by citrate ions to produce a stable solution of AuNPs (Turkevich *et al.*, 1951). A later modification of this reduction process by Frens included controlled size formation (Frens, 1973) through variation of the trisodium citrate to gold ratio.

In practice, Au (III) ions are initially added into deionized (DI) water in the form of hydrogen tetrachloroaurate ($HAuCl_4.3H_2O$). When Na_3Ctr is introduced in excess to the boiling $HAuCl_4.3H_2O$ solution, the citrate ions ($C_6H_5O_7^{3-}$) work as a two-electron reducing, a protective capping agent, and a pH mediator (Ji *et al.*, 2007; Patungwasa and Hodak, 2008). In the process, they are oxidized forming acetone dicarboxylate ions ($C_5H_4O_4^{2-}$), hence pre-determining the size and distribution of the NPs (Jana *et al.*, 2001). The reaction process can be described by half-reactions given in equations (2.49) and (2.50);

$$Au^{3+}(aq) + 3e^- \rightarrow Au(s) \quad \text{.....2.49}$$

$$C_6H_5O_7^{3-}(aq) + H_2O(l) \rightarrow C_5H_4O_4^{2-}(aq) + CO_2(g) + H_3O^+(aq) + 2e^- \quad \text{.....2.50}$$

This method produces gold NPs of an average diameter of ~20 nm, in addition to a narrow size distribution and good reproducibility (Turkevich, 1985; Turkevich *et al.,* 1951). This makes it the method of choice for most researchers.

Size characterization of colloidal AuNPs has been previously performed based on various techniques (Khlebtsov, 2008; Matsuura *et al.,* 2018). Faraday's-Tyndall effect is a phenomenon associated with plasmonic light scattering in NPs (Yu *et al.,* 2015) where the longer-wavelength light is transmitted more while the shorter wavelength light undergoes more reflection through scattering. The presence of AuNPs in a sol can be verified based on the color and Faraday's-Tyndall Effect. When white light illuminates a metallic NP, the plasmonic resonance determines the color we observe in the NPs. The Tyndall effect occurs when a light beam is passed through a colloidal suspension containing NPs of size less than 100 nm. The particles scatter a portion of the beam leading to its divergence hence creating the observed optical effect. Within the gold colloids, this light scattering is very significant, particularly at the SPR band of the AuNPs.

2.9.3 Characterization Techniques for Colloidal Gold

Characterization of AuNPs is based on their distinct optical and physical properties. This depends on their sizes, shapes, concentration, surface structures and agglomeration state. Some of the common techniques used in characterization of AuNPs include; UV-Vis spectroscopy (Alzoubi *et al.,* 2015), SEM/TEM (Khan *et al.,* 2019; Pimpang and Choopun, 2011) and dynamic light scattering (DLS) (Khlebtsov 2008; Zheng *et al.,* 2016). Others are AFM (Li *et al.,* 2013), darkfield microscopy (DFM) (Wang *et al.,* 2011), gel electrophoresis (Liao *et al.*, 2017) and X-ray diffraction (XRD) (Hu *et al.,* 2006). In all these techniques (Piwoński *et al*., 2013; Boyd and Cuenat, 2011), the particle size and distribution measurements are done in solution or after the sample dried.

For microscopy techniques, XRD and DFM, it is possible to generate information about the particle size and morphology at the same time making them more versatile (Pimpang & Choopun, 2011). However, sample preparation is time-consuming since the NPs are very sensitive and must be deposited on a well-characterized substrate. It

also require high precision and use of particular reagents (Grobelny, *et al.,* 2011). Moreover, in the case of polydisperse samples, particles aggregation and sample fractionation during drying may be unavoidable. Gel electrophoresis (Hasenoehrl *et al.,* 2012), analyzes NPs by separating them based on their size, shape and charge (Xu *et al.,* 2007) to study their migration patterns (migration direction and distance). It is more applicable in bioassays to specify the binding of target analytes (Liao *et al.,* 2017) by analyzing the migration patterns alteration upon modification of gold surface charge with charged biomolecules. However, the high system voltage could induce external charges hence interfering with the said patterns to give force results. Among these techniques, the most commonly used ones in the characterization of colloidal suspensions are the DLS and UV-Vis spectroscopy. This is because they are low cost, fast and easy to operate, hence offering sensitivity, simplicity and selectivity to NPs, short time of measurement, and require no complex calibration (Alzoubi *et al.,* 2015; Khan *et al.,* 2019).

The DLS technique is preferred in measurement of size and size distribution of NPs in a colloidal solution (Khan *et al.,* 2019). It involves illuminating the colloids with a laser beam, detecting fluctuations in scattered light and then analyzing velocity of the NPs to determine their hydrodynamic sizes (Zheng *et al.,* 2016). The DLS measures the size of the physical NP physical core, surface coating and NP solvent layer (Sakurai *et al.,* 2010). Therefore, any molecular conjugation to the AuNP surface increases its hydrodynamic size, DLS a very sensitive technique for evaluating surface modifications (Sakurai *et al.,* 2010). Other areas of application include AuNPs stability and detection for bioassays (Khan *et al.,* 2019). Although DLS is widely used in the characterization of monodisperse colloidal NPs, problems associated with the analysis of samples with large-size and multimodal distributions limits it popularity (Khlebtsov and Khlebtsov, 2011; Zanetti-Ramos *et al.,* 2009). During DLS measurement in polydisperse colloids, bigger particles tend to screen small ones making the latter invisible.

Ultraviolet-Visible (UV-Vis) Spectroscopy is one of the widely accepted, low-cost and easy to use characterization techniques commonly applicable in most research laboratories (Link and El-Sayed, 1999). It is based on molecular absorption of light

within the UV-Vis region, where the Vis absorption directly corresponds to the color of the chemicals involved. A beam of light with different wavelengths is passed through a sample and both the incident and the transmitted intensities of the beam measured. The sample absorbance is determined according to the Beer-Lambert law in equation (2.51) (Swinehart, 1962). Accordingly, the sample absorbance (A) at any particular wavelength in terms of incident (I_o) and transmitted beam intensities (I) as described by the Beer-Lambert law in equation;

$$A = \log_{10}\left(\frac{I_0}{I}\right) = C_{ext}\, C\, L \quad \text{.....2.51}$$

where C is the concentration of NPs/molecule, L is the optical path length over which the light passes through the sample and C_{ext} is the extinction coefficient defined in the terms of molar absorptivity (Ricci *et al.*, 1994). According to Beer-Lambert law, a sample of higher concentration exhibits higher absorbance levels.

Gold NPs are known to exhibit LSPR, characterized by strong absorbance bands in the Vis region, measurable by UV-Vis spectroscopy (Willets and Van Duyne, 2007). The LSPR peak wavelength increases with the NP size, with a significant red-shift observed for uneven NPs compared to a spherical NPs of equal size. A linear correlation exists between the peak optical density and the NPs in any colloidal sample (Jain *et al.*, 2008). Therefore, a change in the sample medium causes a change in the absorbance peak hence the peak wavelength, which generally occurs at ~520 nm and depends on the size of AuNPs (Alzoubi *et al.*, 2015).

Table 2.3 shows some of the size-dependent properties of AuNPs (up to 50 nm). The LSPR peaks and the molar extinction increases with increasing size of the AuNPs, while the particle concentration decreases with NPs sizes. For AuNPs with sizes between 5 and 15 nm, the LSPR peak wavelength ranges between 515 and 520 nm.

Table 2.3: Some size-dependent properties of gold nanoparticles (Source: Sigma-Aldrich, 2016)

Diameter (nm)	**Number of Nanoparticles/mL)**	**Peak SPR Wavelength (nm)**	**Molar Extinction ($M^{-1}cm^{-1}$)**
5	5.47×10^{13}	515-520	1.10×10^{7}
10	5.98×10^{12}	515-520	1.01×10^{8}
15	1.64×10^{12}	520	3.67×10^{8}
20	6.54×10^{11}	524	9.21×10^{8}
30	1.79×10^{11}	526	3.36×10^{9}
40	7.15×10^{10}	530	8.42×10^{9}
50	3.51×10^{10}	535	1.72×10^{10}

Figure 2.15 represents a typical UV-Vis absorbance spectra for gold nanospheres, showing the LSPR peak wavelength (λ_{LSPR}) and absorbance (A_{LSPR}) positions. The position of FWHM measurement necessary for analysis of the NPs dispersity behavior over the UV-Vis spectra is also shown (Alzoubi *et al.*, 2015).

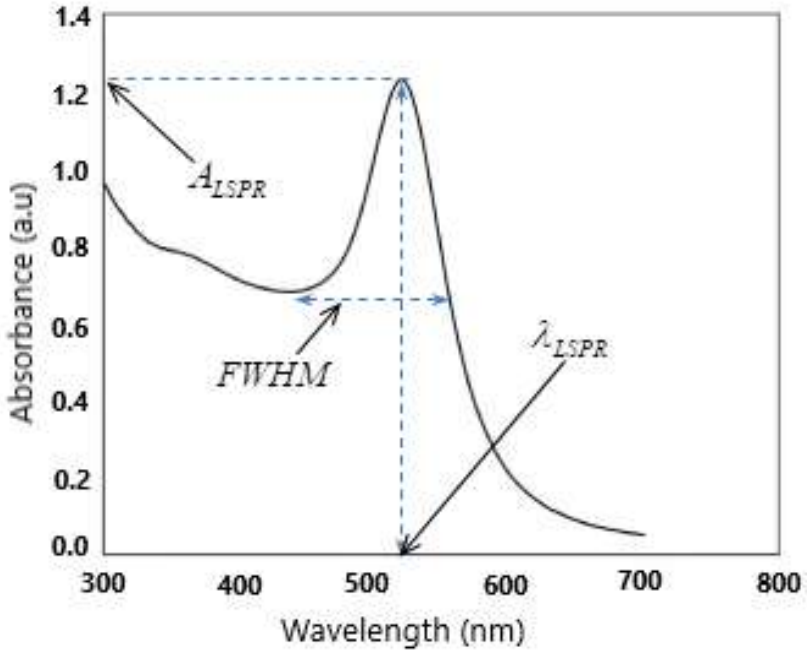

Figure 2.15: A typical UV-Vis absorbance spectra of gold nanosphere, showing LSPR peak wavelength (λ_{LSPR}) and absorbance (A_{LSPR}), and FWHM at approximately 520 nm (Source: Alzoubi *et al.,* 2015).

Reports indicate that the size of AuNPs and the molar concentration of Au(0) can be extracted from a UV-Vis spectra, using either position and extinction at LSPR or the ratio of extinctions at the LSPR peak wavelength and at 450 nm (A_{LSPR}/A_{450}) (Haiss *et al.,* 2007). From the sample solution UV-Vis absorbance spectra, LSPR peaks and FWHM analysis could be used to determine the NP size and distribution (Pimpang and Choopun, 2011). Figure 2.16 shows a general UV-Vis absorption spectra of NPs showing the influence of NPs size distribution on the FWHM value (Oliveira *et al.,* 2020). The distribution of NPs can be described either by a; (a) low FWHM value for monodispersity or (b) higher FWHM for polydispersity of the NPs.

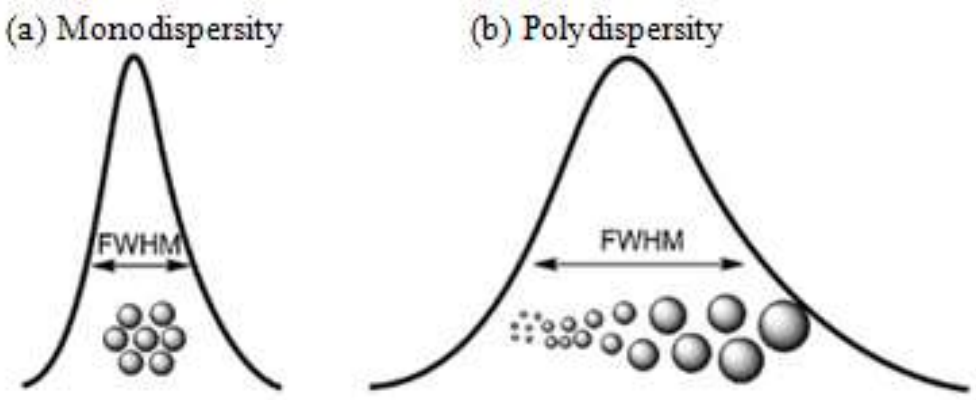

Figure 2.16: A general absorption spectra of NPs showing the influence of NPs size distribution on the FWHM value where (a) low FWHM value indicates monodispersity and (b) higher FWHM value indicate polydispersity of the NPs (Source: Oliveira *et al.,* 2020).

According to Hendel *et al.,* (2014), measurement of UV-Vis absorbance at 400 nm (A_{400}) is located between two decisive spectral regions hence appropriate for evaluating the concentration Au(0). Wavelengths below 400 nm are discouraged since the absorbance is highly influenced by organic substances. However, above 400 nm, the absorbance is influenced by the LSPR of the AuNPs (Hendel *et al.,* 2014), with slightly higher values allowed, where (A_{LSPR}/A_{450}) has been reported to generate fair NPs size estimates between 5 and 80 nm (Haiss *et al.,* 2007) based on equation (2.52);

$$D = Exp\left[B_1 \frac{\lambda_{LSPR}}{A_{450}} - B_2 \right] \quad \text{.....2.52}$$

where B_1 and B_2 parameters determined as 3.00 and 2.20 respectively for AuNPs.

2.9.4 Applications of LSPR in Gold Nanoparticles

With the unveiling of new NPs with different sizes and shapes, unraveling of the science of these particles and the application of computation methods to understand their behavior is ongoing (Bora *et al.,* 2019; Zeng *et al.,* 2015) for different uses.

Some observed important applications include; sensors (Jain *et al.,* 2008; Kravets *et al.,* 2012), surface-enhanced Raman scattering (SERS) (Li *et al.,* 2015; Wang *et al.,* 2010), medical diagnostics and therapy (Abadeer & Murphy, 2016; Conde *et al.,* 2012; Huang *et al.,* 2007), drug delivery (Mendes *et al.,* 2017; Patil *et al.,* 2010; Yang *et al.,* 2006) among others.

Metallic NPs used in graphene-metal nanocomposites have shown great potential in future plasmonic devices (Benítez–Martínez *et al.,* 2015; Bianco *et al.,* 2016; Wang *et al.,* 2012). Recently, much attention has been on synthesis and characterization of new NPs with different sizes and shapes for various applications based on their unique optical characteristics (Lemme, 2009). Small-sized gold spheres are known to localize incident light, extending its optical path length. This promotes their photo-energy harvesting ability due to their LSPRs properties (Dissanayake *et al.,* 2016; Jang *et al.,* 2014; Khalil *et al.,* 2016; Sarkar *et al.,* 2018). Application of AuNPs contact in metal surface modification has been on the rise. When Gr surface is covered with AuNPs, it exhibit increased light absorbance with enhanced photocurrents and efficiencies in the resulting DSSCs being recorded (Borowiec *et al.,* 2013; Hägglund *et al.,* 2008; Lin *et al.,* 2012; Qu *et al.,* 2011). Recent advances on the intersection of the plasmonics and PVs have been made, and new options for SC designs created (Atwater & Polman, 2010). Nanostructuring has also made it possible to tailor surface morphologies that maximize excitons dissociation hence providing efficient charge transport pathways in the modified cells (Watkins *et al.,* 2005). This application forms part of the purpose of this research, with cell modification through a restructuring of the CE design being the focus.

2.10 Composite Dye-Sensitized Solar Cells

2.10.1 FTO as a Base Material for DSSCs

Transparent conductive materials (TCMs), as suggested by the name, are materials possessing both optical transmission and electrical conductivity properties (Ginley & Perkins, 2011), widely useful in thin film SCs for transmission of light and collection of charge carriers (Zhang, 2018). The range of the materials include; wide-band-gap semiconductors, doped organic polymers, metal films or metal nitrides and finds

applications in; displays, photovoltaics, transparent electronics, window glass, and many other technological areas (Ginley & Perkins, 2011; Granqvist, 2007). Currently, TCOs, which are either *n*- and *p*-type semiconductors, form the preferred choice of TCMs. Their band gaps, which are higher than 3 eV, allows them to be transparent within the visible light spectrum (~1.8 - 3.0 eV) (Fortunato *et al.*, 2007). To permit high conductivity, these oxides are often doped with other elements. The most commonly used binary n-type TCOs are Indium (III) oxide (In_2O_3), Zinc (II) oxide (ZnO) and Tin (IV) oxide (SnO_2) (Fortunato *et al.*, 2007). Fluorine doped-SnO_2, commonly referred to as FTO, has been widely used as a base material for CEs and PAs in DSSCs. This choice is motivated by its high transparency (80%) even with inclusion of the glass substrate, and its fair sheet resistance (10 Ω/sq) making it a promising electrode in SCs (Zhang, 2018). Additionally, owing to its ease of deposition, FTO coatings are often integrated into glass manufacturing lines for mass production, vanishing PV markets with low-cost FTO coated glass modules, appropriate for thin-film PV application (Zhang, 2018).

2.10.2 Composite Electrodes

Structurally, a composite or hybrid CEs involve combining two or more component materials based on their merits and compatibility. The resulting DSSC can be regarded as a hybrid or composite cell. Carbonaceous materials and metal NPs have been found to fit very well in this development (Ye *et al.*, 2015). Platinum-based CEs are the most common due to their excellent and desired electro-catalytic properties. On the other hand, ultrathin Pt films, which have been conventionally used in CEs, create high defect points resulting in a reduced efficiency. Out of these challenges, the need for investigation and development of new and possibly hybrid CE incorporating other alternative materials has been high (Mehmood *et al.*, 2014; Ye *et al.*, 2015). However, the conversion efficiencies accrued from them need to be improved compared to noble materials performance. In this work, CVD single-layer graphene on FTO was used as a substrate for the Pt, AuNPs and the AuNPs/Pt as CE modules for the different DSSCs. Photovoltaic performance of the fabricated composite DSSCs was then evaluated against Pt CE DSSCs as a reference with the aim of establishing the enhancement effect of each material in the composite.

2.11 Safety Measures in Nanomaterials

As nanomaterials continue to expand beyond the current use, concerns about their potential effects on human health and environmental systems are emerging (Grassian *et al.,* 2007). Most of the current studies have shown that NPs are on a similar size scale to proteins hence are smaller than organic cells (Jeevanandam *et al.,* 2018). This relative size partly suggests that such particles have a potential adverse impact through biological interaction and permeability (Nel *et al.,* 2006). Although the biocompatibility of AuNPs to human cells (Dobrovolskaia *et al.,* 2009) have been shown to pose low or negligible danger, *in Vivo* studies have traced higher toxicity to the NPs build-up (Chen *et al.,* 2009). Since much is still unknown of their long-term exposure effects, users of nanomaterials must take the highest possible strict precautions (Amoabediny *et al.,* 2009) to eliminate most exposure chances. The most general cause of exposure is the failure to use the proper disposal protocol and the right safety gear when handling nanomaterials. In this regard, wearing protective clothing when handling nanomaterials is necessary. Toxicity studies of most nanomaterials require that NPs be dispersed in aqueous media such as granular sodium chloride. In such media, the NPs tend to form large agglomerates with modified surface charges (Suttiponparnit *et al.,* 2011) which inhibit their toxicity.

CHAPTER THREE

MATERIALS AND METHODS

3.1 Background

This chapter contains a description of the materials and experimental procedures carried out during fabrication and characterization of electrodes and the overall DSSC assembly. It details studies on graphene exfoliation and evaluation of the number of layers based on optical contrast. Procedures for synthesis and characterization of AuNPs are presented. Details on preparation of composite CEs using doctor blade and dip-coating methods, including the final DSSC assembly and characterization are described.

3.2 Preparation and Characterization of Graphene

3.2.1 Materials for Graphene Exfoliation

Highly ordered Pyrolytic graphite, grade SPI-1, #426HP-AB (SPI supplies, USA), shown in Appendix I and double-sided scotch tape were used. Absolute ethanol (99.5 wt-%), hydrochloric acid (HCl) and nitric acid (HNO_3) were all sourced from Sigma-Aldrich Inc. Borosilicate (Pyrex) microscope slides (n = 1.47) were used for sample microscopy. DI water was used for the final cleaning of glassware and microscope slides before drying in an oven at 180 ^{o}C.

3.2.2 Mechanical Exfoliation of Graphene Flakes

The exfoliation and processing of the flakes was performed in steps. Figure 3.1 illustrates the process of obtaining microscopy graphene flakes from HOPG, showing (a) HOPG block, (b) magic scotch tape containing graphene flakes after thinning process, (c) set up for cleaning the flakes after detaching from the tape and (d) flakes transferred onto a microscope slide for microscopy analysis.

For an effective process, the glass slides were first cleaned in aqua-regia (prepared by mixing 3 part concentrated HCl and 1 part concentrated HNO_3), ethanol and DI

water to ensure the microscopy graphene flakes were free from contaminants and easily detached from the tapes. Graphene flakes were prepared from the HOPG by mechanical cleaving procedure reported by Novoselov *et al.,* (2004). The tape with flakes attached was soaked in acetone for 5 min and further for 5 min in ethanol to detach the flakes. These flakes were cleaned in DI water before being transferred to clean microscope slides for drying and analysis.

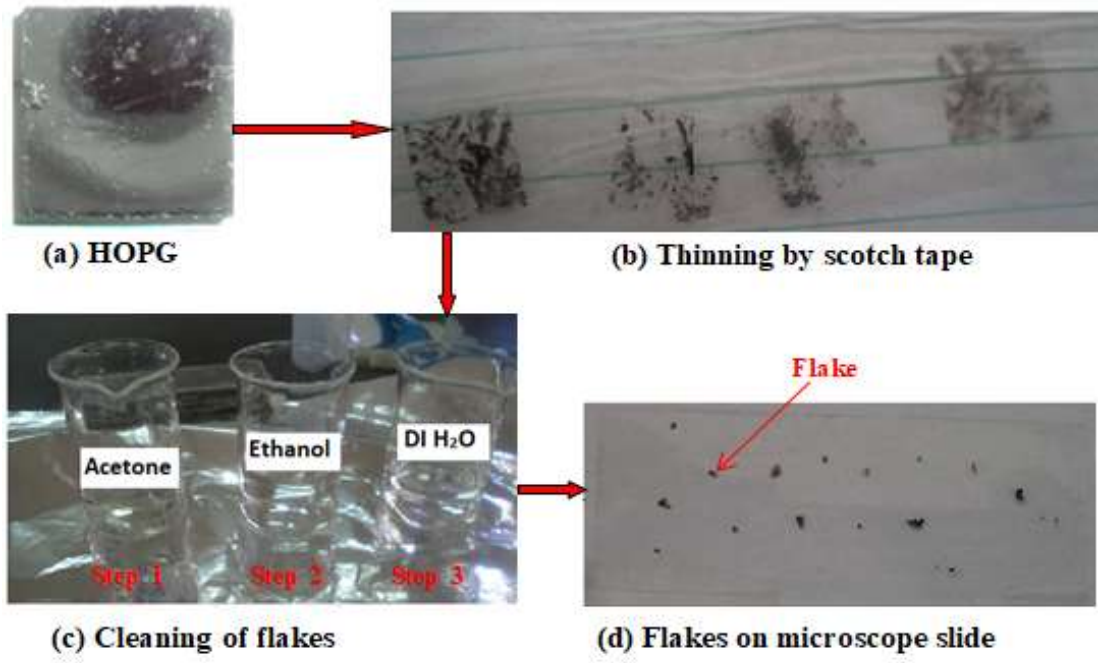

Figure 3.1: Mechanical exfoliation process of obtaining graphene flakes from HOPG (a) HOPG block, (b) thinning of flakes by magic scotch tape, (c) detaching flakes from tape and cleaning, (d) flakes transferred onto a microscope slide.

3.2.3 Characterization of Exfoliated Graphene by Contrast Analysis

Acquisition of optical images of the flakes was made using the *Labomed LX 400* optical microscope model in transmission mode. A charge-coupled device (CCD) camera embedded on the microscope, interfaced to a computer was used to record the incident light (400-800 nm) emitted by a constant power halogen lamp through a 1 mm aperture. Magnified 8-bit color images at resolution 1920×1080 pixels were acquired through *PixelPro* software. The recorded optical images in red, green, and

blue (RGB) forms were analyzed in terms of grayscale values and position (pixels) using *ImageJ 1.48v* software.

3.2.4 Characterization of CVD Graphene on FTO

A CVD SLG module synthesized and transferred on FTO substrate (#Y060515, USA) by poly(methyl methacrylate) (PMMA) technique was used as an electrodes base in this study. Its optical properties were analyzed using a UV-Vis-NIR spectrophotometer (*Spectro* 3700 DUV). Briefly, the transmission and reflection spectra were measured and analyzed between 300 - 2500 nm in 1 nm steps. From the spectrophotometer, optical transmittance, T(%) and reflectance R(%) of bare FTO substrate and of the SLG on FTO (SLG/FTO) were obtained and analyzed within the spectral region from NUV to NIR. For validation, Raman Spectroscopy (Renishaw Ramascope), was used and the quality and thicknesses of the graphene were also evaluated (Castro Neto *et al.,* 2009) to ascertain its transmittance level within the spectral regime for PV applications. Within the region, a comparison of optical conductivity ratio and absorbance (in $\pi\alpha$ units) of SLG was performed.

3.3 Synthesis and Characterization of Colloidal AuNPs

3.3.1 Cleaning of Glassware for AuNPs Synthesis

Cleanliness in all glassware dedicated for the preparation and storage of colloidal gold is essential to avoid any exposure to organic matter hence contamination the samples. The glassware was first washed using hot soapy water, then rinsed in DI water. This was followed by soaking in fresh aqua-regia (Hu *et al.,* 2007) overnight. Final rinsing in the DI water was done followed by oven-drying at 120 ^{o}C for 6 hr. The clean glassware was covered on top with aluminium foil and kept in a clean dry box.

3.3.2 Formulation and Synthesis of Colloidal AuNPs

A solution containing 0.254 mM $HAuCl_4 \cdot 3H_2O$ was prepared by dissolving 0.0500 g of the Hydrogen tetrachloroaurate (III) trihydrate (ACS reagent, ≥ 49.0 Au basis,

$HAuCl_4 \cdot 3H_2O$, MW=393.83 g/mol. Sigma-Aldrich inc.) in 50 mL of the DI H_2O. A solution containing 38.8 mM Na_3Ctr was freshly prepared by dissolving 0.5705 g of trisodium citrate dihydrate tribasic ($Na_3C_6H_5O_7$, MW=294.1 g/mol, 99%. Sigma-Aldrich inc.) to form 50 mL with the DI water. Colloidal AuNPs were prepared through the citrate reduction method (Turkevich, 1985), with a variation in the volume of the Na_3Ctr used. Molar concentration, C (mol/L) of the solutes were based on equation (3.1) (Sigma-Aldrich, 2016);

$$C = \frac{m}{V} \times \frac{1}{MW} \quad \text{.....3.1}$$

where, m is the mass of solute in grams (g) that must be dissolved in total volume V of solution in liters (L) to make the desired molar concentration (C), while MW is the formula weight of the solute in (g/mol.).

Figure 3.2 shows a schematic diagram representing the citrate reduction process carried out during synthesis of colloidal AuNPs. A 50 mL of HAuCl4 solution was heated on a hot plate at ~98 °C with vigorous magnetic stirring until boiling. A volume of 0.85 mL Na3Ctr was introduced into the boiling solution while stirring rapidly. The solution was allowed to boil further for about 6 min attaining a final wine-red color (Pimpang and Choopun, 2011). Heating was stopped and the solution cooled to room temperature while stirring rapidly. The process was repeated by increasing the volume of Na3Ctr by 0.05 mL to obtain six other sets of colloidal AuNPs.

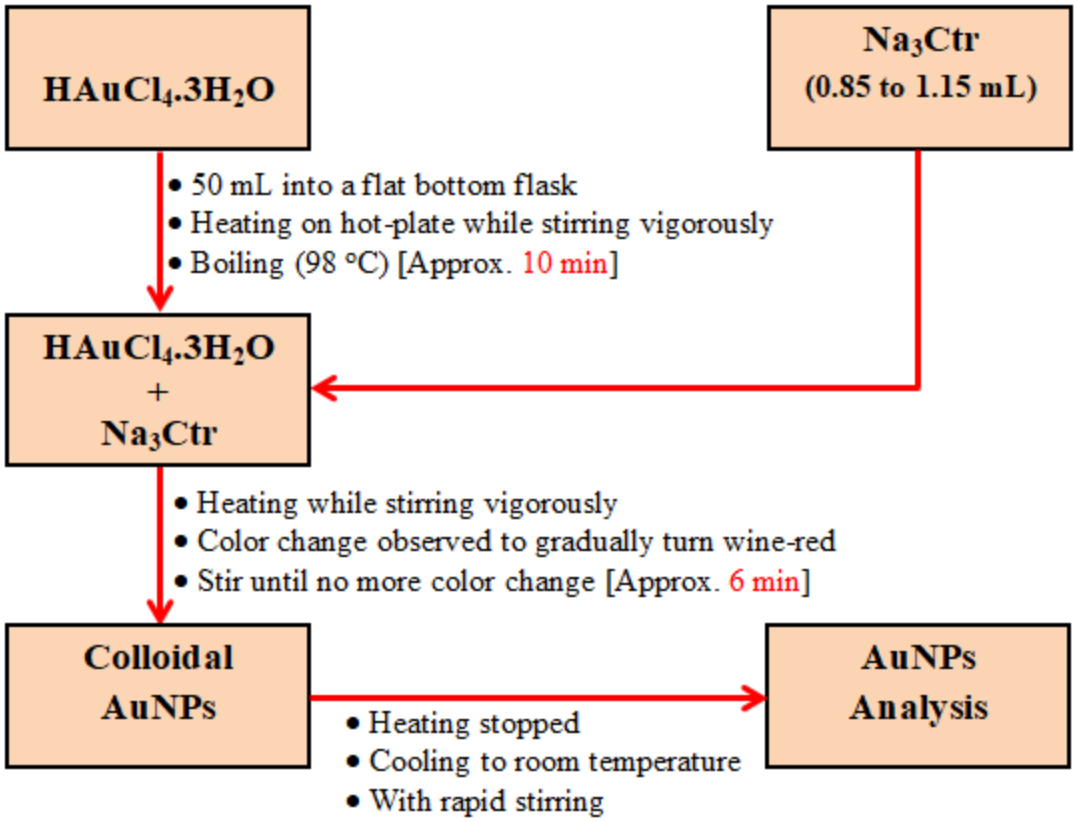

Figure 3.2: A schematic summary of the citrate reduction process for preparing colloidal AuNPs.

3.3.3 Detection of the Presence of AuNPs

The presence of AuNPs in the treated solution was established through observation of progressive color changes during the synthesis process. The final characteristic color plays an essential role in this confirmation. Further, a Tyndall effect test was performed by shining a laser light through AuNPs solution (Yu *et al.*, 2015). Similar test was performed on the reacting solution ($HAuCl_4$ and Na_3Ctr) used in this process to establish if the effect only occurred in the NPs solution.

3.3.4 Determination of AuNPs Sizes using LSPR Method

The NPs size determination was done through UV-Vis spectroscopy, a technique based on absorption of light by molecules within the UV-Vis region. Figure 3.3 shows a schematic representation of the UV-Vis spectrophotometer operational structure.

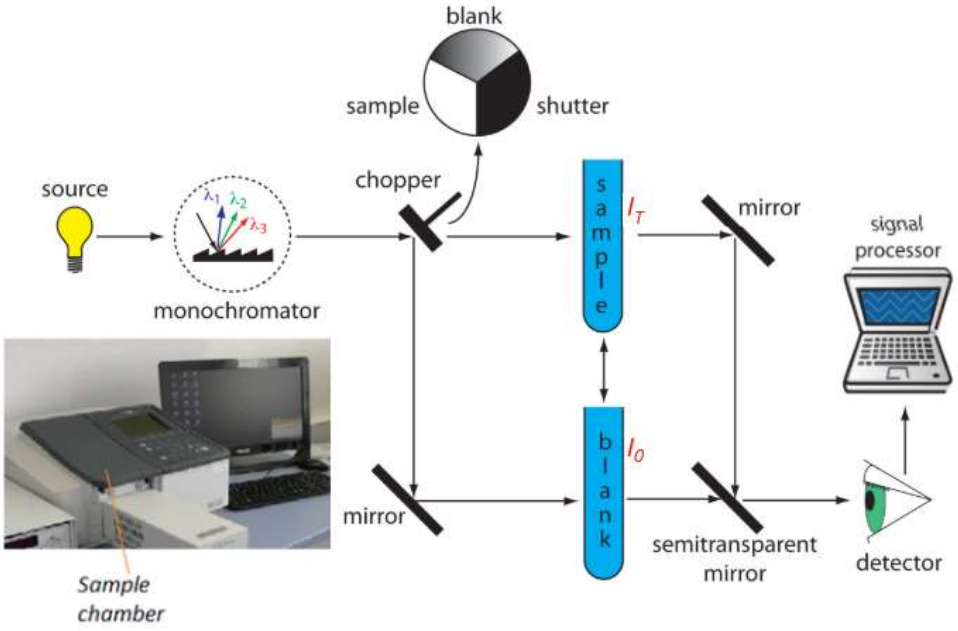

Figure 3.3: A schematic representation of the UV-Vis spectrophotometer operational structure showing signal path for sample detection and processing and (inset) a typical Shimadzu UV-1800 spectrophotometer.

A typical Shimadzu UV-1800 double-beam spectrophotometer used in this study is in the inset. Light beam from the source splits into two pathways, one through the sample cuvette and the other through the set reference cuvette for comparison. The monochromator permits automated recording of spectra. The chopper controls the source beam path, to alternate it between the sample, the blank, and the shutter. The transparent window passes the radiation to the sample while the mirror reflects it to the blank. The signal processor resolves the beam reaching the detector into the transmission of the blank, I_O and the sample, I_T using the chopper rotation speed to keep on adjusting its transmittance. In this study, UV-Vis absorbance spectra of the solutions were recorded in a standard 1 cm × 1 cm × 3.5 cm quartz cuvette at a resolution of 1 nm from 300 to 800 nm. From the UV-Vis absorption spectra, LSPR peak wavelengths and FWHM values generated were used to evaluate the NP sizes, and size distribution.

3.4 Fabrication and Assembly of the Nanocomposites CE-Based DSSCs

3.4.1 Counter Electrodes Preparation and Characterization

3.4.1.1 Substrate Surface Preparation

The FTO glass substrates (~1.5 cm × 2.5 cm, sheet resistance, 12~15 Ohm/sq) and the CVD graphene coated FTO glass substrates (coverage >98%) were received from *MSESupplies* (USA). Colloidal gold NPs (~12 nm) prepared by citrate reduction method according to the procedure previously described in section 2.3. were used. To make a CE, the conductive side of the FTO was identified through resistance continuity testing using a digital multimeter. Two electrolyte filling holes were first drilled through the substrates from the conducting sides at predetermined positions to fit over the cell active area using a 0.8 mm diamond burr (*Eternal tools*). The glass/FTO substrates were cleaned sequentially in three (3) steps of 5 min each. These steps involved soaking in acetone (purity 99.5%), ethanol (purity 99.5%) and the rinsing in DI water to remove any oils, organic residues and dirt, which could be present on the substrate (Katumo *et al.,* 2015). The clean substrate was then dried in a stream of pressurized dry air. On the other hand, the graphene coated glass/FTO substrates were first soaked in ethanol for 5 min then rinsed for another 5 min in DI water before drying under pressurized air.

3.4.1.2 Preparation of CEs Modules

Three test CEs based on Pt, AuNPs, and AuNPs/Pt were fabricated on the FTO/Gr substrate while the reference CE was based on the commonly used Pt-film. Figure 3.4 shows schematic diagrams of the four CE modules namely (a) the FTO/Pt, CE1, (b) FTO/Gr/Pt, CE2, (c) FTO/Gr/AuNPs, CE3 and (d) FTO/Gr/AuNPs/Pt, CE4. For the reference module named CE1, a platinum layer of platisol T/SP pore size, 15-20 nm, (Solaronix, Switzerland) was coated onto the conductive side of the bare glass/FTO substrate through a doctor-blade process.

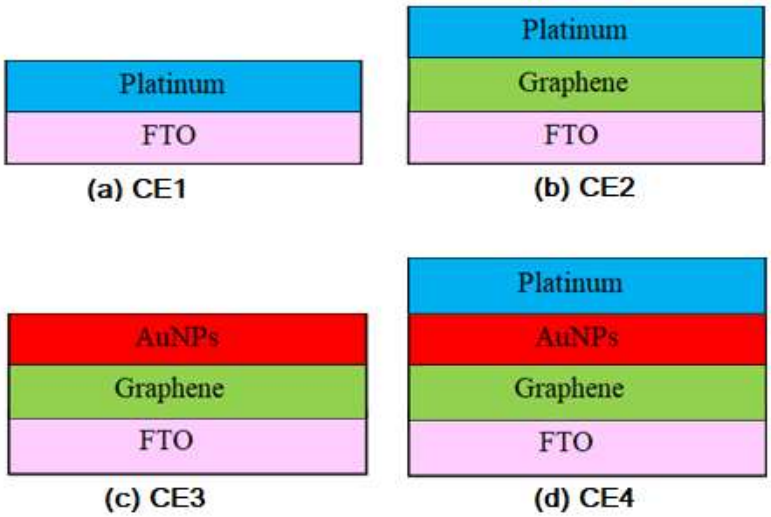

Figure 3.4: A schematic diagrams of the four CE modules prepared, showing (a) FTO/Pt, (b) FTO/Gr/Pt, (c) FTO/Gr/AuNPs and (d) FTO/Gr/AuNPs/Pt.

By using a multimeter, the conductive side of the FTO was identified by testing conductivity continuity. A magic scotch tape was then placed on this conductive side of clean glass/FTO substrate 4 mm from the edge on each side of its length. The platisol, T/SP, was applied manually using the doctor blade technique to generate a thin film deposition. The film thicknesses were controlled through applying uniform pressure in the pasting region. The platinized FTO module was kept in a clean and dry petri dish covered in aluminium foil for 20 min before carefully removing the scotch tape. This was aimed at reducing surface irregularity and getting rid of air bubbles to enhance homogeneity. The module was then heat-treated in a furnace at a rate of 2 ^{o}C /min to 170 ^{o}C followed 5 ^{o}C /min to 400 ^{o}C, then sintered for 30 min. The furnace was switched off and the CE is allowed to cool down gradually to room temperature. To make the second module (CE2), a CVD produced FTO/Gr substrate was platinized as in CE1 to form an FTO/Gr/Pt module.

The third module (CE3), was prepared by dipping the CVD produced FTO/Gr substrate into the colloidal AuNPs at a constant speed with the conductive side facing upwards, and kept in the solution for 3 hours. The aim here was to form a coating of NPs on the film to generate FTO/Gr/AuNPs CE. The sample was then removed gently from the AuNPs solution and carefully wiped off excess solution

from the back-side using cotton swabs. Finally, the surface of the film with NP contacts was dried using a stream of dry air in a clean chamber. The fourth module (CE4) was prepared by platinizing a sample of module CE3 to form an FTO/Gr/AuNPs/Pt CE. The modules were then stored in dark plastic sample boxes.

3.4.1.3 Characterization of Counter Electrode Modules

Characterization of the FTO/Gr modules used in the CEs was carried out using optical microscopy, UV-Vis spectroscopy and Raman spectroscopy to determine the surface characteristics and the graphene defect levels prior to application.

3.4.2 Photoanodes Preparation and Characterization

3.4.2.1 TiO_2 Paste Preparation and Application

The PAs design structure consisted of FTO/Gr/TiO_2 composite. The CVD FTO/Gr modules used as substrates were cleaned, first in acetone (5 min), followed by ethanol (5 min) and then in DI water (5 min) before drying in a stream of dry hot air. A highly dispersed titania nano-particle paste, Ti-nanoxide T/SP (18% wt, 15-20 nm, Solaronix, Switzerland) was used to prepare a mesoporous nanocrystalline TiO_2 film for the PA active layer. In this case, 2.4 g TiO_2 nanopowder (~21 nm, *solaronix*) was dissolved into 40 mL of ethanol (99.5%, Sigma) and continuously stirred for 1 hour using a magnetic stirrer to form a uniform TiO_2 paste. Hand shaking the paste bottle itself was avoided since it could cause air bubble formation preventing good deposition. The conductive side of the FTO/Gr was identified first, as described in section 3.4.1.2. A window measuring 1 x 1 cm^2 was cut from a scotch magic tape (~50-60 µm thick) using a clean sharp blade and mounted on the conductive graphene surface of the FTO/Gr substrate.

A layer of the TiO_2 paste was applied onto the graphene surface of the FTO/Gr substrate module and spread even to form a thin homogeneous film using the doctor-blade coating method (Katumo *et al.,* 2015). Thickness of the TiO_2 film was maintained at approximately 20 μm by use of a constant pressure during doctor blading. The coated module was dried in a covered petri dish at room temperature for

20 min for the film to homogenize and reduce surface irregularity (Sedghi and Miankushki, 2014). It was then annealed in a furnace at an optimized rate of 2 ^{o}C /min (Katumo *et al.,* 2015) from room temperature up to 175 ^{o}C, then at a rate of 10 ^{o}C /min up to 450 ^{o}C. It was then sintered at 450 ^{o}C for 30 min before cooling gradually in the furnace to room temperature (25 ^{o}C). This procedure is noted to promote crystallinity of the TiO_2 by reducing the grain boundary between its NPs to form a tiny porous layer on the FTO substrate with enhanced bonding. In addition, it increases the surface area for efficient dye loading, and reduces charge recombination during transportation of electrons to the CE.

3.4.2.2 Characterization of Photoanode Modules

Characterization of the PA modules was performed based on optical microscopy and UV-Vis spectroscopy. An optical image of the PA TiO_2 surface was captured and a line profile generated in grayscale. From the profile frequency and heights, the state of surface roughness of the PA was established. UV-Vis absorption spectra of the TiO_2 surface before and after N719 dye loading was carried out. The absorbance wavelength range and peak shift in the PA spectra was analyzed for DSSC applications.

3.4.3 Dye Preparation and Application

Ruthenium dye containing 0.5 mM of N719 dye, *cis-diisothiocyanato-bis(2,2'-bipyridyl-4,4'-dicarboxylato) ruthenium(II) bis(tetrabutylammonium)*(*molar mass* 1188.6 g/mol) was prepared by dissolving 200 mg of N719 dye (purchased from Solaronix, Switzerland) in 100 mL of ethanol (99.5 wt-%) in a conical flask. Concentration of the dye was calculated according to the molar equation (3.1).

The flask was covered using aluminium foil and stirred with a magnetic stirrer to ensure all the particles dissolved. Using a measuring cylinder and a micropipette, 236.53 mL of the ethanol was added and stirred to form 0.5 mM of N719 dye solution. The formed solution was then transferred into a dark sample bottle, wrapped in aluminium foil and kept ready for use. The prepared PA was sensitized by gently immersing it in a dye bath solution contained in staining boxes. The

samples were soaked in the dye for 20 - 24 hr then dried in a stream of air. Dye loading was evaluated using UV-Vis spectroscopy.

3.4.4 Composite DSSC Assembly

3.4.4.1 Geometry of the DSSC

Dye sensitized SC modules were fabricated in sandwich geometry. A hot melt sealing film, Dupont surlyn frame (60 μm thick Meltonix 1170-60, Solaronix, Switzerland) was used as a spacer and a thermoplastic sealant between dye coated PA surface and the AuNPs coated side of the CE. Figure 3.5 shows a schematic diagram of a composite DSSC fabrication process, showing the photoanode and counter electrode with the different components in DSSC assembled using the CE4 module. The assembled DSSC structure was fastened using binder clips as shown in the photograph on the top left of Figure 3.5, ready for evaluation.

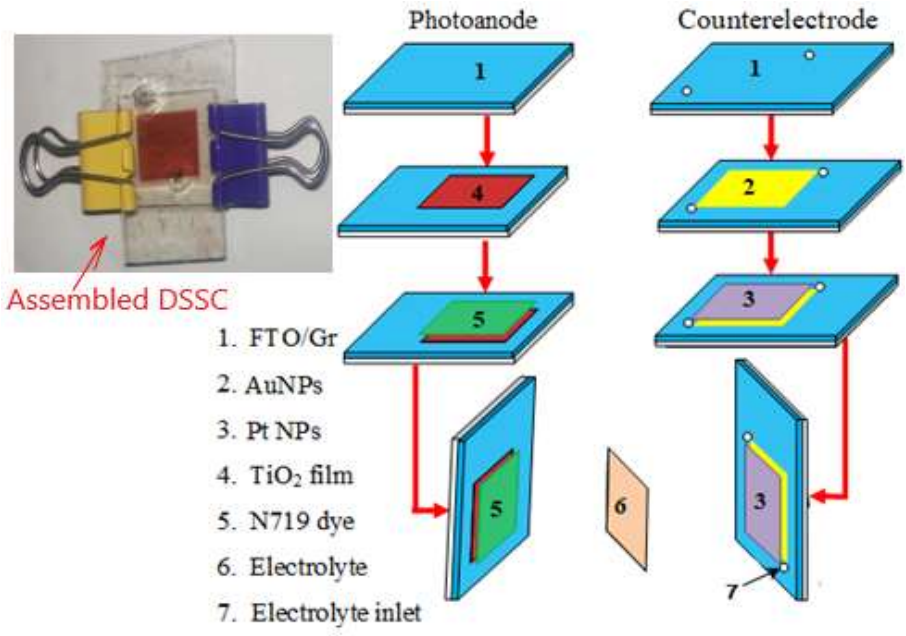

Figure 3.5: A schematic diagram of a composite DSSC fabrication process, showing the different components in the Gr/AuNPs/Pt CE DSSC module. A photograph of the assembled DSSC is shown on top left.

3.4.4.2 Electrolyte Injection and Sealing

A 30 mM iodide/triiodide electrolyte redox couple (Iodolyte HI-30, Solaronix, Switzerland) was injected using a syringe needle into the space between the electrodes through pre-drilled holes on the CE. The holes were then sealed using Amosil 4 sealant (Solaronix) and the cell assembled for testing (Appendix II).

3.4.5 Testing and Evaluation

3.4.5.1 Measurement of the Photovoltaic Parameters

The main parameters used for DSSC characterization were J_{sc}, V_{oc}, *FF* and PCE as discussed in section 2.5. This was based on the standard procedure where the *J*-*V* curve was generated (Sharma *et al.*, 2018). Figure 3.6 shows a schematic illustration of the *J*-*V* data generating setup. A solar simulator based on a 450 W halogen lamp was used and adjusted to provide a spectral output irradiance of 100 mW/cm^2 (AM 1.5 G) illumination at 25 ^{o}C. This was recorded using a solar power meter TM206 (3T0-3-1, Tenmars Taiwan). A single crystal Si photodiode was used to calibrate the incident photon flux to a distance of 0.3 m on the DSSCs. Once the cell was illuminated, voltage sweep was applied and the resulting current measured. The *J* and *V* values were recorded using a digital multimeter.

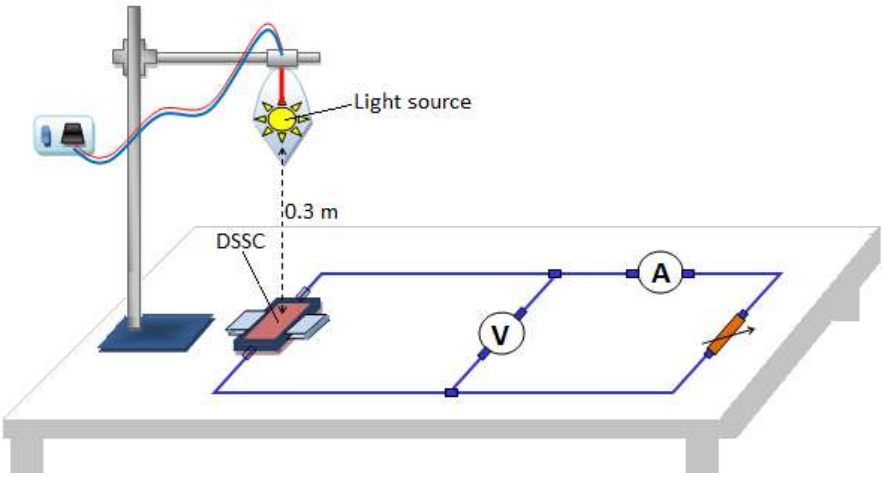

Figure 3.6: A schematic illustration of the *J*-*V* data generating set up.

3.4.5.2 Evaluation of the Composite DSSCs Performance

To evaluate the cell performance, values of J_{pm}, V_{pm}, V_{oc} and J_{sc} were generated from the plotted *J-V* curve. The *FF* (equation 2.15) and η (equation 2.16) of the cells were hence calculated. Graphical software *OriginPro* version 8.5, was used in generating the SCs characteristics.

CHAPTER FOUR

RESULTS AND DISCUSSIONS

4.1 Introduction

This chapter entails a tabular, pictorial and graphical representation of the generated data and the results. Discussion of the results are also given based on data from the three main parts forming the material investigations objectives, namely; graphene, gold NPs and the fabricated DSSC.

4.2 Synthesis and Characterization of AuNPs Sizes

4.2.1 Macroscale Synthesis and Faraday's -Tyndall Effect Test

Based on the citrate reduction of AuNPs, observations were made stepwise during the synthesis process. Figure 4.1 shows the phase change in colloidal AuNPs during the citrate reduction process represented by color change with time starting from (a) pale-yellow gold salt before heating. The color changes recorded during heating at 98 ^{o}C with vigorous magnetic stirring were; (b) colorless solution after 10 min and (c) dark-greyish solution upon addition of Na_3Ctr (12 min). After 14 min of heating, (d) the greyish solution turned purple before attaining the final wine-red color after a total time of approx. 18 min.

The noted color changes were consistent with the macroscale synthesis of AuNPs (Kumar *et al.,* 2007). Gold salt is yellowish in color (Figure 4.1a) and addition of Na_3Ctr under boiling and stirring takes it through the first phase change. In this phase, Au^{3+} reduces into colorless Au^{2+} (Figure 4.1b). Continuous heating takes the solution to supersaturation phase, which is represented by the dark-greyish solution color (Figure 4.1c).

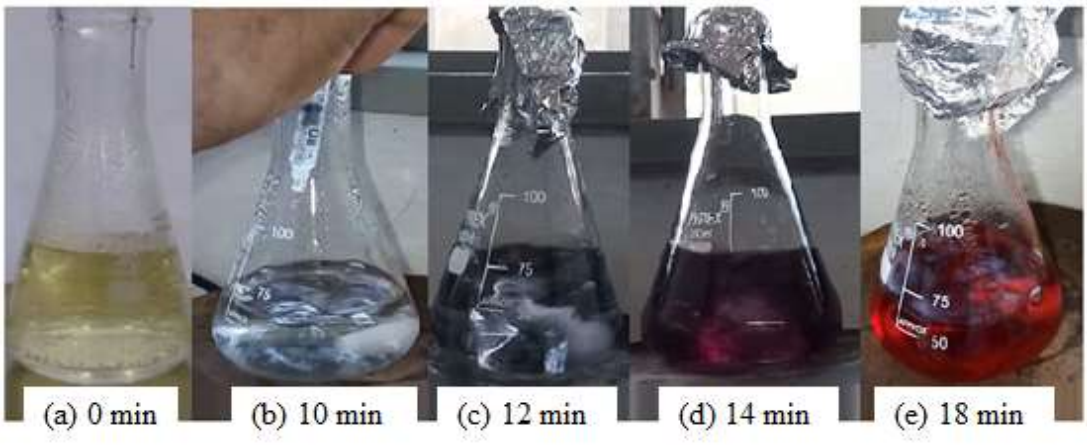

Figure 4.1: Phase change in AuNPs during a citrate reduction process represented by the solution color change with time, given as; (a) pale-yellow gold salt (b) colorless, (c) dark-greyish colored, (d) purple-colored and (e) final wine-red AuNPs.

The third phase in the synthesis involves nucleation, a phase that produces gold nanowires, which are dark bluish/purple in color (Figure 4.1d) which is an intermediary towards AuNPs formation (Wuithschick *et al.*, 2015). The intense wine red (Figure 4.1e) is an indication that, during the growth phase, AuNPs are regenerating. It results from the absorption of some portion of the visible spectrum by the NPs at SPR (Amendola and Meneghetti, 2009; Jain *et al.*, 2006). The different colors observed in AuNPs can therefore be attributed to the fact that smaller particles (<30 nm) absorb light within the blue region while reflecting the red spectrum. Conversely, the larger sized particles absorb wavelength within the red region while reflecting the blue portion of the spectrum hence presenting a bluish/purple color of the AuNPs solution. The kinetics of size changes such as particle agglomeration and aggregation has been studied based on this phenomenon (Hayden *et al.*, 2012).

Figure 4.2 is a photographic representation of Faraday's-Tyndall effect. Figure 4.2(a) shows a reddish beam through the test solution, depicting an occurrence of Tyndall effect in wine red colloidal AuNPs.

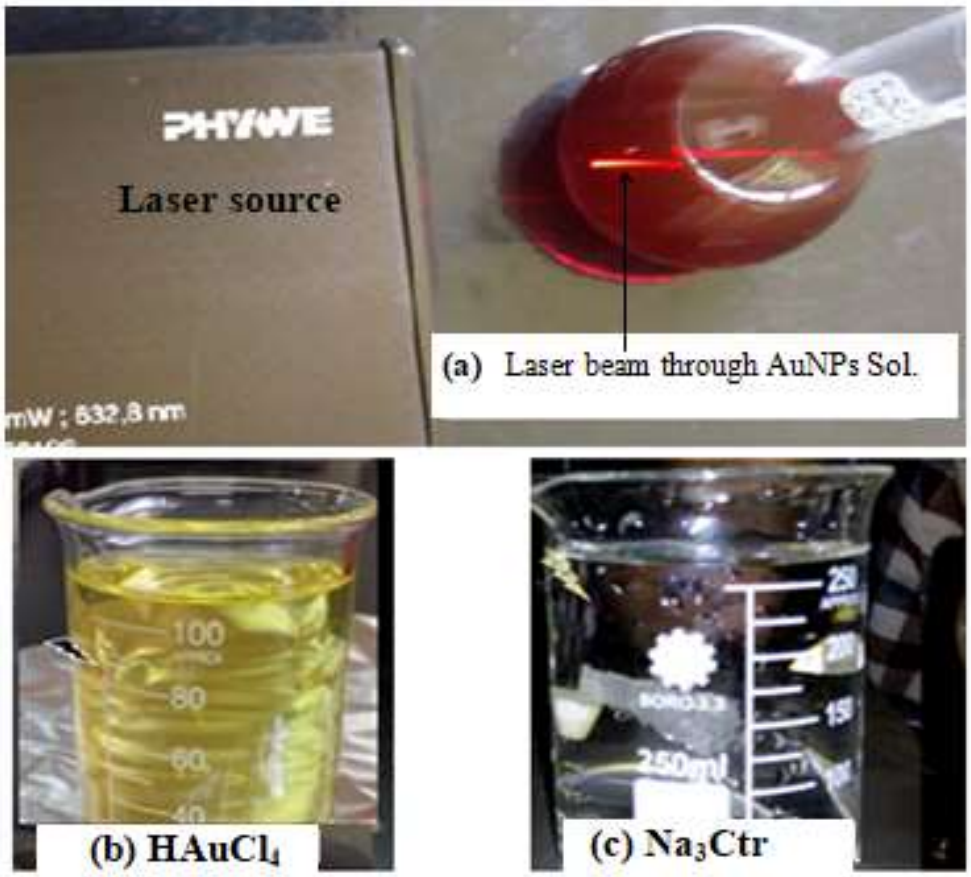

Figure 4.2: A photographic representation of Faraday's-Tyndall effect showing (a) presence of Tyndall effect in wine red colloidal AuNPs and (b, c) absence in $HAuCl_4$ and Na_3Ctr solutions.

Conversely, the reagents used in the AuNPs synthesis, 3.2(b) $HAuCl_4$ salt and 3.2(c) Na_3Ctr solutions show no observable color effect, implying that Tyndall effect is absent. According to Yu *et al.,* (2015), the observed beam path in (a) results from light scattering by the NP present in the solution. This is a characteristic of the Tyndall effect as previously observed (Yu *et al.,* 2015).

4.2.2 UV-Vis Spectroscopy of Colloidal AuNPs

Further, the presence of AuNPs in the final solution was confirmed through the UV-Vis absorbance measurements. Figure 4.3 shows a section of the UV-Vis spectra for colloidal AuNPs synthesized at different amounts of Na_3Ctr. A narrow shift in the LSPR peak wavelength is notable, where a peak of 520 nm was generated when 0.85

and 0.95 mL Na_3Ctr were used, 519 nm when 0.90 mL Na_3Ctr was used while 518 was recorded for 1.00, 1.05, 1.10 and 1.15 mL Na_3Ctr. A full AuNPs spectrum in the Vis region is as shown for 0.85 mL Na_3Ctr in Figure 4.3 (inset). The wavelength at 440 nm was chosen for the purpose of AuNPs size evaluation as discussed in the next section. Generally, absorption peaks occur at ~520 nm representing the LSPR wavelengths. This shows LSPR behavior with the absorption peaks being prominent at ~520 nm, a clear characteristic of AuNPs of size <20 nm (Daniel and Astruc, 2004; Liz-Marzán, 2004). The presence of narrow peaks is an indication of monodispersity in the synthesized NPs.

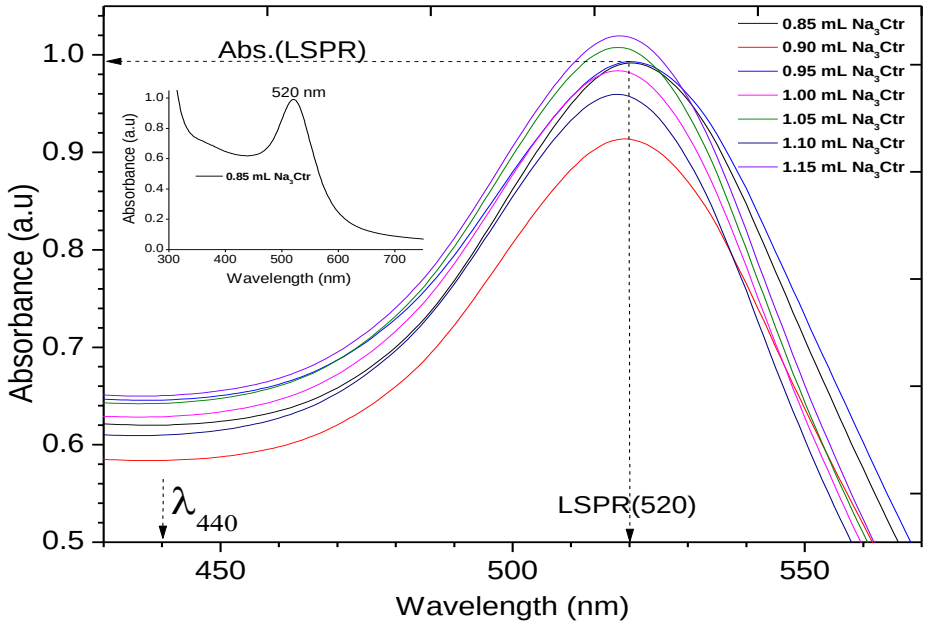

Figure 4.3: UV-Vis spectra generated from colloidal AuNPs synthesized at different amounts of Na_3Ctr. Inset: A full spectra for AuNPs prepared using 0.85 mL Na_3Ctr showing LSPR at 520 nm.

4.2.3 Gold NPs Sizing via LSPR Analysis

To evaluate the size and size distribution of the synthesized AuNPs, LSPR peak wavelengths and FWHM values were extracted from the UV-Vis absorption spectra. Figure 4.4 shows a plot of the variation of LSPR peaks (left axis) with volumes of Na_3Ctr used and the corresponding FWHM (right axis) from UV-Vis spectra of the AuNPs solutions.

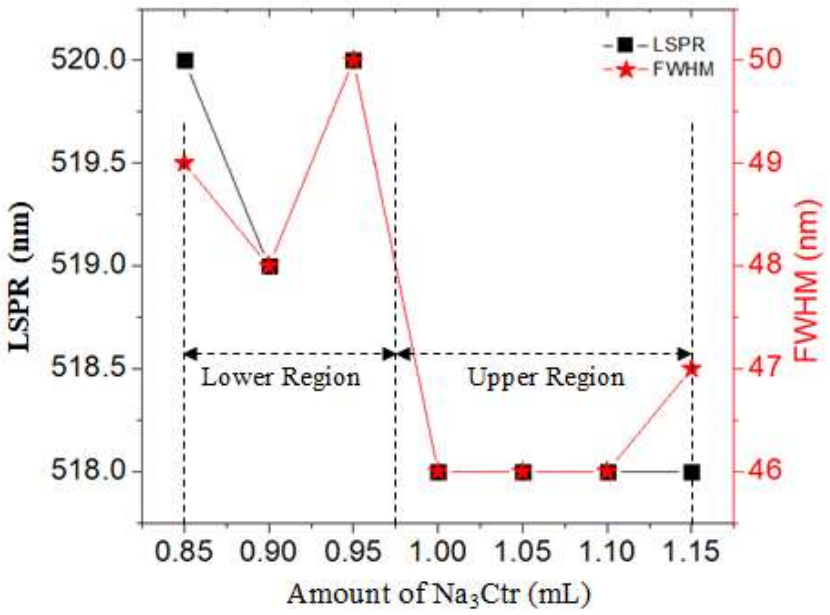

Figure 4.4: Variation of LSPR peaks (left axis) with volumes of Na_3Ctr used and the corresponding FWHM (right axis) from UV-Vis spectra of the AuNPs solutions.

Based on the amount of Na_3Ctr used, two distinct plot regions are observed; the lower region (0.85 - 0.95 mL) and the upper region (1.00 – 1.15 mL). The recorded LSPR peaks wavelengths range between 518 and 520 nm, consistent with the plasmonic AuNPs sizes (Sigma-Aldrich, 2016). In this case, LSPR peaks of 519 and 520 nm occur in the lower region while 518 nm occur in the upper region. Similarly, the larger FWHM values (50 – 48 nm) occur in the lower region, while the smaller FWHM values (47- 46 nm) occur in the upper region of Na_3Ctr used. This shows that the longer LSPR peak wavelengths corresponds to the larger FWHM values at the lower region while the shorter LSPR peak wavelengths corresponds to the smaller FWHM values at the upper region.

According to Pimpang and Choopun, (2011), the LSPR peaks increase with the increase in AuNPs sizes. During synthesis, the faster the AuNPs are capped by the higher amount of Na_3Ctr and the smaller the size of NPs generated (Wang *et al.*, 2018). Therefore, the upper region consisting of shorter LSPR peak wavelengths, represent AuNPs of smaller sizes than the lower region. In addition, FWHM values from UV-Vis absorption spectra have been used to predict size distribution in

colloidal AuNPs (Wang *et al.,* 2018), where the lower FWHM values coincide with narrow size distribution. From these FWHM values, the standard deviations over the lower and upper regions are 1.00 and 0.43 nm respectively. This implies that the narrow range of FWHM values in both regions depict that the AuNPs have a narrow size distribution. However, working within the upper region would generate AuNPs with small sizes and high levels of monodispersity.

The sizes of the AuNPs synthesized were calculated from the LSPR peaks (Haiss *et al.*, 2007), where the recorded sizes were within the 10 - 15 nm range. To evaluate the relation between the amount of citrate used and the size of synthesized AuNPs, the results were plotted and compared to a theoretical prediction from a related study by Kumar (2007). Figure 4.5 shows how sizes of the synthesized AuNPs vary the amount of Na_3Ctr used, based on experimental data from this study (squares) and compared to a theoretical simulation by Kumar (triangles).

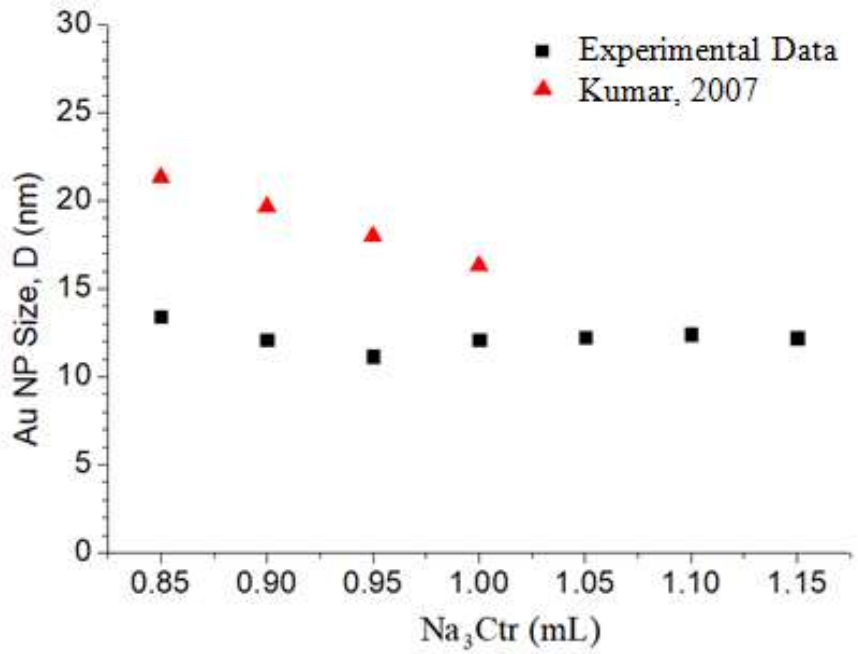

Figure 4.5: Variation of the synthesized AuNPs sizes with the amount of Na_3Ctr used, based on theoretical simulation by Kumar (triangles) and from experimental data in this study (squares).

A general decrease in the size of AuNPs was observed for every additional amount of Na_3Ctr from 0.85 to 0.95 mL. From this range, the synthesized NPs from this work presented smaller sizes, decreasing from 14 to 11 nm compared to the 21 to 18 nm as simulated by Kumar (2007). For citrate volume from 1.00 to 1.15 mL, NPs with an average size of ~12 nm is realized in this work.

As the NPs size decreases, the absorption peak experiences blue shifts. This shift can be described in terms of the d-electron contribution to the dielectric properties (Maier, 2007). By considering the Lorentz–Drude model in bulk materials (gold for this case), the contribution of interband transitions, which involve $s-d$ interactions is described by the Lorentz term function (Equation 2.47). Due to screening by $s-d$ interactions, a reduction in the unscreened bulk resonant frequency value arises (Fan *et al.*, 2014). This reduction occurs at the surface of the NPs during spill out of the s electrons. As a result, the surface-to-bulk ratio of the NPs increases as the size decreases leading a blue shift. This shift has been associated with long-range dipole coupling in the AuNPs (Ghosh and Pal, 2007).

According to Haiss *et al.*, (2007), evaluating the ratios of absorbance at LSPR to absorbance within the wavelength region below 600 nm could give an insight on the quality of the NPs. To evaluate the distribution of the size of NPs within the prepared solutions, the ratios of the absorbance of AuNPs solution at LSPR peak to the absorbance at a short wavelength of 440 nm (A_{SPR}/A_{440}) were generated based on the recorded UV-Vis spectra data. This absorbance ratio presented a linear dependence on the logarithmic particle size range. Figure 4.6 shows the resultant variation of absorbance ratio (A_{SPR}/A_{440}) with natural logarithm of NP size (Ln D) to depict size distribution in the colloidal AuNPs.

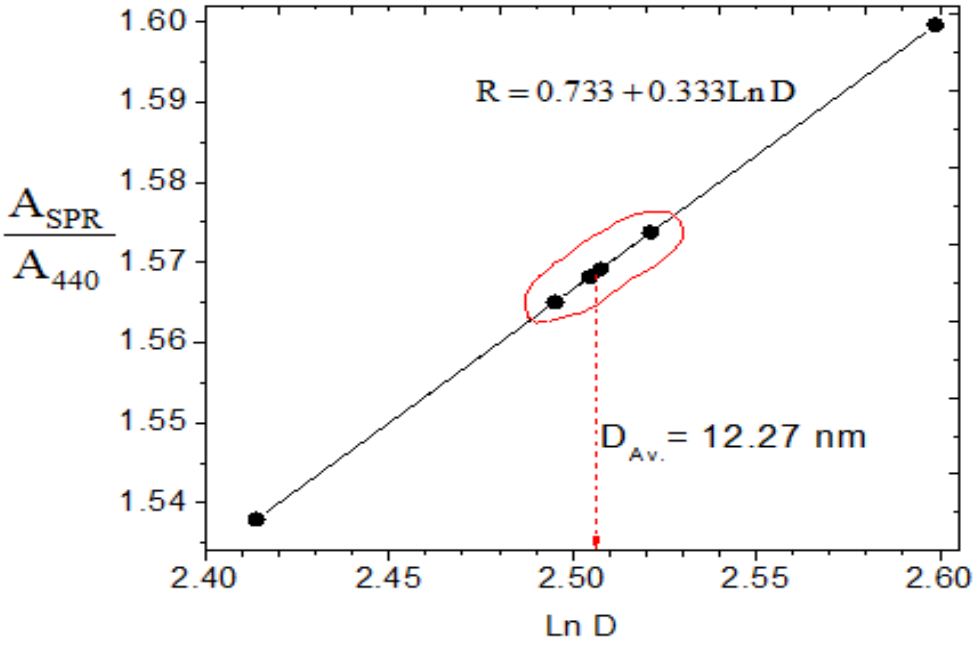

Figure 4.6: Variation of absorbance ratio (ASPR)/(A440) with natural logarithm of NP size (Ln D) to depict size distribution in the colloidal AuNPs.

Most of these NPs had a value close to 2.51 for Ln D, translating to an average size of ~12 nm. The LSPR of most NPs was 518 nm, corresponding to a range of 1.00 - 1.15 mL of Na_3Ctr, consistent with the citrate volumes used, similar to the reported trends (Haiss *et al.*, 2007; Khlebtsov, 2008). In this case, the narrow size distribution is highly concentrated at ~12 nm (equivalent to Ln D value of 2.51).

To validate the relationship between the sizes of NPs and LSPR peak wavelengths in the range 518 - 520 nm, the generated AuNPs sizes from this work were plotted against the corresponding LSPR peaks. Figure 4.7 shows a comparison of different AuNPs sizes (<20 nm) and their corresponding LSPR peaks at 518, 519 and 520 nm as derived from the experimental data from this work and from other studies.

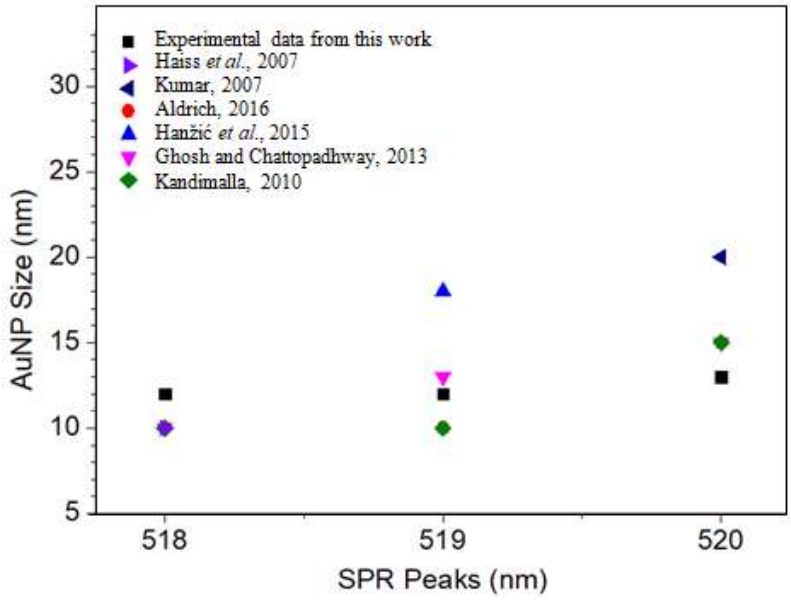

Figure 4.7: A comparison of different AuNPs sizes and their corresponding LSPR peaks as derived from the experimental data and other studies.

It is shown that, AuNPs within the evaluated plasmonic peaks from this study presents a size range 10 - 15 nm, which is in agreement with other studies (Ghosh & Chattopadhyay, 2013; Haiss *et al.*, 2007; Hanžić *et al.*, 2015; Kandimalla, 2010; Kumar, 2007; Sigma-Aldrich, 2016). Additionally, AuNPs of a particular size are capable of exhibiting multiple plasmonic resonances within a narrow size limit (Figure 4.7), with the LSPR values increasing with NPs sizes. For small NPs (<20 nm), the position of LSPR is strongly affected by the decrease in surface electron density as well as the interband transitions (Patungwasa & Hodak, 2008). For AuNPs, this interband transition "pushes" the resonance to around 2.4 eV as compared to bulk gold, which is 10 - 15 eV, corresponding to a wavelength extending from 510 to 530 nm. This high energy band results from the said radiative interband recombination between the *sp*- and *d*-bands (Barman *et al.*, 2015; Beversluis *et al.*, 2003; Xu *et al.*, 2014). Multiple resonance in nanospheres has also been reported (Yao *et al.*, 2018), also attributed to the interband transitions. Based on their large surface-area-to-volume ratio, these small AuNPs find use in nanocomposites for various applications (de Mello Donegá, 2014; Khan *et al.*, 2019).

4.3 Optical Microscopy of Exfoliated Graphene

4.3.1 Detection of Graphene Layers

To evaluate presence of graphene supported on a substrate and identify the number of exfoliated GL, an exfoliated flake optical image was captured, and contrast analysis performed. Figure 4.8 shows an optical microscopy image of a graphene flake revealing clear contrast regions for (a) the substrate, different layers, (b) layer edge and undefined many layers. Based on the way the HOPG snaps during exfoliation, the layers in FLG have well defined steps. However, the step edges are characterized by folds and wrinkles (Zhao, 2018). From the image, the regions of distinct contrast regimes change from bright to dark as the layers increase from the substrate moving towards the bulk of the flake.

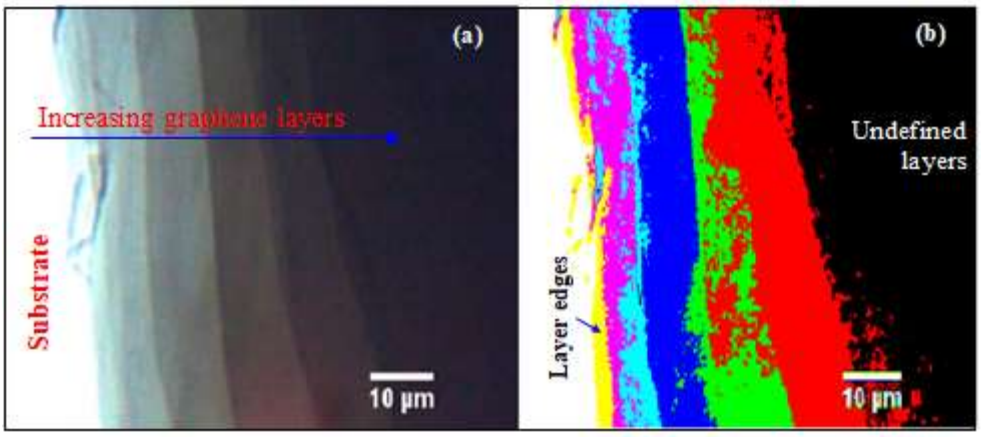

Figure 4.8: An optical microscopy image for a graphene flake showing contrast regions for (a) the substrate, different layers, (b) layer edge and undefined many layers.

To correlate this optical contrast with exfoliated GL, the contrast difference was evaluated using *ImageJ 1.48v* software. The latter is based on grayscale values and position in the red, green, blue (RGB) image contrast channel. Figure 4.9 shows a grayscale level contrast profile for the RGB image channel generated from an optical image of a graphene flake on a glass substrate. An optical image of a graphene flake showing distinct contrast regions along AB for the substrate and four (4) different regions of graphene thickness is given in the inset. From the profile generated along

line AB of the RGB image, a common step-like pattern of gray values is noted. The observed steps depict different GL starting from the substrate, where the gray value is highest followed by an SLG. Each step indicates an additional Gr layer over the SLG (John *et al.*, 2015). As the gray values reduce, the number of layers directly detected through the contrast region steps were limited to four, and denoted by; one layer (1N), two layers (2N), three layers (3N) and four layers (4N) as shown in Figure 4.9. However, using the detected layers, a model to evaluate more layers in FLG ($N < 10$) based on the image contrast was generated.

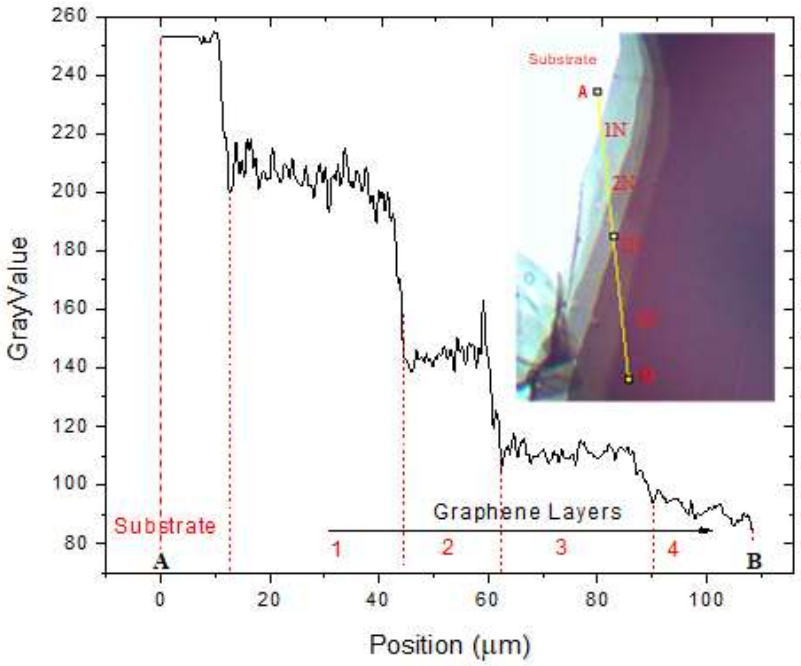

Figure 4.9: Grayscale contrast profile for the RGB channel generated from an optical image of a graphene flake on a glass substrate. Inset: Optical image of a graphene flake showing distinct contrast regions along AB for the substrate and four (4) different regions of graphene thickness.

Along the grayscale, 255 (brightest) represent the least optical absorption region while 0 (darkest) represents the highest absorption region (Wang *et al.*, 2019). Therefore, light absorbance is found to increase along the profile from position A towards B. The bare substrate surface (point A) recorded a gray value of ~255, an indication that its light absorption is almost negligible allowing transmission of most

light. Over the mid-region of the image (Figure 4.9, inset), the observed profile steps describe the different layers of graphene present within the sample flake (John *et al.*, 2015). The stepwise decrease in gray values from ~255, indicates an increased absorption due to increasing GL. Within the region denoted by point B, the sample thickness resulted in a uniform profile with a gray value reducing to ~90 corresponding to the darkest part of the image. This point is taken as having the highest number of GL and beyond no observable contrast based on the sample image since most of the incident light is absorbed within the sample layers.

4.3.2 Evaluation of the Number of Layers in Few-Layer Graphene

Generation of a model for evaluating the number of GL exfoliated was based on the optical contrast in the RGB image. This contrast for each layered graphene over the substrate was determined from the spectra gray values according to equation (2.30), as previously described (Ni *et al.,* 2007). The number of Gr layers was plotted against the layer contrast. Figure 4.10 shows a variation of RGB image contrast level with position along line section AB and corresponding mean contrasts (in bracket). From the image profile the layer mean contrast in gray values along line AB were extracted, plotted, and their mean contrast difference recorded.

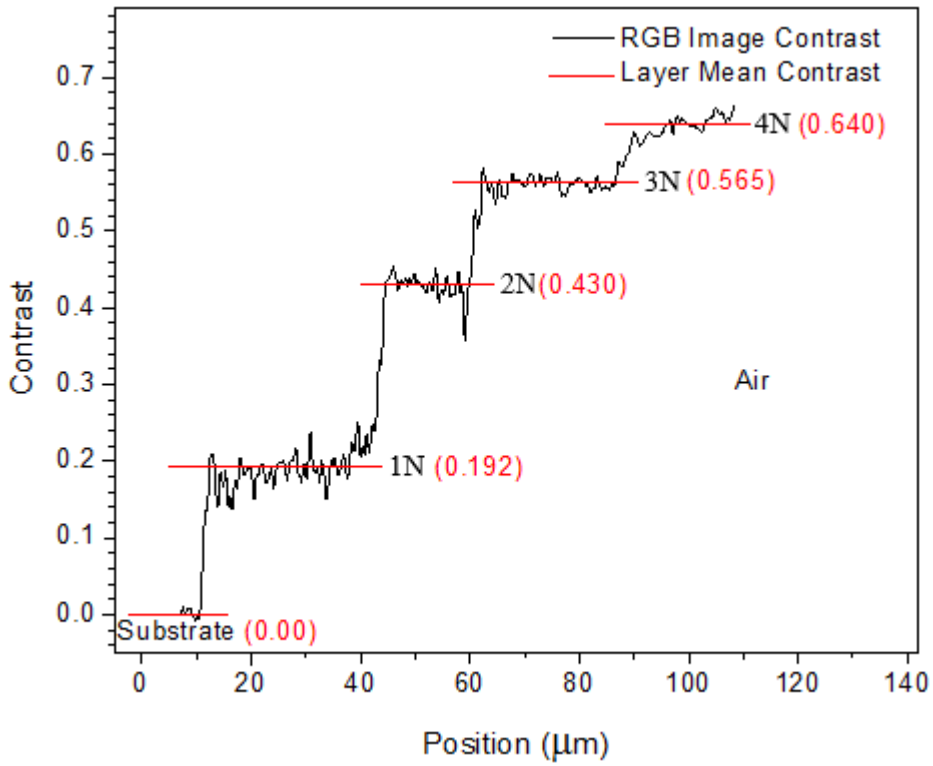

Figure 4.10: Variation of RGB image contrast level with position along the image line section AB, and corresponding mean contrasts (in bracket).

To generate a model for evaluating the number of GL present in an exfoliated flake, the values of N as generated from the RGB image were plotted against the corresponding optical contrast. Figure 4.11 shows the optical contrast variation with the number of graphene layers showing 99.2% correlation based on polynomial fitting and simulated data.

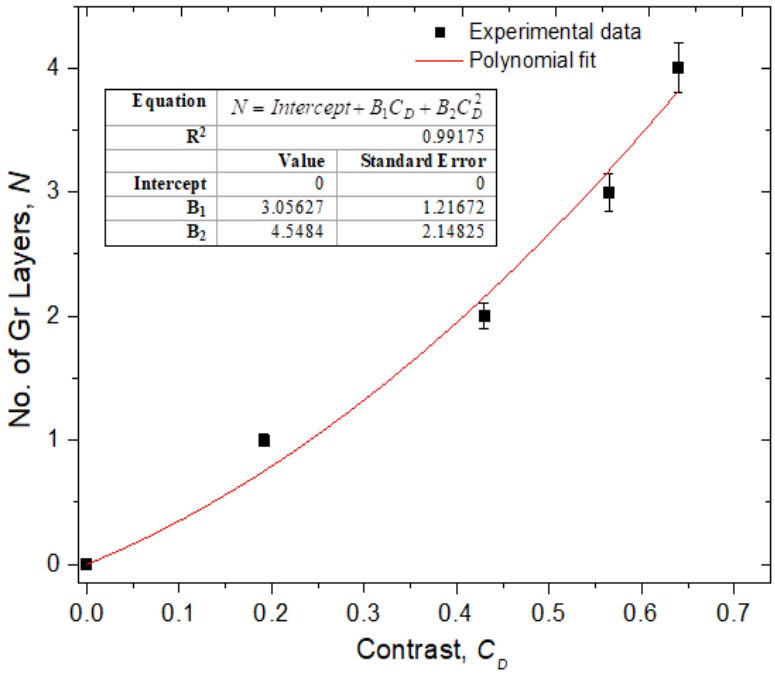

Figure 4.11: Optical contrast variation with the number of Gr layers showing 99.2% correlation based on polynomial fitting.

It is observed that the contrast between each layer and the substrate used increases gradually with the number of layers. A high correlation of 99.2% is established between contrast and the number of Gr layers. This correlation is described by a polynomial fitting given by equation 4.1.

$$N = 3.05627\, C_D + 4.5484\, C_D^2 \quad \text{.....4.1}$$

where C_D is the optical contrast and N is the number of graphene layers detected from the few-layer flakes under optical microscopy.

To establish the limit of this function over the layers, the value of N was evaluated at $C_D = 1$ and found to be 7.6. This indicated that the maximum observable number of GL was ~7. This is the largest number of layers observable from the optical images evaluated. Beyond 7 Gr layers, the contrast generated is beyond the limit of 1.0. Reports indicate that the presence of many GL makes the flake so thick that intensity of reflection as light penetrates through the layers dominates, compared to the light through the substrate resulting in limited contrast (Bing *et al.*, 2018; Ni *et al.*, 2007).

The generated correlation (Equation 4.1) between the number of GL and contrast accurately determines the thickness of FLG up to 7 layers.

4.4 Characterization of CVD Graphene

4.4.1 Analysis of Optical Conductivity in Graphene

The absorbance for FTO/Gr, plotted against energy (Figure 4.12), was found to increase from low energy towards high energy within the NIR (0.50 - 1.66 eV), Visible (1.66 - 3.27 eV), and NUV (3.27 - 4.14 eV) spectral regions.

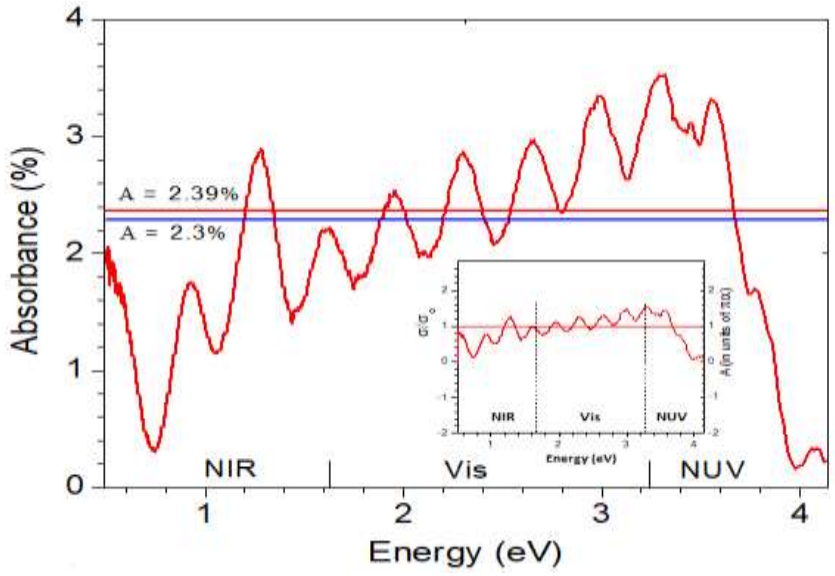

Figure 4.12: Optical absorbance of SLG approximately equal to the theoretical opacity of 2.3% ($\pi\alpha$) in the visible region. (inset): A comparison of optical conductivity ratio, σ/σ_o and absorbance of SLG in units of $\pi\alpha$ showing universality ($\sigma/\sigma_0 = 1$) within the Vis region.

The optical conductivity in terms of the universal optical conductivity, σ/σ_o (Figure 4.12, inset) was found to increase with photon energy, where in the NIR, $\sigma/\sigma_o < 1$ (~0.6), 1.04 in the Vis region and reaching a peak of 1.54 ~3.3 eV (NUV region), before dropping sharply. Since the absorbance $A = 2.3 \approx \pi\alpha$ and taking that $\sigma_1(\omega) = \sigma$, then the ratio σ/σ_0 takes the form;

$$\sigma / \sigma_0 = 1 \quad \text{.....4.2}$$

Therefore, within the visible range, the optical conductivity for CVD grown SLG (σ) approaches the universal optical conductivity which is in agreement with the theoretical expectations where, $\sigma / \sigma_0 \approx 1$ or $\sigma \approx \sigma_0 = 1$ as reported (Kuzmenko *et al.,* 2008). This universality related to the existence of density of states (DOS) as noted by Wang *et al.,* (2010) and is lost beyond the visible energy regime where σ / σ_0 increases rapidly as previously observed (Fei *et al.,* 2008). From the results (Figure 4.12), a decrease in σ / σ_0 to almost zero in NUV region is an indication of non-universality of σ which may be attributed to the intra-band transitions.

4.4.2 Optical Microscopy of CVD Graphene

To explore the surface roughness of the FTO/Gr substrate used in DSSC electrodes, optical microscopy images for the samples were captured under 5X, 20X and 100X magnification and presented as shown in Figure 4.13. The image under 5X magnification (Figure 4.13a) appeared smooth. However, the images at magnifications 20X and 100X of the Gr surface (Figure 4.13b, c) presented more visible but uniform roughness features. Further surface characterization using *ImageJ* provided a better view of the extent of the surface roughness.

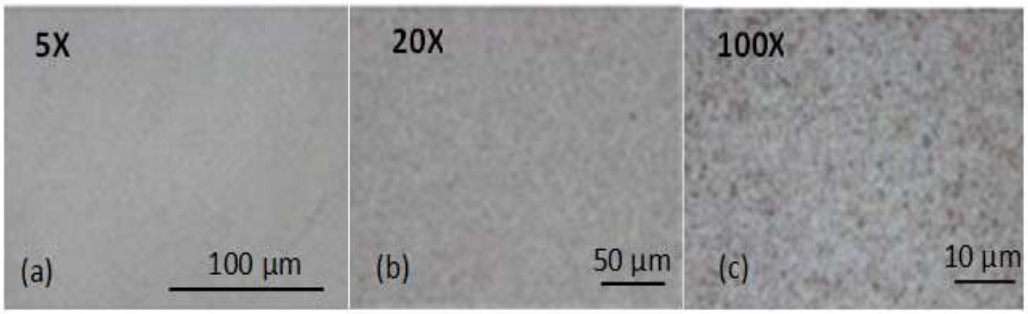

Figure 4.13: Optical images of SLG on FTO substrates (*MSEsupplies*) under 5X, 10X and 100X magnifications showing uniform roughness features.

Figure 4.14 shows the surface profile extracted from the optical image (Figure 4.14: inset) based on the gray value scale of 0 – 255. From the profile, a mean gray value of 160.7876 ± 0.964 and a standard deviation of 14.2352 were recorded.

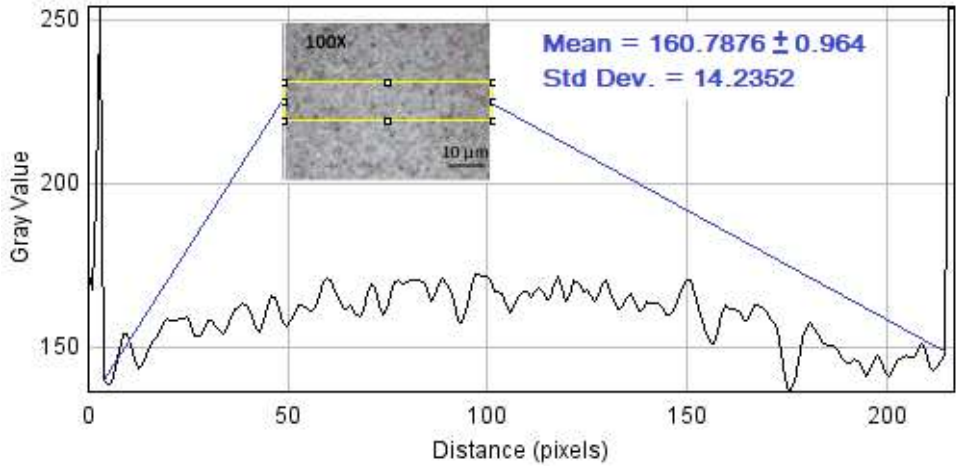

Figure 4.14: A line profile of the FTO/Gr surface gray value level showing low deviation in surface features. Inset: An optical surface image of the module showing the analyzed area.

The low deviation is an indication that surface morphology is not dominated by much pronounced roughness features. This infers that the FTO/Gr surface would provide a credible substrate for TiO_2 or Pt during electrode preparation (Cojocaru *et al.*, 2017) for best cell performance.

4.4.3 Raman Spectroscopy of Graphene Substrate

To evaluate the presence and surface uniformity of the CVD graphene films on the FTO substrate, Raman spectra were generated and optical images recorded and presented as shown in Figure 4.15. The optical image of FTO/Gr revealed uniform surface roughness features over the Gr surface at 100X magnification (Figure 4.15: inset). These features are critical in Pt and AuNPs adherence during electrode fabrication or general surface modification. In PAs, it also facilitates binding of TiO_2 hence providing a large area for dye loading (Jalali *et al.*, 2015).

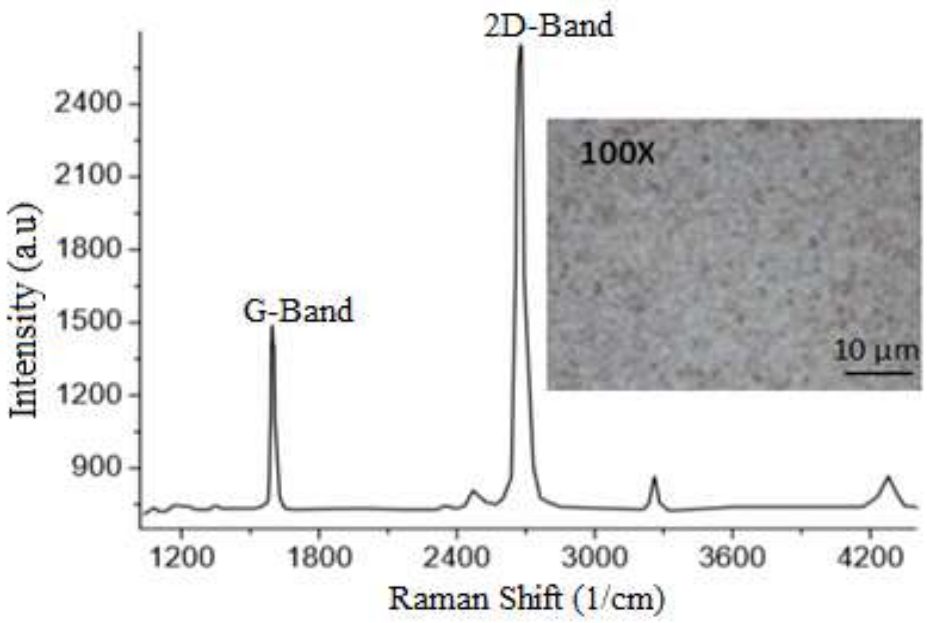

Figure 4.15: A Raman spectrum of SLG on FTO substrate showing the G and 2D band peaks, (inset: An optical microscopy image of the SLG at 100X magnification showing its surface roughness).

The generated Raman spectrum (Figure 4.15), presented two key band peaks at 1596 cm^{-1} for the G band and 2687 cm^{-1} for the 2D band. The 2D peak frequency results from the graphitic materials electronic band structure and represents an overtone of the second order modes of the D band (~1350 cm^{-1}) (Shmavonyan *et al.*, 2013; Wang *et al.*, 2008). The G band on the other hand, arises from the stretching vibration of the graphene carbon atoms (Lalwani *et al.*, 2013). However, the D band, which normally arises from the imperfections in the sp^2 hybridized carbon framework is absent. This implies that largely the carbon-carbon double bond system is intact and hence the graphene is defect free. Table 4.1 presents a summary of the resulting Raman parameters.

Table 4.1: Raman generated parameters for the FTO/Gr substrate module.

V_G (cm^{-1})	$FWHM_G$ (cm^{-1})	V_{2D} (cm^{-1})	$FWHM_{2D}$ (cm^{-1})	I_D/I_G	I_{2D}/I_G
1596	18	2687	38	0.81	1.68

The ratio of the sample characteristic band peaks intensity $I_{2D} / I_G \approx 2$ while the FWHM is 38 cm^{-1} for the 2D band and 18 cm^{-1} for the G band. This is an indication of the presence and uniformity of SLG films over the investigated substrate area (Ferrari *et al.,* 2006; Geim and Novoselov, 2007) and is a confirmation of the uniformity observed in surface microscopy imaging (Figure 4.15 inset). The severely attenuated D band as depicted by a I_D/I_G ratio which is much less than 1 is suggestive of low defects level and good graphitic nature (sp^2 hybridized) of the carbon atoms system in the tested samples (Ferrari *et al.,* 2006; Kibona *et al.,* 2019; Wu *et al.,* 2018).

4.4.4 Optical Transmittance by the Counter Electrode Modules

Upon successful fabrication of the four CEs, evaluation of their transmittance followed. Figure 4.16 shows the optical transmittance spectra of CE1, CE2, CE3, and CE4 compared to the substrate (FTO/Gr) showing optical opacity (T_{550} > 0.7). Within the Vis spectral domain, the FTO/Gr substrate, which has a sheet resistance of ~12 Ω/sq, recorded a transmittance of 0.78 at 550 nm. The FTO/Gr/AuNPs composite CE attained the same transparency (T_{550} = 0.78) as FTO/Gr within the 300–900 nm wavelength range. Moreover, CE2 and CE4 recorded similar transparency (T_{550} = 0.73), while that of CE1 was T_{550} = 0.76).

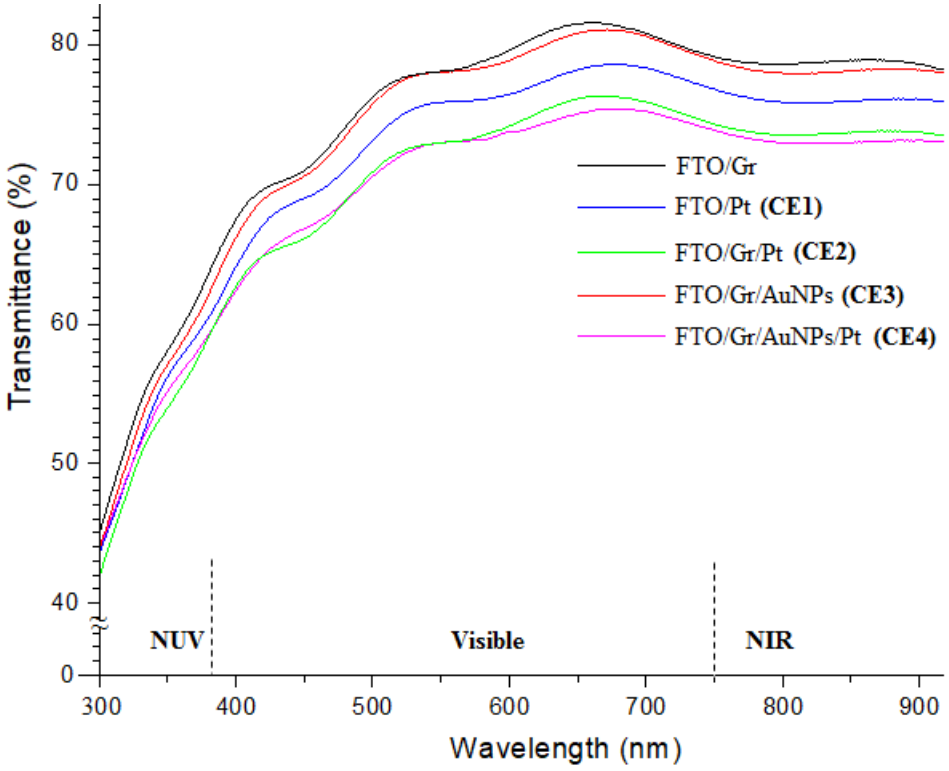

Figure 4.16: Optical transmittance spectra of CE1, CE2, CE3, and CE4 compared to the substrate (FTO/Gr) showing opacity above 70%.

Previous work on composite CEs indicate that any transparency of $T_{550} > 0.7$ is sufficient for a back electrode, where improved cell performance has been reported (Tai and Zhao, 2014). In this work, similar transparency in CE3 and FTO/Gr indicate that addition of AuNPs on the substrate has no observable effect on the opacity of the resulting CE. A similar observation is made between CE2 and CE4. On the other hand, the difference in transmittance between the substrate ($T_{550} > 0.78$) and CE2 ($T_{550} > 0.73$) and between CE3 ($T_{550} > 0.78$) and CE4 ($T_{550} > 0.73$) could be attributed to the added Pt film. The trasmittance of Pt on FTO has been shown to be over 70% at 550 nm (Ren *et al*., 2014). The lower transmittance in CE1 ($T_{550} > 0.76$) than in the substrate similarly results from the contribution of the Pt, and the absence of Gr, although it has a low effect due to its high transparency (97.8%) (Lee et al., 2013).

4.5 Surface Roughness of the PA and Absorbance of N719 Dye

For effective surface modification of the substrates, it is important to understand the surface features that affect the charge transfer in a PA. To evaluate the surface roughness of the PA, an optical image of treated TiO_2 film (Figure 4.17, inset) as prepared on the FTO/Gr substrate was analyzed using *ImageJ* as shown in Figure 4.17.

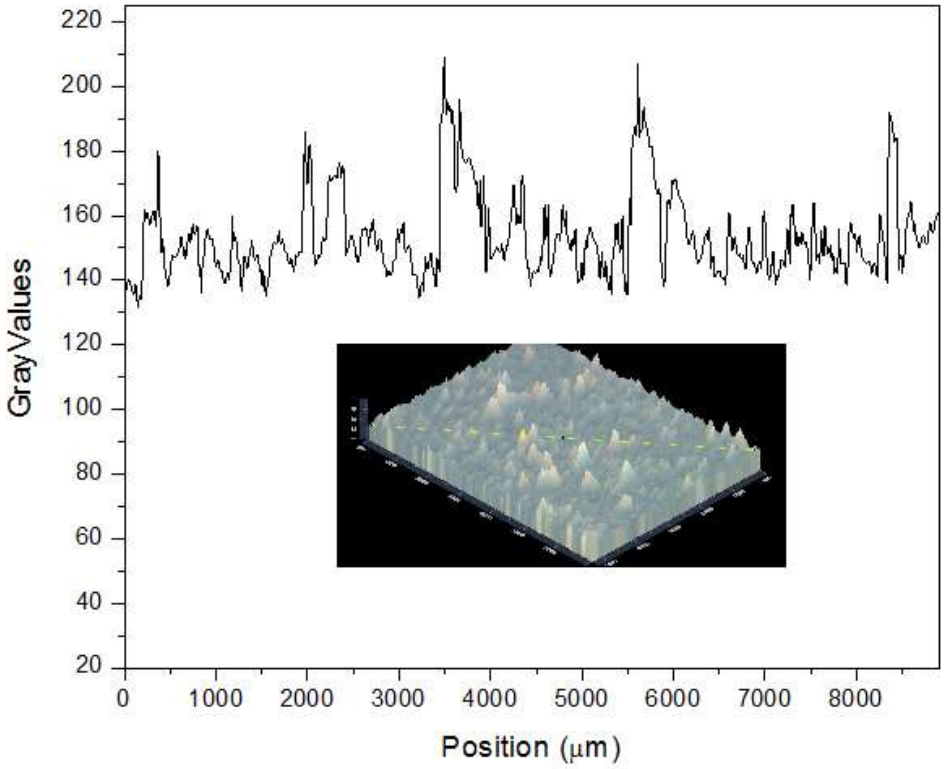

Figure 4.17: A line profile of the TiO_2 surface prepared on FTO/Gr showing peaks and frequency variation on the grayscale coinciding with the roughness features observed on the TiO_2 surface image (inset) along a line section.

The resulting module was found to possess surface roughness features. These features result from enhanced mobility of molecules during annealing which makes the film more homogeneous. According to Cojocaru *et al.,* (2017), the substrate surface uniformity improves interfacial contact of TiO_2 with the dye to enhance dye loading, hence improving electron transfer efficiencies by the PA.

Figure 4.18 shows the absorption spectrum of the N719 dye loaded on the TiO_2. With ethanol solvent, the dye presents two key peaks; a wide narrow peak at 550 nm, within the visible region. This absorbance spectrum is in agreement with earlier observations (Muhammed *et al.*, 2018). This means that the dye needs to be irradiated with light energy of wavelength 550 nm to excite a single one electron from the sample particle.

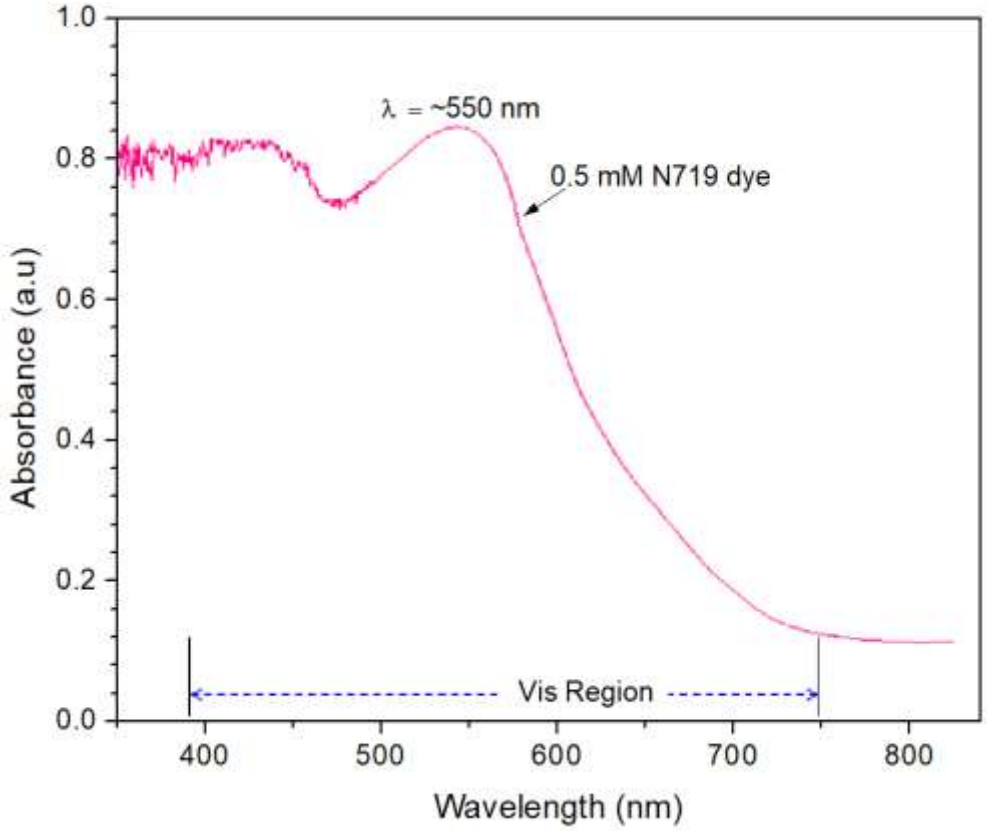

Figure 4.18: Absorbance spectra of the N719 ruthenium dye showing key peak at 550 nm.

To establish the effectiveness of the N719 dye loading onto the mesoporous TiO_2 film, absorption spectrum of the PA before and after dye loading was plotted and evaluated. Figure 4.19 shows an absorbance spectra of the prepared photoanode, (a) without dye and (b) with N719 dye.

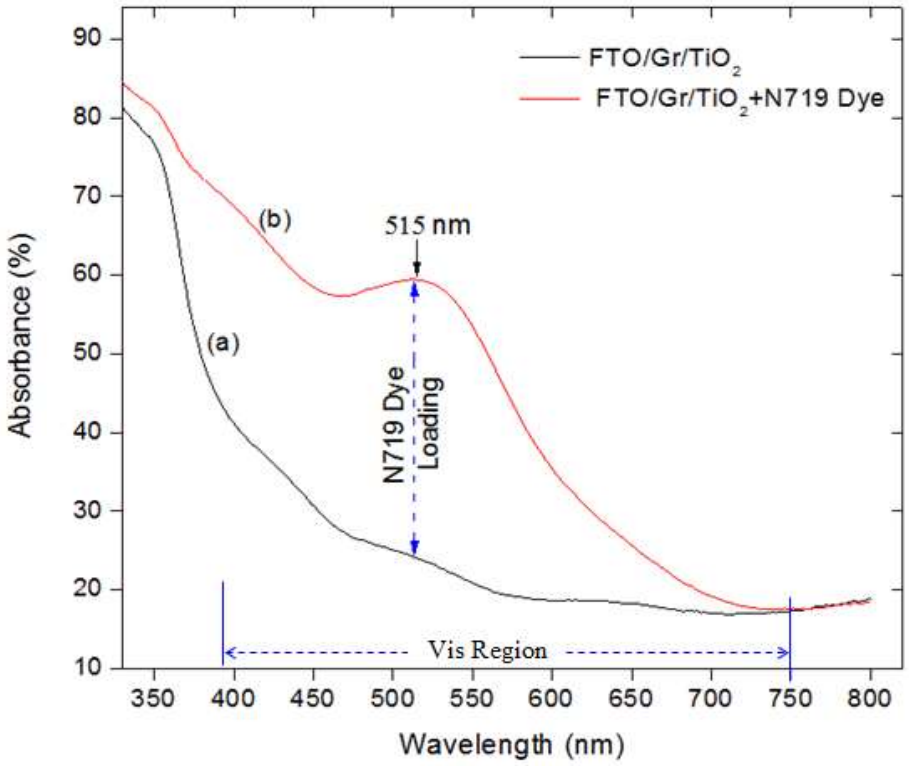

Figure 4.19: Absorbance spectra of the PA (a) without dye and (b) with the N719 dye. The absorbance extends within the visible region and the maximum dye loading into the FTO/Gr/TiO_2 PA module occurring at ~515 nm.

The absorbance is found to extend over the whole visible region. Dye loading onto the FTO/Gr/TiO_2 photoanode module is best at ~515 nm. Within the visible regime, the optical absorption by the adsorbed N719 dye and the various PA components is highly pronounced compared to other regions of the spectra. While the peak absorbance of the dye is at 550 nm consistent with other reports (Wang *et al.*, 2014), the least absorbance is observed within the NIR. This provides a clear evident of the worthiness and capability of such dye loaded PA in light harvesting.

It is clear that the FTO/Gr/TiO_2 composite photoelectrode presents remarkable absorption nearly within the entire visible region upon dye loading. The observed high absorbance by FTO/Gr/TiO_2 PA partly results from the excellent light absorption effect of the N719 ruthenium dye (Shih *et al.,* 2012). Additionally, the PA design with graphene provides the TiO_2 thin film micro-cavities necessary for dye retention over providing an optical path through which multiple scattering of light occurs (Liu *et al.,* 2012). Moreover, Gr forming the FTO/TiO_2 interface within the PA suppresses carrier recombination increasing carrier lifetime and hence photocurrent density (Eshaghi & Aghaei, 2015).

4.6 Performance of the Composite DSSCs

4.6.1 *J-V* Characteristics of the Composite DSSCs

To investigate the performance of the DSSCs assembled using the composite CEs, their *J-V* characteristics were first plotted. Figure 4.20 shows the resulting *J-V* characteristics of DSSCs assembled using CE1 (Pt), CE2 (Gr/Pt), CE3 (Gr/AuNPs) and CE4 (Gr/AuNPs/Pt) measured at 100mW/cm^2 (AM 1.5) illumination. The J_{sc} was found to increase progressively for the DSSCs based on CE1, CE2 and CE4, which contains Pt. The Pt-free DSSC, based on CE3 recorded a J_{sc} value higher than CE2 and the reference CE1, although slightly lower than in CE4. The recorded V_{oc} values for the four CE DSSCs were closely equal at ~0.7 V.

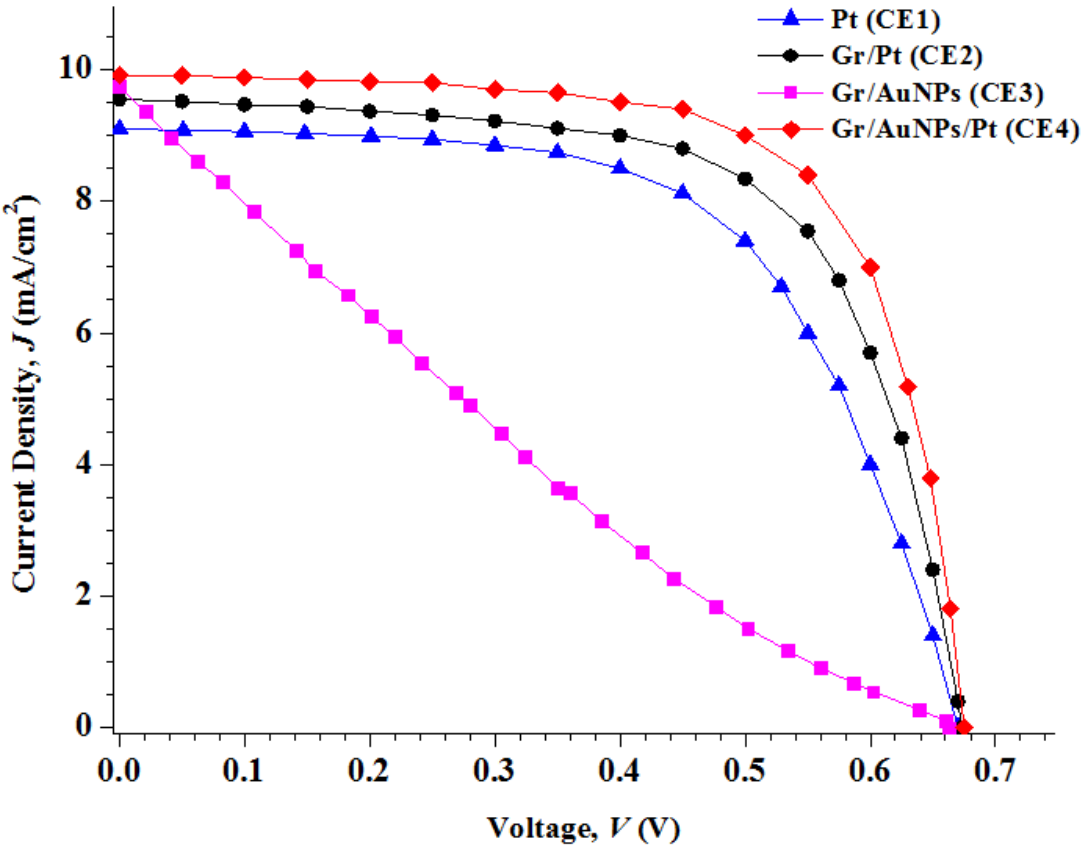

Figure 4.20: *J-V* characteristics of DSSCs assembled using CE1, CE2, CE3 and CE4 measured at 100 mW/cm^2 (AM 1.5) illumination.

4.6.2 DSSC Photovoltaic Parameters

From the *J-V* characteristics (Figure 4.21), the PV parameters were generated, and tabulated. A summary of PV parameters for the DSSCs assembled using CE1, CE2, CE3 and CE4 is provided in Table 4.2, with corresponding percentage change in PCE (ΔPCE) in CE2, CE3 and CE4 based DSSCs with reference to CE1 are indicated.

Table 4.2: A summary of PV parameters as extracted from the DSSCs assembled using CE1, CE2, CE3 and CE4.

Cell Code	CEs	J_{sc} (mA/cm^2)	V_{oc} (V)	*FF*	PCE (%)	ΔPCE (%)
CE1	FTO/Pt	9.10	0.670	0.607	3.700	0
CE2	FTO/Gr/Pt	9.55	0.673	0.653	4.196	13.41
CE3	FTO/Gr/AuNPs	9.75	0.663	0.213	1.375	-62.84
CE4	FTO/Gr/AuNPs/Pt	9.92	0.675	0.690	4.620	24.86

4.7 Evaluation of the Photovoltaic Performance Enhancement

To evaluate the performance of the assembled DSSC modules, the resulting PV parameters (Table 4.2) were evaluated. Figure 4.21 provides a graphical representation of the summarized PV parameters showing the behavior of (a) J_{sc}, (b) V_{oc}, (c) *FF* and (d) PCE values for the four DSSCs based on CE1, CE2, CE3 and CE4. It is observed that, all the test cells recorded an increase in J_{sc} from CE1 (9.10 mA/cm^2), CE2 (9.55 mA/cm^2), CE3 (9.75 mA/cm^2) and CE4 (9.92 mA/cm^2) (Figure 4.21a). The V_{oc} values for CE1 (0.67 V), CE2 (0.67 V), CE3 (0.66 V) and CE4 (0.68 V) varied slightly, fairly approximating to 0.7 V (Figure 4.21b). Additionally, the *FF* for CE1, CE2, CE3 and CE4 were 0.61, 0.65, 0.21 and 0.69 respectively (Figure 4.21c). This notable change in J_{sc} translated well to the resulting PCE values for CE1 (3.7%), CE2 (4.2%), CE3 (1.4%) and CE4 (4.6%) (Figure 4.21d). However, the lower V_{oc} (0.66 V) and *FF* (0.21) in CE3 compared to the reference V_{oc} (0.67 V) and *FF* (0.61) resulted in its minimal PCE, which is 62.8% decrease. This dismal performance in CE3 could be attributed to the absence of Pt, which is essential due its high catalytic properties towards I_3^- reduction (Hoshi *et al.*, 2014).

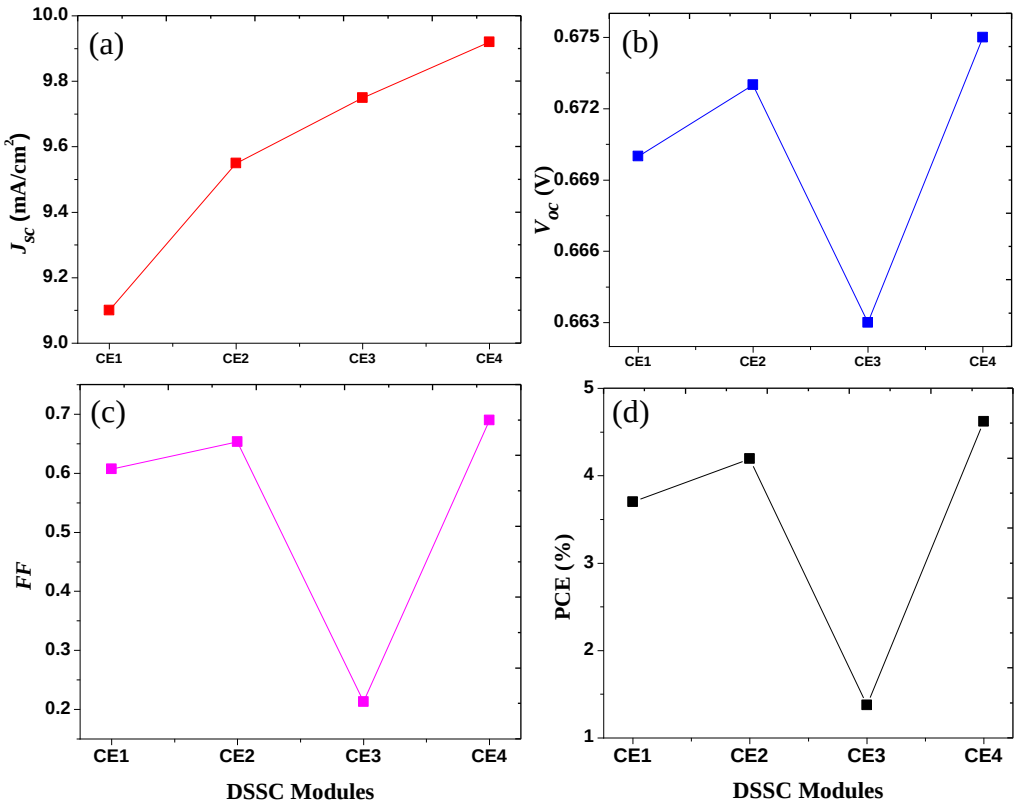

Figure 4.21: A graphical representation of the recorded PV parameters showing variation in (a) J_{sc}, (b) V_{oc}, (c) *FF* and (d) PCE values for the four DSSCs based on CE1, CE2, CE3 and CE4.

Considering the Pt based DSSCs (CE1, CE2 and CE4), the PCE is also found to increasingly correlate with the increasing J_{sc}, V_{oc} and *FF*. The performance of CE1 based cells matched well with previous study by Katumo *et al.*, (2015). Figure 4.22 shows a comparative analysis of the PV parameters enhancement for the Pt - based nanocomposite DSSC modules (CE2 and CE4) compared to the reference, CE1. The enhancement in PV parameters of CE1 based DSSC is 0%. A minimal enhancement in V_{oc} at 0.5% (CE2) and 0.8% (CE4) is observed. An enhancement of 5.0% (CE2) and 9.0% (CE4) in J_{sc}, with 7.6% (CE2) and 13.7% (CE4) in *FF* resulted in a remarkable PCE enhancement for CE2 (13.4%) and best in CE4 (24.9%) compared to CE1.

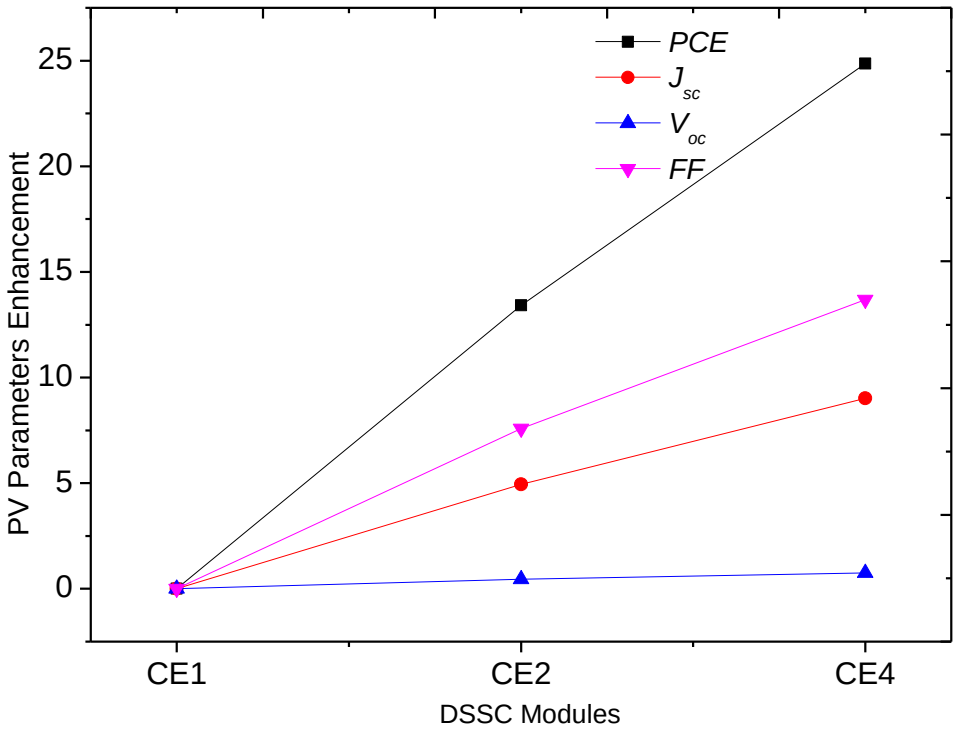

Figure 4.22: A comparative analysis of the PV parameter enhancement for the Pt - based nanocomposite DSSC modules (CE2 and CE4) compared to the reference, CE1.

The recorded progressive enhancement in CE2 and CE4 is attributed to the addition of the Gr and Gr/AuNPs nanomaterials to interface FTO-Pt CE in CE2 and CE4 respectively (Yang *et al.,* 2015). Comparing the observed PCE enhancements, the contributions of the various component materials were 13.4% from Gr/Pt in CE2 and 24.9% from Gr/AuNPs/Pt in CE4 composite. Further, a comparison of CE2 and CE4 reveals that AuNPs contributed 10.1%, which in addition to Gr contribution (13.4%) results in 23.5% efficiency enhancement. This is much closer to their synergistic effect of 24.9% in the composite. Considering CE2 and CE4, the 2-D graphene matrix structure forming the FTO-Pt CE interface layer offers a high charge conductivity effect (Cheng *et al.,* 2013; Lee *et al.,* 2013) on the DSSCs. Deposits of Pt NPs on Gr as prepared in CE2 and CE4 increases the Faradaic current densities for the I^-/I_3^- reaction within the module (Hoshi *et al.,* 2014). This improves the porosity of contact films hence enhancing the catalytic activity and carrier lifetime

thus reducing the charge recombination within the electrode (Cheng *et al.,* 2013; Gong *et al.,* 2011; Yue *et al.,* 2013).

The presence of AuNPs over the Gr surface in CE2 or as a Gr/Pt interface in CE4 offers strong resonance energy transfer providing light concentration effect (Atwater & Polman, 2010) due to their LSPR property to improve the cell efficiency (Hong *et al.,* 2008; Wang *et al.,* 2010). According to Mcleod *et al.,* (2015), the optical properties of the Gr/Au composites are greatly influenced by the NPs density, positioning and antiparticle spacing. Previous reports have indicated that there exists thermal coupling mediated by the acoustic phonon interactions across the Gr/Au interface (Sundaram *et al.,* 2011). For DSSCs, these cause a temperature rise within the CE structure hence impairing its stability and performance resulting in a low J_{sc} value (Sundaram *et al.,* 2011). Although this assertion is not evaluated in this work, together with the absence of an electron transfer mediator or linker for stabilizing the anchoring of the Au contacts on the CVD Gr surface, it is also pointed out as playing a negative role in achieving higher photocurrent (Bianco *et al.,* 2016).

In this work, the overall best performance was achieved with the Gr/AuNPs/Pt (CE4) composite DSSC, where a PCE of 4.6% was recorded, representing a 24.86% enhancement. An enhanced coupling existing between these component layers making the CE reduces the series resistances of electrodes, electrolyte and contacts (Cheng *et al.,* 2013). Reports indicate that there exists large charge transfer resistance within the electrolyte interface resulting from the poor diffusion by the redox couple within graphene pores (Gong *et al.,* 2011; Yen *et al.,* 2011). However, incorporation of AuNPs as a bridge to TiO_2 close to the electrolyte promotes this charge transfer due to their light concentration effect arising from LSPR (Atwater & Polman, 2010). Moreover, inclusion of Gr at the FTO/TiO_2 interface of the PAs creates a larger area of contact for adherence of TiO_2 NPs on FTO, thus enhancing transfer of the photo-induced electrons (Guo *et al.,* 2015). Furthermore, the direct contact between the redox/electrolyte and the FTO surface is then blocked resulting in minimal rate of electron-hole recombination in the TiO_2 material layer (Kongkanand *et al.,* 2007).

The charge transfer rates and mechanisms over the electrodes interfaces under different modifications have been widely studied (Hauch & Georg, 2001; Ponken *et al.,* 2017; Yang *et al.,* 2015). For the CEs, charge transfer at the FTO/Pt interface has been effective with reported cell efficiencies of 3-5% (Smestad *et al.,* 1994) and 5.9% (Ponken *et al.,* 2017). Moreover, at the CE interface with the electrolyte (FTO/Pt/Electrolyte), it greatly influences the J_{sc} and the general cell efficiency (Dagher *et al.,* 2014; Hauch & Georg, 2001; Kakiage *et al.,* 2015; Kusama & Sayama, 2015) due to the said charge recombination. Similarly, for the PAs, effective charge interaction and transport within the FTO/TiO_2 interface has also been realized and attributed to the crystalline nature of the TiO_2 (Gong *et al.,* 2011; Sun *et al.,* 2010; Tang *et al.,* 2010; Yang *et al.,* 2010). Modification of the TiO_2/dye/electrolyte interfaces by varying the TiO_2 thickness and using liquid-based electrolyte has been able to enhance the efficiencies (Cho *et al.,* 2016). The modified electrodes DSSCs in this paper report an efficiency enhancement of 24.9%. Although these DSSC designs would provide high competition between charge regeneration and recombination, their resulting efficiencies are still low.

4.8 Contribution of the Composite CE to Overall Performance of DSSC

To visualize how the overall DSSC design would facilitate photoelectrons to flow from dye molecules to the outer circuit through the CB of graphene/TiO_2/FTO interfaces, first consider the work functions (WF) of these composite materials making the PA. Figure 4.23 shows a schematic energy level and charge recombination diagram for the Gr/AuNPs/Pt composite DSSC. The CB for FTO, graphene, TiO_2, AuNPs, Pt and the HOMO and LUMO levels of N719 dye and also the redox couple are shown. It is observed that the WF of graphene (−4.42 eV) is much close to both the FTO substrate (−4.7 eV) and the CB of TiO_2 (−4.21 eV) (Bhagwat *et al.,* 2017; Eshaghi & Aghaei, 2015).

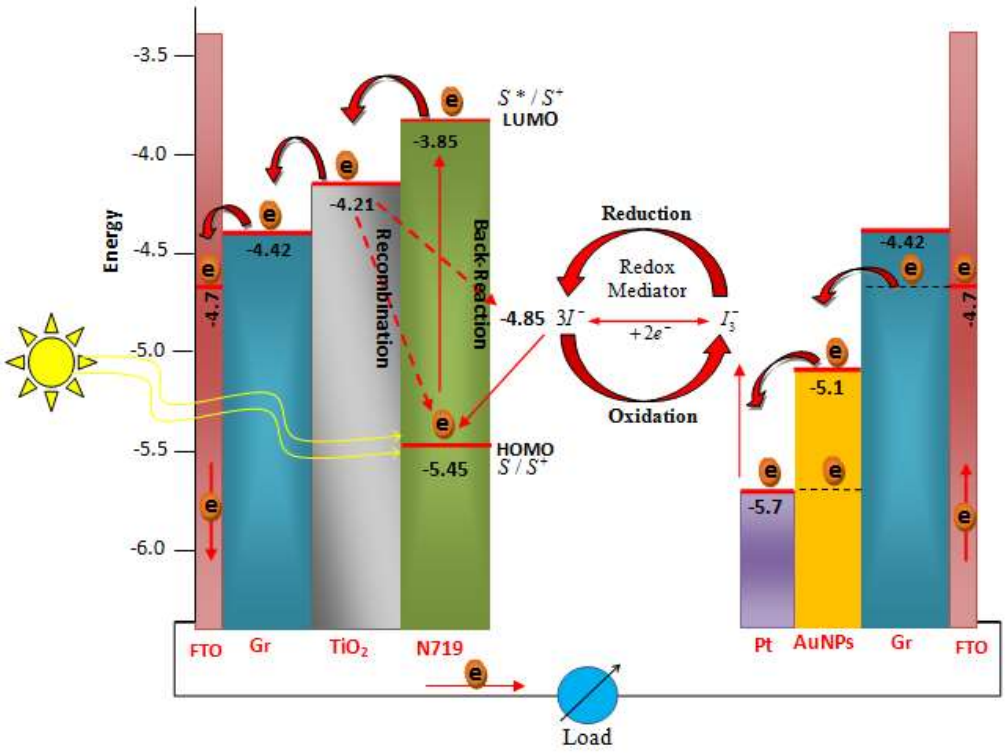

Figure 4.23: A schematic energy level and charge recombination diagram for the Gr/AuNPs/Pt composite DSSC. Shown are the CB for FTO, graphene, TiO2, AuNPs, Pt and the HOMO and LUMO levels of N719 dye and the redox couple.

The energy level of Gr lies between the CB of TiO_2 and that of FTO. It can be inferred that for such a composite structure under cell illumination, the photo excitons from the dye are transported via the CB of the graphene and TiO_2 to the CB of the TiO_2 (Chen, 2015). This transport path through the graphene CB builds to the already existing TiO_2 path. Since graphene possess excellent electrical conductivity and is homogenous throughout the structure, its bridging layer both at the PA and the CE acts as electron acceptor providing a channel for flawless collection of photo-excited electrons to the CB of TiO_2 and rapid transport to the FTO. This is consistent with reports by Yang *et al.*, (2010). Additionally, the resistance to electron transport within the graphene-TiO_2 interface is highly minimized with much suppression of the recombination and back-reaction processes compared to the graphene-free DSSC (Eshaghi & Aghaei, 2015; Fan *et al.*, 2012). Moreover, incorporating Gr has been shown to influence the PA surface morphology by activating additional sites necessary for dye adsorption and loading onto the TiO_2 (Eshaghi & Aghaei, 2015).

From the general composite DSSC design, a negative surface potential is created on the Pt surface during the charge transfer process. This generates a backward electron transfer kinetics making I_3^- to pick electrons with ease (Cheng *et al.,* 2013). Due to the excellent conductivity of the interfacing graphene, the electrons collected on the Pt surface are rapidly replaced (Katumo *et al.,* 2015). In addition, the large surface area and plasmonic effect of the AuNPs on the Pt surface connecting to the redox mediator, an enhanced catalytic activity on the composite CE is realized with the high concentrations of I_3^- reducing effective recombination (Boschloo & Hagfeldt, 2009). According to Cheng *et al.,* (2013), Pt surface within a Pt/Gr composite CE, has a low contact resistance compared to the bare Pt based CE. In this design, the inclusion of AuNPs over graphene further reduces this resistance making the CE better by enhancing its catalytic activity (Blanita & Lazar, 2013; Cheng *et al.,* 2013; Yue *et al.,* 2013). According to Cao *et al.,* (2010), combining small amounts of AuNPs with Pt yields a discrete distribution of nanostructures, also regarded as ‘‘nanoelectrodes. Such AuNPs/Pt composite offers large surface area leading to maximized diffusion of the redox species within the Pt pores, with similar effect expected in Gr/AuNPs CE based DSSCs. Additionally, the AuNPs and the high WF of Pt ensures sufficient total charge quantity over the CE surface. This offers rapid reduction of the redox species and improved transmission state.

CHAPTER FIVE

CONCLUSION AND RECOMMENDATIONS

5.1 Conclusion

Dye-sensitized solar cells are important optoelectronic devices capable of delivering a considerable photo-energy conversion over time. One way to enhance DSSC performance is by use of nanomaterials in CE designs. Structural modification of SC electrodes is complicated due to the difficulty in separating one material or parameter effect on the experimental data without influencing others. Understanding the contribution of each material introduced or eliminated from the structure is essential.

In this research, four DSSCs were assembled based on the fabricated composite CE modules, namely; FTO/Pt, FTO/Gr/Pt, FTO/Gr/AuNPs, and FTO/Gr/AuNPs/Pt. Their *J-V* characteristics were plotted, and corresponding PV performance compared. Based on the discussion of results in this thesis, the following conclusion was made: Mechanical exfoliation of flakes from HOPG provided a simple and convenient procedure for generating layered graphene samples for optical microscopy. By analyzing the RGB image contrast from the exfoliated flakes, a 99.2% correlation between the optical contrast and the number of graphene layer up to 7 layers based on polynomial fitting was established. Therefore, evaluation of the number of graphene layers in FLG is highly simplified. However, the generated flakes did not provide viable material for large surface area applications such as in DSSC electrode substrates. On the other hand, CVD graphene prepared on FTO depicted high transmittance (T_{550} = 0.76), large surface area coverage and universality in optical conductivity. In addition, it exhibited low defect levels and sp^2 hybridization based on Raman parameters, making it a candidate electrode module for SCs.

To evaluate the plasmonic effect of nanoparticles on DSSCs, ~12 nm citrate reduced colloidal gold was synthesized by varying the amount of 0.38 mM Na_3Ctr solution used on 0.254 mM $HAuCl_4$ from 0.85 to 1.15 mL. The sizes of NPs were evaluated

based on recorded LSPR (518 – 520 nm) from UV-Vis spectroscopy data, where the synthesized AuNPs depicted monodispersity as deduced from the FWHM values (46 – 50 nm) which had a low standard deviation (< 1) . The optimal amount of Na_3Ctr to use in preparing the 12 nm AuNPs was established to be between 1.00 to 1.15 mL with the LSPR peak wavelength being 518 nm. However, AuNPs of a particular size also exhibited multiple resonances, and attributed to the interband transitions.

The four CEs modules prepared presented optical transmittances above 70% at CE1 ($T_{550} > 0.76$), CE2 ($T_{550} > 0.73$), CE3 ($T_{550} > 0.78$) and CE4 ($T_{550} > 0.73$) depending on the composite materials used. This effectively influences the performance of the resulting DSSCs. The reduced transmittance in CE1, CE2 and CE4 could be attributed to the added Pt film.

The three DSSCs fabricated using Pt based CEs (CE1, CE2 and CE4) performed better than the Pt free CE (CE3). The DSSCs based on Gr/AuNPs/Pt CE presented the best performance with an efficiency of 4.62%. This research provides important data to establish the extent by which AuNPs and graphene contribute to enhancing the performance of Pt-based DSSCs when used either as a nanocomposite or independently within a CE. Individually, the contribution was 10.1% for AuNPs and 13.4% for Gr, while as Gr/AuNPs composite, an enhancement of 24.9% was realized. These findings provide viable information on nanocomposite CEs designs and the overall DSSC performance enhancement using nanomaterials, forming a basis for further research.

5.2 Recommendations

Although much focus of this work was on enhancement of the conventional Pt DSSCs by use of Gr/AuNPs composite based CEs and presented remarkable contribution towards PCE, the overall efficiencies of such DSSCs have been generally low even with the use of the best reported dyes, redox couple, and advanced cell designs. Further research on the following areas and aspects of DSSCs is recommended to understand the low efficiencies and bring more improvement on cell performance:

1. Investigate the existence charges barrier, existing within the composite material interfaces. Such barriers have negative impact on the DSSC performance. In this view, a critical investigation of the charge transfer behavior across the electrolyte in the various electrode designs would unravel the mechanisms behind the limited performance of the cells.
2. The low open circuit voltage exhibited by the iodide/triiodide electrolyte based DSSCs can be attributed to the electrolyte corrosion effect. As such, other redox electrolyte materials could be explored for integration with the composite DSSCs for possible cell improvement.
3. Investigate the best positioning of the plasmonic nanoparticles within the cell structure and optimize the nanoparticles sizes for best cell performance.

REFERENCES

Abadeer, N. S., & Murphy, C. J. (2016). Recent Progress in Cancer Thermal Therapy Using Gold Nanoparticles. *Journal of Physical Chemistry C*, *120*(9), 4691–4716.

Adawiyah, S. R., & Endarko. (2017). Structural and morphological characterization of TiO_2-SnO_2 thin film prepared by combining doctor-blade and sol-gel techniques. *IOP Conference Series: Materials Science and Engineering*, *188*(1), 012062.

Agunloye, E., Panariello, L., Gavriilidis, A., & Mazzei, L. (2018). A model for the formation of gold nanoparticles in the citrate synthesis method. *Chemical Engineering Science, 191*, 318–331.

Ahmadi, S., Asim, N., Alghoul, M. A., Hammadi, F. Y., Saeedfar, K., Ludin, N. A., Zaidi, S. H., & Sopian, K. (2014). The role of physical techniques on the preparation of photoanodes for dye sensitized solar cells. *International Journal of Photoenergy, 2014*(ID 198734), 1-19.

Alanazi, F. K., Radwan, A. A., & Alsarra, I. A. (2010). Biopharmaceutical applications of nanogold. *Saudi Pharmaceutical Journal*, *18*(4), 179–193.

Alzoubi F. Y., Alzouby J. Y., Alqadi M. K., Alshboul H. A., & Aljarrah K. M. (2015). Synthesis and Characterization of Colloidal Gold Nanoparticles Controlled by the pH and Ionic Strength. *Chinese Journal of Physics*, *53*(5), 100801.

Amendola, V., & Meneghetti, M. (2009). Size evaluation of gold nanoparticles by UV-vis spectroscopy. *Journal of Physical Chemistry C*, *113*(11), 4277–4285.

Amoabediny, H., Naderi, A., Malakootikhah, J., Koohi, M., Mortazavi, A., Naderi, M., & Rashedi, H. (2009). Guidelines for safe handling, use and disposal of nanoparticles. *Journal of Physics: Conference Series*, *170*, 012037.

Anker, J. N., Hall, W. P., Lyandres, O., Shah, N. C., Zhao, J., & Van Duyne, R. P. (2008). Biosensing with plasmonic nanosensors. *Nature Materials*, *7*(6), 442-453.

Arboleda, D. M., Santillán, J. M. J., Herrera, L. J. M., Muraca, D., Schinca, D. C., & Scaffardi, L. B. (2016). Size-dependent complex dielectric function of Ni, Mo, W, Pb, Zn and Na nanoparticles. Application to sizing. *Journal of Physics D: Applied Physics*, *49*(7), 75302.

Aruna, K., Rao, K. R., & Parhana, P. (2015). A systematic review on nanomaterials: properties, synthesis and applications. *I-Manager's Journal on Future Engineering and Technology*, *11*(2), 25.

Asim, N., Ahmadi, S., Alghoul, M. A., Hammadi, F. Y., Saeedfar, K., & Sopian, K. (2014). Research and development aspects on chemical preparation techniques of photoanodes for dye sensitized solar cells. *International Journal of Photoenergy*, *2014*(ID 518156), 21.

Atwater, H. A. (2007). The promise of Plasmonics. *Scientific American*, *296*(4), 56-63.

Atwater, H. A., & Polman, A. (2010). Plasmonics for improved photovoltaic devices. *Nature Materials*, *9*(3), 205–213.

Bai, S., & Shen, X. (2012). Graphene-inorganic nanocomposites. *RSC Advances*, *2*(1), 64–98.

Balandin, A. A., Ghosh, S., Bao, W., Calizo, I., Teweldebrhan, D., Miao, F., & Lau, C. N. (2008). Superior thermal conductivity of single-layer graphene. *Nano Letters, 8*(3), 902–907.

Bandara, T. M. W. J., Fernando, H. D. N. S., Rupasinghe, E. J., Ratnasekera, J. L., Chandrasena, P. H. N. J., Furlani, M., Albinsson, I., … & Mellander, B. E. (2016). N719 and N3 dyes for quasi-solid state dye sensitized solar cells - A comparative study using polyacrylonitrile and CsI based electrolytes. *Ceylon Journal of Science*, *45*(2), 61.

Barbagiovanni, E. G., Lockwood, D. J., Simpson, P. J., & Goncharova, L. V. (2014). Quantum confinement in Si and Ge nanostructures: theory and experiment. *Applied Physics Reviews*, *1*(1), 011302.

Barman, T., Hussain, A. A., Sharma, B., & Pal, A. R. (2015). Plasmonic hot hole generation by interband transition in gold-polyaniline. *Scientific Reports*, *5*(1), 453-462.

Bartelt, N. C., & McCarty, K. F. (2012). Graphene growth on metal surfaces. *MRS Bulletin*, *37*(12), 1158–1165.

Becquerel, A.-E. (1839). Recherches sur les effets de la radiation chimique de la lumiere solaire au moyen des courants electriques (Research on the effects of chemical radiation from solar light using electrical currents). *CR Acad. Sci*, *9*(145), 1.

Benítez–Martínez, S., López-Lorente, Á. I., & Valcárcel, M. (2015). Multilayer graphene–gold nanoparticle hybrid substrate for the SERS determination of metronidazole. *Microchemical Journal*, *121*, 6–13.

Berciaud, S., Cognet, L., Tamarat, P., & Lounis, B. (2005). Observation of intrinsic size effects in the optical response of individual gold nanoparticles. *Nano Letters*, *5*(3), 515–518.

Berger, C., Song, Z., Li, T., Li, X., Ogbazghi, A. Y., Feng, R., Dai, Z., Marchenkov, A. N., Conrad, E. H., & First, P. N. (2004). Ultrathin epitaxial graphite: 2D electron gas properties and a route toward graphene-based nanoelectronics. *The Journal of Physical Chemistry B*, *108*(52), 19912–19916.

Bessegato, G. G., Tasso Guaraldo, T., & Valnice Boldrin Zanoni, M. (2014). Enhancement of Photoelectrocatalysis Efficiency by Using Nanostructured Electrodes. In Mahmood Aliofkhazraei (Ed.), *Modern Electrochemical Methods in Nano, Surface and Corrosion Science* (271–319). InTech.

Beversluis, M., Bouhelier, A., & Novotny, L. (2003). Continuum generation from single gold nanostructures through near-field mediated intraband transitions. *Physical Review B - Condensed Matter and Materials Physics*, *68*(11), 25.

Bhagwat, S., Dani, R., Goswami, P., & Kerawalla, M. A. K. (2017). Recent advances in optimization of photoanodes and counter electrodes of dye-sensitized solar cells. *Current Science*, *113*(2), 228-235.

Bianco, G. V., Giangregorio, M. M., Losurdo, M., Sacchetti, A., Capezzuto, P., & Bruno, G. (2016). Demonstration of Improved Charge Transfer in Graphene/Au Nanorods Plasmonic Hybrids Stabilized by Benzyl Thiol Linkers. *Journal of Nanomaterials*, *2016*, 1–6.

Bing, D., Wang, Y., Bai, J., Du, R., Wu, G., & Liu, L. (2018). Optical contrast for identifying the thickness of two-dimensional materials.*Optics Communications*, *406*, 128–138.

Binnig, G., & Rohrer, H. (1987). Scanning tunneling microscopy from birth to adolescence. *Reviews of Modern Physics*, *59*(3), 615–625.

Blake, P., Hill, E. W., Castro Neto, A. H., Novoselov, K. S., Jiang, D., Yang, R., Booth, T. J., & Geim, A. K. (2007). Making graphene visible. *Applied Physics Letters*, *91*(6), 13–15.

Blanita, G., & Lazar, M. D. (2013). Review of Graphene-Supported Metal Nanoparticles as New and Efficient Heterogeneous *Catalysts*, *5*(2), 138-149.

Bora, T., Dousse, A., Sharma, K., Sarma, K., Baev, A., Hornyak, G. L., & Dasgupta, G. (2019). Modeling nanomaterial physical properties: theory and simulation. *International Journal of Smart and Nano Materials*, *10*(2), 116–143.

Borowiec, J., Wang, R., Zhu, L., & Zhang, J. (2013). Synthesis of nitrogen-doped graphene nanosheets decorated with gold nanoparticles as an improved sensor for electrochemical determination of chloramphenicol. *Electrochimica Acta*, *99*, 138–144.

Boschloo, G., & Hagfeldt, A. (2009). Characteristics of the iodide/triiodide redox mediator in dye-sensitized solar cells. *Accounts of Chemical Research*, *42*(11), 1819-1826.

Boyd, R. D., & Cuenat, A. (2011). New analysis procedure for fast and reliable size measurement of nanoparticles from atomic force microscopy images. *Journal of Nanoparticle Research*, *13*(1), 105–113.

Brown, G. F., & Wu, J. (2009). Third generation photovoltaics. *Laser and Photonics Reviews*, *3*(4), 394–405.

Burda, C., Chen, X., Narayanan, R., & El-Sayed, M. A. (2005). Chemistry and properties of nanocrystals of different shapes. *Chemical Reviews*, *105*(4), 1025–1102.

Cai, W., Zhu, Y., Li, X., Piner, R. D., & Ruoff, R. S. (2009). Large area few-layer graphene/graphite films as transparent thin conducting electrodes. *Applied Physics Letters*, *95*(12), 123115.

Campos, J. L. E., Miranda, H., Rabelo, C., Sandoz-Rosado, E., Pandey, S., Riikonen, J., Cano-Marquez, A. G., & Jorio, A. (2018). Applications of Raman spectroscopy in graphene-related materials and the development of parameterized PCA for large-scale data analysis. *Journal of Raman Spectroscopy*, *49*(1), 54–65.

Cao, G., Liu, Q., Huang, Y., Li, W., & Yao, S. (2010). Generation of gold nanostructures at the surface of platinum electrode by electrodeposition for ECL detection for CE. *Electrophoresis*, *31*(6), 1055-1062.

Casiraghi, C., Hartschuh, A., Lidorikis, E., Qian, H., Harutyunyan, H., Gokus, T., Novoselov, K. S., & Ferrari, A. C. (2007). Rayleigh imaging of graphene and graphene layers. *Nano Letters*, *7*(9), 2711–2717.

Castro Neto, A. H., Guinea, F., Peres, N. M. R., Novoselov, K. S., & Geim, A. K. (2009). The electronic properties of graphene. *Reviews of Modern Physics*, *81*(1), 109–162.

Castro Neto, A. H., Guinea, F., & Peres, N. M. R. (2006). Drawing conclusions from graphene. *Physics World*, *19*(11), 33–37.

Chang, Y. C., Liu, C. H., Liu, C. H., Zhong, Z., & Norris, T. B. (2014). Extracting the complex optical conductivity of mono- and bilayer graphene by ellipsometry. *Applied Physics Letters*, *104*(26), 261909.

Chen, D., Tang, L., & Li, J. (2010). Graphene-based materials in electrochemistry. *Chemical Society Reviews*, *39*(8), 3157–3180.

Chen, L.-C. (2015). Dye-Sensitized Solar Cells with Graphene Electron Extraction Layer. In S. Pyshkin & J. Ballato (Eds.), *Optoelectronics - Materials and Devices*. London: InTech.

Chen, Y. S., Hung, Y. C., Liau, I., & Huang, G. S. (2009). Assessment of the in vivo toxicity of gold nanoparticles. *Nanoscale Research Letters*, *4*(8), 858–864.

Cheng, C.-E. E., Lin, C.-Y. Y., Shan, C.-H. H., Tsai, S.-Y. Y., Lin, K.-W. W., Chang, C.-S. S., Chien, F. S.-S., & Shih-Sen Chien, F. (2013). Platinum-graphene counter electrodes for dye-sensitized solar cells. *Journal of Applied Physics*, *114*(1), 014503.

Childres, I., Jauregui, L. A., Park, W., Cao, H., & Chen, Y. P. (2013). Raman spectroscopy of graphene and related materials. *New developments in photon and materials research*, *1*, 1-20.

Cho, W., Lim, J., Kim, T. Y., Kim, Y. R., Song, D., Park, T., Fabregat-Santiago, F., … & Kang, Y. S. (2016). Electron-Transfer Kinetics through Interfaces between Electron-Transport and Ion-Transport Layers in Solid-State Dye-Sensitized Solar Cells Utilizing Solid Polymer Electrolyte. *Journal of Physical Chemistry C*., *120*(5), 2494-2500.

Choi, H., Kim, H., Hwang, S., Han, Y., & Jeon, M. (2011). Graphene counter electrodes for dye-sensitized solar cells prepared by electrophoretic deposition. *Journal of Materials Chemistry*, *21*(21), 7548.

Choy, K. L. (2003). Chemical vapour deposition of coatings. *Progress in Materials Science*, *48*(2), 57–170.

Cojocaru, L., Uchida, S., Jayaweera, P. V. V., Kaneko, S., Wang, H., Nakazaki, J., Kubo, T., & Segawa, H. (2017). Effect of TiO_2 Surface Treatment on the Current–Voltage Hysteresis of Planar-Structure Perovskite Solar Cells Prepared on Rough and Flat Fluorine-Doped Tin Oxide Substrates. *Energy Technology*, *5*(10), 1762-1766.

Conde, J., Doria, G., & Baptista, P. (2012). Noble Metal Nanoparticles Applications in Cancer. *Journal of Drug Delivery*, *2012*, 1–12.

Dagher, S., Haik, Y., Ayesh, A. I., & Tit, N. (2014). Synthesis and optical properties of colloidal CuO nanoparticles. *Journal of Luminescence*, *151*, 149–154.

Daniel, M. C., & Astruc, D. (2004). Gold Nanoparticles: Assembly, Supramolecular Chemistry, Quantum-Size-Related Properties, and Applications toward Biology, Catalysis, and Nanotechnology. *Chemical Reviews*, *104*(1), 293-346.

de Mello Donegá, C. (2014). The nanoscience paradigm:“size matters!” In de Mello Donegá C. (ed.), *Nanoparticles* (1–12) Berlin, Heidelberg: Springer.

Di Paola, A., Bellardita, M., & Palmisano, L. (2013). Brookite, the least known TiO_2 photocatalyst. *Catalysts*, *3*(1), 36–73.

Dissanayake, M. A. K. L., Kumari, J. M. K. W., Senadeera, G. K. R., & Thotawatthage, C. A. (2016). Efficiency enhancement in plasmonic dye-sensitized solar cells with TiO_2 photoanodes incorporating gold and silver nanoparticles. *Journal of Applied Electrochemistry*, *46*(1), 47–58.

Dobrovolskaia, M. A., Patri, A. K., Zheng, J., Clogston, J. D., Ayub, N., Aggarwal, P., Neun, B. W., Hall, J. B., & McNeil, S. E. (2009). Interaction of colloidal gold nanoparticles with human blood: effects on particle size and analysis of plasma protein binding profiles. *Nanomedicine: Nanotechnology, Biology, and Medicine*, *5*(2), 106–117.

Dodoo-Arhin, D., Fabiane, M., Bello, A., & Manyala, N. (2013). Graphene: Synthesis, Transfer, and Characterization for Dye-Sensitized Solar Cells Applications. *Industrial & Engineering Chemistry Research*, *52*(39), 14160–14168.

El-Sayed, M. A. (2001). Some interesting properties of metals confined in time and nanometer space of different shapes. *Accounts of Chemical Research*, *34*(4), 257–264.

El-Sayed, Mostafa A. (2004). Small is different: Shape-, size-, and composition-dependent properties of some colloidal semiconductor nanocrystals. *Accounts of Chemical Research*, *37*(5), 326–333.

Eshaghi, A., & Aghaei, A. A. (2015). Effect of TiO_2-graphene nanocomposite photoanode on dye-sensitized solar cell performance. *Bulletin of Materials Science*, *38*(5), 1177–1182.

Fan, J., Liu, S., & Yu, J. (2012). Enhanced photovoltaic performance of dye-sensitized solar cells based on TiO_2 nanosheets/graphene composite films. *Journal of Materials Chemistry, 22(33),* 17027-17036.

Fan, X., Zheng, W., & Singh, D. J. (2014). Light scattering and surface plasmons on small spherical particles. *Light: Science & Applications*, *3*(6), 179–179.

Fattori, A. (2010). *Electrochemical and Spectroelectrochemical Studies of Dyes used in Dye-sensitized Solar Cells*. Unpublished PhD Thesis, Bath: University of Bath.

Fei, Z., Shi, Y., Pu, L., Gao, F., Liu, Y., Sheng, L., Wang, B., Zhang, R., & Zheng, Y. (2008). High-energy optical conductivity of graphene determined by reflection contrast spectroscopy. *Physical Review B - Condensed Matter and Materials Physics*, *78*(20), 201402.

Ferrari, A. C., Meyer, J. C., Scardaci, V., Casiraghi, C., Lazzeri, M., Mauri, F., Piscanec, S., … & Geim, A. K. (2006). Raman spectrum of graphene and graphene layers. *Physical Review Letters*, *97*(18), 187401.

Ferrari, A.C. (2007). Raman spectroscopy of graphene and graphite: Disorder, electron-phonon coupling, doping and nonadiabatic effects. *Solid State Communications*, *143*(1–2), 47–57.

Feynman, R. P. (1992). There's plenty of room at the bottom. *Journal of Microelectromechanical Systems, 1*(1), 60 - 66.

Fortunato, E., Ginley, D., Hosono, H., & Paine, D. C. (2007). Transparent conducting oxides for photovoltaics. *MRS Bulletin*, *32*(3), 242–247.

Frens, G. (1973). Controlled Nucleation for the Regulation of the Particle Size in Monodisperse Gold Suspensions. *Nature Physical Science*, *241*(105), 20–22.

Fujii, S., Ziatdinov, M., Ohtsuka, M., Kusakabe, K., Kiguchi, M., & Enoki, T. (2014). Role of edge geometry and chemistry in the electronic properties of graphene nanostructures. *Faraday Discussions*, *173*, 173–199.

Gabor, N. M. (2013). Impact excitation and electron-hole multiplication in graphene and carbon nanotubes. *Accounts of Chemical Research*, *46*(6), 1348–1357.

Geim, A. K., & Novoselov, K. S. (2007). The rise of graphene. *Nature Materials*, *6*(3), 183–191.

Germer, T. A., Zwinkels, J. C., & Tsai, B. K. (2014). Theoretical Concepts in Spectrophotometric Measurements. *Experimental Methods in the Physical Sciences*, *46*, 11–66.

Ghifari, A., Long, D. X., Kim, S., Ma, B., & Hong, J. (2020). Transparent Platinum Counter Electrode Prepared by Polyol Reduction for Bifacial, Dye-Sensitized Solar Cells. *Nanomaterials*, *10*(3), 502.

Ghosh, D., & Chattopadhyay, N. (2013). Gold Nanoparticles: Acceptors for Efficient Energy Transfer from the Photoexcited Fluorophores. *Optics and Photonics Journal*, *03*(01), 18–26.

Ghosh, S. K., & Pal, T. (2007). Interparticle Coupling Effect on the Surface Plasmon Resonance of Gold Nanoparticles: From Theory to Applications. *Chemical Reviews*, *107*, 4797–4862.

Ginley D. S., & Perkins J. D. (2011) Transparent Conductors. In: Ginley D. (Ed.), *Handbook of transparent conductors* (1-25). Boston, MA: Springer.

Ginley, D. S., & Cahen, D. (2011). In David S. Ginley (Ed.), *Fundamentals of materials for energy and environmental sustainability*. Cambridge: Cambridge university press.

Gong, F., Wang, H., & Wang, Z.-S. (2011). Self-assembled monolayer of graphene/Pt as counter electrode for efficient dye-sensitized solar cell. *Physical Chemistry Chemical Physics*, *13*(39), 17676.

Gong, J., Liang, J., & Sumathy, K. (2012). Review on dye-sensitized solar cells (DSSCs): Fundamental concepts and novel materials. *Renewable and Sustainable Energy Reviews*, *16*(8), 5848–5860.

González, A. L., Noguez, C., Ortiz, G. P., & Rodríguez-Gattorno, G. (2005). Optical Absorbance of Colloidal Suspensions of Silver Polyhedral Nanoparticles. *The Journal of Physical Chemistry B*, *109*(37), 17512–17517.

Granqvist, C. G. (2007). Transparent conductors as solar energy materials: A panoramic review. *Solar Energy Materials and Solar Cells*, *91*(17), 1529–1598.

Grassian, V. H., O'Shaughnessy, P. T., Adamcakova-Dodd, A., Pettibone, J. M., & Thorne, P. S. (2007). Inhalation exposure study of Titanium dioxide nanoparticles with a primary particle size of 2 to 5 nm. *Environmental Health Perspectives*, *115*(3), 397–402.

Grätzel, C., & Zakeeruddin, S. M. (2013). Recent trends in mesoscopic solar cells based on molecular and nanopigment light harvesters. *Materials Today*, *16*(1–2), 11–18.

Grätzel, M. (2001). Molecular photovoltaics that mimic photosynthesis. In *Pure and Applied Chemistry, 73*(3), 432-442.

Grätzel, M. (2005). Solar energy conversion by dye-sensitized photovoltaic cells. *Inorganic Chemistry*, *44*(20), 6841–6851.

Green, M. A. (2002). Third generation photovoltaics: Solar cells for 2020 and beyond. *Physica E: Low-Dimensional Systems and Nanostructures*, *14*(1–2), 65–70.

Grobelny, J., Delrio, F. W., Pradeep, N., Kim -I, D., Hackley, V. A., and Cook, R. F. (2011). Size measurement of nanoparticles using atomic force microscopy,". In S. E. McNeil, (Ed.), Characterization of Nanoparticles Intended for Drug Delivery. *Methods in Molecular Biology* (71–82)., Switzerland: Springer.

Guo, X., Lu, G., & Chen, J. (2015). Graphene-based materials for photoanodes in dye-sensitized solar cells. *Frontiers in Energy Research*, *3*, 50.

Gupta, A., Chen, G., Joshi, P., Tadigadapa, S., & Eklund, P. C. (2006). Raman scattering from high-frequency phonons in supported n-graphene layer films. *Nano Letters*, *6*(12), 2667–2673.

Hagfeldt, A., Boschloo, G., Sun, L., Kloo, L., & Pettersson, H. (2010). Dye-Sensitized Solar Cells. *Chemical Reviews*, *110*(11), 6595–6663.

Hägglund, C., Zäch, M., & Kasemo, B. (2008). Enhanced charge carrier generation in dye sensitized solar cells by nanoparticle plasmons. *Applied Physics Letters*, *92*(1), 13113.

Haiss, W., Thanh, N. T. K., Aveyard, J., & Fernig, D. G. (2007). Determination of size and concentration of gold nanoparticles from UV-vis spectra. *Analytical Chemistry*, *79*(11), 4215–4221.

Hanžić, N., Jurkin, T., Maksimović, A., & Gotić, M. (2015). The synthesis of gold nanoparticles by a citrate-radiolytical method. *Radiation Physics and Chemistry*, *106*, 77–82.

Hardin, B. E., Snaith, H. J., & McGehee, M. D. (2012). The renaissance of dye-sensitized solar cells. *Nature Photonics*, *6*, 162–169.

Hasenoehrl, C., Alexander, C. M., Azzarelli, N. N., & Dabrowiak, J. C. (2012). Enhanced detection of gold nanoparticles in agarose gel electrophoresis. *Electrophoresis*, *33*(8), 1251–1254.

Hauch, A., & Georg, A. (2001). Diffusion in the electrolyte and charge-transfer reaction at the platinum electrode in dye-sensitized solar cells. *Electrochimica Acta*, *46*(22), 3457–3466.

Hayden, S. C., Zhao, G., Saha, K., Phillips, R. L., Li, X., Miranda, O. R., Rotello, V. M., El-Sayed, M. A., Schmidt-Krey, I., & Bunz, U. H. F. (2012). Aggregation and interaction of cationic nanoparticles on bacterial surfaces. *Journal of the American Chemical Society*, *134*(16), 6920-6923.

Haynes, H., Shinde, M., Nuraje, N., Subbaiyan, N. K., D'Souza, F., & Asmatulu, R. (2011). Experimental screen printing alternatives for the production of multi-layer dye sensitized solar cells. *Int. SAMPE Tech. Conf*, *43*, 14.

He, X., & Lu, H. (2014). Graphene-supported tunable extraordinary transmission. *Nanotechnology*, *25*(32), 325201.

Heidari, G., Mohammadi Rezaei, S., & Shirmahd, H. (2018). Comparative study of α-Fe_2O_3 films prepared by electrodeposition and spray pyrolysis methods as photoanode. *Journal of Materials Science: Materials in Electronics*, *29*(6), 4975–4980.

Hendel, T., Wuithschick, M., Kettemann, F., Birnbaum, A., Rademann, K., & Polte, J. (2014). In situ determination of colloidal gold concentrations with UV–Vis spectroscopy: limitations and perspectives. *Analytical Chemistry*, 86(22), 11115–11124.

Hendry, E., Koeberg, M., O'Regan, B., & Bonn, M. (2006). Local field effects on electron transport in nanostructured TiO_2 revealed by terahertz spectroscopy. *Nano Letters*, *6*(4), 755–759.

Hong, W., Xu, Y., Lu, G., Li, C., & Shi, G. (2008). Transparent graphene/PEDOT-PSS composite films as counter electrodes of dye-sensitized solar cells. *Electrochemistry Communications*, *10*(10), 1555–1558.

Hoshi, H., Tanaka, S., & Miyoshi, T. (2014). Pt-graphene electrodes for dye-sensitized solar cells. *Materials Science and Engineering: B*, *190*, 47–51.

Hu, J., Wang, Z., & Li, J. (2007). Gold nanoparticles with special shapes: Controlled synthesis, surface-enhanced raman scattering, and the application in biodetection. *Sensors*, *7*(12), 3299–3311.

Hu, M., Chen, J., Li, Z. Y., Au, L., Hartland, G. V., Li, X., Marquez, M., & Xia, Y. (2006). Gold nanostructures: Engineering their plasmonic properties for biomedical applications. *Chemical Society Reviews*, *35*(11), 1084–1094.

Huang, X., Jain, P. K., El-Sayed, I. H., & El-Sayed, M. A. (2007). Gold nanoparticles: Interesting optical properties and recent applications in cancer diagnostics and therapy. *Nanomedicine*, *2*(5), 681–693.

Huc, V., Bendiab, N., Rosman, N., Ebbesen, T., Delacour, C., & Bouchiat, V. (2008). Large and flat graphene flakes produced by epoxy bonding and reverse exfoliation of highly oriented pyrolytic graphite. *Nanotechnology*, *19*(45), 5601. 20 179801.

Huynh, T.-P. P., Hoang, T.-T., Nguyen, P.-H. H., Tran, T.-N. N., & Nguyen, T.-V. V. (2009). Preparation of TiO_2 thin film using modified doctor-blade method for improvement of dye-sensitized solar cell. *Conference Record of the IEEE Photovoltaic Specialists Conference*, 002168–002171.

IEO. (2018). International Energy Outlook 2018 (IEO2018) Key takeaways. In *U.S. Energy Information Administration* (Vol. IEO2018, Issue July).

Ismagilov, Z. R., Shikina, N. V., Mazurkova, N. A., Tsikoza, L. T., Tuzikov, F. V., Ushakov, V. A., Ishchenko, A. V., Rudina, N. A., Korneev, D. V., & Ryabchikova, E. I. (2012). Synthesis of nanoscale TiO_2 and study of the effect of their crystal structure on single cell response. *The Scientific World Journal*, *2012*, 498345.

Ito, S. (2011). Investigation of Dyes for Dye-Sensitized Solar Cells: Ruthenium-Complex Dyes, Metal-Free Dyes, Metal-Complex Porphyrin Dyes and Natural Dyes. In Kosyachenko L. (Ed.), *Solar Cells: Dye-Sensitized Devices*, 19-48. Croatia: InTech.

Jain, P. K., Huang, X., El-Sayed, I. H., & El-Sayed, M. A. (2008). Noble metals on the nanoscale: Optical and photothermal properties and some applications in imaging, sensing, biology, and medicine. *Accounts of Chemical Research*, *41*(12), 1578–1586.

Jain, P. K., Lee, K. S., El-Sayed, I. H., & El-Sayed, M. A. (2006). Calculated absorption and scattering properties of gold nanoparticles of different size, shape, and composition: Applications in biological imaging and biomedicine. *Journal of Physical Chemistry B*, *110*(14), 7238–7248.

Jalali, M., Moakhar, R. S., Kushwaha, A., Goh, G. K. L., Sadrnezhaad, S. K., & Riahi-Noori, N. (2015). TiO_2 surface nanostructuring for improved dye loading and light scattering in double-layered screen-printed dye-sensitized solar cells. *Journal of Applied Electrochemistry*, *45*(8), 831–838.

Jana, J., Ganguly, M., & Pal, T. (2016). Enlightening surface plasmon resonance effect of metal nanoparticles for practical spectroscopic application. *RSC Advances*, *6*(89), 86174–86211.

Jana, N. R., Gearheart, L., & Murphy, C. J. (2001). Seeding growth for size control of 5-40 nm diameter gold nanoparticles. *Langmuir*, *17*(22), 6782–6786.

Jang, Y. H., Jang, Y. J., Kochuveedu, S. T., Byun, M., Lin, Z., & Kim, D. H. (2014). Plasmonic dye-sensitized solar cells incorporated with Au-TiO_2 nanostructures with tailored configurations. *Nanoscale*, *6*(3), 1823–1832.

Jayawardena, K. D. G. I., Rozanski, L. J., Mills, C. A., Beliatis, M. J., Nismy, N. A., & Silva, S. R. P. (2013). "Inorganics-in-Organics": Recent developments and outlook for 4G polymer solar cells. *Nanoscale*, *5*(18), 8411–8427.

Jeevanandam, J., Barhoum, A., Chan, Y. S., Dufresne, A., & Danquah, M. K. (2018). Review on nanoparticles and nanostructured materials: History, sources, toxicity and regulations. *Beilstein Journal of Nanotechnology*, *9*(1), 1050-1074.

Jennings, J. R., Liu, Y., & Wang, Q. (2011). Efficiency limitations in dye-sensitized solar cells caused by inefficient sensitizer regeneration. *Journal of Physical Chemistry C*, *115*(30), 15109–15120.

Ji, X., Song, X., Li, J., Bai, Y., Yang, W., & Peng, X. (2007). Size Control of Gold Nanocrystals in Citrate Reduction: The Third Role of Citrate. *Journal of the American Chemical Society*, *129*(45), 13939–13948.

John, B. M., Ngumbi, P. K., Katumo, N., Mugo, S. W., Timonah, N., & Ngaruiya, J. M. (2015). Determination of Graphene Layers by Optical Imaging Contrast Analysis. *International Journal of Innovative Research in Science, Engineering and Technology*, *4*(11), 1111–1115.

Jorio, A. (2012). Raman spectroscopy in graphene-based systems: prototypes for nanoscience and nanometrology. *International Scholarly Research Notices, Nanotechnology*, 16.

Jung, I., Pelton, M., Piner, R., Dikin, D. A., Stankovich, S., Watcharotone, S., Hausner, M., & Ruoff, R. S. (2007). Simple approach for high-contrast optical imaging and characterization of graphene-based sheets. *Nano Letters*, *7*(12), 3569–3575.

Kabashin, A. V., Meunier, M., Kingston, C., & Luong, J. H. T. (2003). Fabrication and characterization of gold nanoparticles by femtosecond laser ablation in an aqueous solution of cyclodextrins. *Journal of Physical Chemistry B*, *107*(19), 4527–4531.

Kakiage, K., Aoyama, Y., Yano, T., Oya, K., Fujisawa, J. I., & Hanaya, M. (2015). Highly-efficient dye-sensitized solar cells with collaborative sensitization by silyl-anchor and carboxy-anchor dyes. *Chemical Communications*, *51*(88), 15894–15897.

Kanchi, S., Sharma, D., & Bisetty, K. (2014). Dye Sensitized Solar Cells: Tool to Overcome the Future Energy Crisis. *Journal of Environmental Analytical Chemistry*, *02*(01), 1–2.

Kandimalla, V. K. (2010). *Influence of Metal Nanoparticles on Fluorescence Properties.* Unpublished Master's Theses, Michigan: Eastern Michigan University.

Katoh, R. (2012). Quantitative evaluation of electron injection efficiency in dye-sensitized TiO_2 films. *Ambio*, *41*(2), 143-148.

Katoh, R., Huijser, A., Hara, K., Savenije, T. J., & Siebbeles, L. D. A. (2007). Effect of the particle size on the electron injection efficiency in dye-sensitized nanocrystalline TiO_2 films studied by Time-Resolved Microwave Conductivity (TRMC) measurements. *Journal of Physical Chemistry C*, *111*(28), 10741-1074.

Katumo, N., W. Mugo, S., M. Ngaruiya, J., K. Ngumbi, P., & Mbaluka, B. (2015). Graphene Supported Platinum Counter Electrode for Dye Sensitized Solar Cells. *International Journal of Innovative Research in Science, Engineering and Technology 3297*(4), 12251–12257.

Khalil, I., Julkapli, N. M., Yehye, W. A., Basirun, W. J., & Bhargava, S. K. (2016). Graphene-gold nanoparticles hybrid-synthesis, functionalization, and application in an electrochemical and surface-enhanced Raman scattering biosensor. *Materials*, *9*(6), 406.

Khan, I., Saeed, K., & Khan, I. (2019). Nanoparticles: Properties, applications and toxicities. *Arabian Journal of Chemistry*, *12*(7), 908–931.

Kheirandish, A., Javan, N. S., & Mohammadzadeh, H. (2020). Modified Drude model for small gold nanoparticles surface plasmon resonance based on the role of classical confinement. *Scientific Reports*, *10*(1), 1–10.

Khlebtsov, B. N., & Khlebtsov, N. G. (2011). On the measurement of gold nanoparticle sizes by the dynamic light scattering method. *Colloid Journal*, *73*(1), 118–127.

Khlebtsov, N. G. (2008). Determination of size and concentration of gold nanoparticles from extinction spectra. *Analytical Chemistry*, *80*(17), 6620–6625.

Kibona, T. E., Shao, G. N., Kim, H. T., & King'ondu, C. K. (2019). Specific capacitance–pore texture relationship of biogas slurry mesoporous carbon/MnO_2 composite electrodes for supercapacitors. *Nano-Structures and Nano-Objects*, *17*, 21-33.

Kim, K. S., Zhao, Y., Jang, H., Lee, S. Y., Kim, J. M., Kim, K. S., Ahn, J. H., Kim, P., Choi, J. Y., & Hong, B. H. (2009). Large-scale pattern growth of graphene films for stretchable transparent electrodes. *Nature*, *457*(7230), 706–710.

Kim, S. K., Raj, C. J., & Kim, H. J. (2014). CdS/CdSe quantum dot-sensitized solar cells based on ZnO nanoparticle/nanorod composite electrodes. *Electronic Materials Letters*, *10*(6), 1137–1142.

Kimoto, T. (2019). SiC Material Properties. In B. J. Baliga (Ed.), *Wide Bandgap Semiconductor Power Devices* (1st ed., 21–42). Kyoto, Japan: Woodhead publishing.

Kolwas, K., & Derkachova, A. (2013). Damping rates of surface plasmons for particles of size from nano-to micrometers; reduction of the nonradiative decay. *Journal of Quantitative Spectroscopy and Radiative Transfer*, *114*, 45–55.

Kongkanand, A., Dominguez, R. M., and Kamat, P. V. (2007). Single wall carbon nanotube scaffolds for photoelectrochemical solar cells. Capture and transport of photogenerated electrons. *Nano Letters*, *7*(3), 676–680.

Koole, R., Groeneveld, E., Vanmaekelbergh, D., Meijerink, A., & de Mello Donegá, C. (2014). Size effects on semiconductor nanoparticles. In de Mello Donegá C. (Ed.), *Nanoparticles* (13–51). Berlin: Springer,

Koshino, M., & Ando, T. (2008). Magneto-optical properties of multilayer graphene. *Physical Review B - Condensed Matter and Materials Physics*, *77*(11), 1–9.

Kosynkin, D. V., Higginbotham, A. L., Sinitskii, A., Lomeda, J. R., Dimiev, A., Price, B. K., & Tour, J. M. (2009). Longitudinal unzipping of carbon nanotubes to form graphene nanoribbons. *Nature*, *458*(7240), 872–876.

Kravets, V. G., Schedin, F., Jalil, R., Britnell, L., Novoselov, K. S., & Grigorenko, A. N. (2012). Surface Hydrogenation and Optics of a Graphene Sheet Transferred onto a Plasmonic Nanoarray. *The Journal of Physical Chemistry C*, *116*(6), 3882–3887.

Kroto, H.W., Heath, J. R., O'Brien, S. C., Curl, R. F., & Smalley, R. E. (1985). C60: Buckminsterfullerene. *Nature*, *318*(6042), 162–163.

Kuchibhatla, S. V. N. T., Karakoti, A. S., Bera, D., & Seal, S. (2007). One dimensional nanostructured materials. *Progress in Materials Science*, *52*(5), 699–913.

Kumar, S., Gandhi, K. S., & Kumar, R. (2007). Modeling of formation of gold nanoparticles by citrate method. *Industrial and Engineering Chemistry Research*, *46*(10), 3128–3136.

Kumar, S. (2007). *Plasmonic Nanoparticles for Imaging Intracellular Biomarkers*, Unpublished PhD thesis, Texas: The University of Texas at Austin.

Kusama, H., & Sayama, K. (2015). A comparative computational study on the interactions of N719 and N749 dyes with iodine in dye-sensitized solar cells. *Physical Chemistry Chemical Physics*, *17*(6), 4379–4387.

Kuzmenko, A. B., Heumen, E. Van, Carbone, F., Marel, D. Van Der, Van Heumen, E., Carbone, F., & Van Der Marel, D. (2008). Universal optical conductance of graphite. *Physical Review Letters*, *100*(11), 117401.

Lalwani, G., Henslee, A. M., Farshid, B., Lin, L., Kasper, F. K., Qin, Y. X., Mikos, A. G., & Sitharaman, B. (2013). Two-dimensional nanostructure-reinforced biodegradable polymeric nanocomposites for bone tissue engineering. *Biomacromolecules*, *14*(3), 900-909.

Lan, J. L., Wang, Y. Y., Wan, C. C., Wei, T. C., Feng, H. P., Peng, C., Cheng, H. P., Chang, Y. H., & Hsu, W. C. (2010). The simple and easy way to manufacture counter electrode for dye-sensitized solar cells. *Current Applied Physics*, *10*(2), S168–S171.

Laurenti, M., & Cauda, V. (2018). Porous zinc oxide thin films: Synthesis approaches and applications. *Coatings*, *8*(2), 67.

Lee, C. P., Li, C. T., & Ho, K. C. (2017). Use of organic materials in dye-sensitized solar cells. *Materials Today*, *20*(5), 267–283.

Lee, S. K., Kim, H., & Shim, B. S. (2013). Graphene: an emerging material for biological tissue engineering. *Carbon Letters*, *14*(2), 63–75.

Lemme, M. C. (2009). Current status of graphene transistors. *Solid State Phenomena*, *156–158*, 499–509.

Li, H., Yuan, K., Zhang, Y., & Wang, J. (2013). Synthesis of Au-SiO_2 asymmetric clusters and their application in ZnO nanosheet-based dye-sensitized solar cells. *ACS Applied Materials and Interfaces*, *5*(12), 5601–5608.

Li, J. J., An, H. Q., Zhu, J., & Zhao, J. W. (2015). Improve the surface enhanced Raman scattering of gold nanorods decorated graphene oxide: The effect of CTAB on the electronic transition. *Applied Surface Science*, *347*, 856–860.

Li, P.-J., Chen, K., Chen, Y.-F., Wang, Z.-G., Hao, X., Liu, J.-B., He, J.-R., & Zhang, W.-L. (2012). Low platinum loading PtNPs/graphene composite catalyst with high electrocatalytic activity for dye-sensitized solar cells. *Chinese Physics B*, *21*(11), 118101.

Liao, Z. X., Liu, M. C., Kempson, I. M., Fa, Y. C., & Huang, K. Y. (2017). Light-triggered methylcellulose gold nanoparticle hydrogels for leptin release to inhibit fat stores in adipocytes. *International Journal of Nanomedicine*, *12*, 7603–7611

Lin, C.-C., Kuo, M.-T., & Chang, H.-C. (2010). Raman spectroscopy–a novel tool for noninvasive analysis of ocular surface fluid. *Journal of Medical and Biological Engineering*, *30*(6), 343–354.

Lin, S.-J., Lee, K.-C., Wu, J.-L., & Wu, J.-Y. (2012). Plasmon-enhanced photocurrent in dye-sensitized solar cells. *Solar Energy*, *86*(9), 2600–2605.

Link Stephan, & El-Sayed, M. A. (1999). Size and temperature dependence of the plasmon absorption of colloidal gold nanoparticles," *Journal of Physical Chemistry B*, *103*(21), 4212–4217.

Link, Stephan, & El-Sayed, M. A. (2000). Shape and size dependence of radiative, non-radiative and photothermal properties of gold nanocrystals. *International Reviews in Physical Chemistry*, *19*(3), 409–453.

Liu, D.-W., Cheng, I.-C., Chen, J. Z., Chen, H.-W., Ho, K.-C., & Chiang, C.-C. (2012). Enhanced optical absorption of dye-sensitized solar cells with microcavity-embedded TiO_2 photoanodes. *Optics Express*, *20*(S2), A168.

Liz-Marzán, L. M. (2004). Nanometals: Formation and color. *Materials Today*, *7*(2), 26–31.

Long, N. N., Vu, L. Van, Kiem, C. D., Doanh, S. C., Nguyet, C. T., Hang, P. T., Thien, N. D., & Quynh, L. M. (2009). Synthesis and optical properties of colloidal gold nanoparticles. *Journal of Physics: Conference Series*, *187*, 12026.

Luceño-Sánchez, J. A., Díez-Pascual, A. M., & Capilla, R. P. (2019). Materials for photovoltaics: State of art and recent developments. *International Journal of Molecular Sciences*, *20*(4), 976.

Mak, K. F., Ju, L., Wang, F., & Heinz, T. F. (2012). Optical spectroscopy of graphene: From the far infrared to the ultraviolet. *Solid State Communications*, *152*(15), 1341–1349.

Maier, S. A. (2007). *Plasmonics: fundamentals and applications*. UK: Springer Science & Business Media.

Maluta, N. (2010). *Simulations of dye-sensitized solar cells*. Unpublished PhD Thesis, UK: University of Bath.

Mao, M., Wang, J. B., Xiao, Z. F., Dai, S. Y., & Song, Q. H. (2012). New 2,6-modified BODIPY sensitizers for dye-sensitized solar cells. *Dyes and Pigments*, *94*(2), 224–232.

Marinakos, S. M., Chen, S., & Chilkoti, A. (2007). Plasmonic detection of a model analyte in serum by a gold nanorod sensor. *Analytical Chemistry*, *79*(14), 5278–5283.

Matsuura, Y., Nakamura, A., & Kato, H. (2018). Determination of Nanoparticle Size Using a Flow Particle-Tracking Method. *Analytical Chemistry*, *90*(6), 4182–4187.

Mattevi, C., Kim, H., & Chhowalla, M. (2011). A review of chemical vapour deposition of graphene on copper. *J. Mater. Chem.*, *21*(10), 3324–3334.

Mayumi, S., Ikeguchi, Y., Nakane, D., Ishikawa, Y., Uraoka, Y., & Ikeguchi, M. (2017). Effect of Gold Nanoparticle Distribution in TiO_2 on the Optical and Electrical Characteristics of Dye-Sensitized Solar Cells. *Nanoscale Research Letters*, *12*(1), 513.

McConnell, R. D. (2002). Assessment of the dye-sensitized solar cell. *Renewable and Sustainable Energy Reviews*, *6*(3), 271–293.

McKittrick, J., & Shea-Rohwer, L. E. (2014). Review: Down conversion materials for solid-state lighting. *Journal of the American Ceramic Society*, *97*(5), 1327–1352.

McLeod, A., Kumar, S., Vernon, K. C., & Ostrikov, K. (2015). Vertical graphene nanosheets coated with gold nanoparticle arrays: Effect of interparticle spacing on optical response. *Journal of Nanomaterials*, *2015*, 1–7.

Mehmood, U., Rahman, S. U., Harrabi, K., Hussein, I. A. I. A., & Reddy, B. V. S. V. S. (2014). Recent advances in dye sensitized solar cells. *Advances in Materials Science and Engineering*, *2014*, 1–12.

Melville, J., & Kapelewski, M. (2015). Optical Properties of Quantum Dots. *UC Berkeley College of Chemistry*, 2–3.

Mendes, R., Fernandes, A. R., & Baptista, P. V. (2017). Gold nanoparticle approach to the selective delivery of gene silencing in cancer-The case for combined delivery? *Genes*, *8*(3), 94.

Meyer, E., Taziwa, R., Mutukwa, D., & Zingwe, N. (2018). A review on the advancement of ternary alloy counter electrodes for use in dye-sensitised solar cells. *Metals*, *8*(12), 1080.

Mie, G. (1976). Contributions to the optics of turbid media, particularly of colloidal metal solutions. *Contributions to the Optics of Turbid Media*, *25*(3), 377–445.

Min, H., & MacDonald, A. H. (2009). Origin of universal optical conductivity and optical stacking sequence identification in multilayer graphene. *Physical Review Letters*, *103*(6), 067402.

Mishchenko, G., & Halperin, I. (2003). Transport equations for a two-dimensional electron gas with spin-orbit interaction. *Physical Review B*, *68*(4), 045317.

Mohamad, I. S., Ismail, S. S., Norizan, M. N., Murad, S. A. Z., & Abdullah, M. M. A. (2017). ZnO photoanode effect on the efficiency performance of organic based dye sensitized solar cell. *IOP Conference Series: Materials Science and Engineering*, *209*(1), 12028

Moskovits, M. (1985). Surface-enhanced spectroscopy. *Reviews of modern physics*, *57*(3), 783.

Muhammed, G. S., Abdullah, M. M., & Alsammarraie, A. M. A. (2018). Efficiency enhancement of flexible dye sensitized solar cell using TiO_2 nanotube/ZnS nanoparticles photoanode. *Asian Journal of Chemistry*, *30*(6).

Muñoz, R., & Gómez-Aleixandre, C. (2013). Review of CVD synthesis of graphene. *Chemical Vapor Deposition*, *19*(10-11-12), 297-322.

Nair, R. R., Blake, P., Grigorenko, A. N., Novoselov, K. S., Booth, T. J., Stauber, T., Peres, N. M. R., & Geim, A. K. (2008). Fine structure constant defines visual transparency of graphene. *Science*, *320*(5881), 1308.

Nel, A., Xia, T., Mädler, L., & Li, N. (2006). Toxic potential of materials at the nanolevel. *Science*, *311*(5761), 622–627.

Nelson, J. (2003). The Physics of Solar Cells. *World Scientific Publishing Company*.

Ni, Z. H., Wang, H. M., Kasim, J., Fan, H. M., Yu, T., Wu, Y. H., Feng, Y. P., & Shen, Z. X. (2007). Graphene thickness determination using reflection and contrast spectroscopy. *Nano Letters*, *7*(9), 2758–2763.

Niu, B., Wang, X., Wu, K., He, X., & Zhang, R. (2018). Mesoporous titanium dioxide: Synthesis and applications in photocatalysis, energy and biology. *Materials*, *11*(10), 1910.

Nivea, R., Gunasekaran, V., Kannan, R., Sakthivel, T., & Govindan, K. (2014). Enhanced photocatalytic efficacy of hetropolyacid pillared TiO_2 nanocomposites. *Journal of nanoscience and nanotechnology*, *14*(6), 4383–4386.

Novoselov, K. S., Geim, A. K., Morozov, S. V., Jiang, D., Zhang, Y., Dubonos, S. V., Grigorieva, I. V., & Firsov, A. A. (2004). Electric field in atomically thin carbon films. *Science*, *306*(5696), 666–669.

Novoselov, K. S., Jiang, D., Schedin, F., Booth, T. J., Khotkevich, V. V., Morozov, S. V., & Geim, A. K. (2005). Two-dimensional atomic crystals. *Proceedings of the National Academy of Sciences*, *102*(30), 10451–10453.

NREL. (2019). Best Research-Cell Efficiency Chart Photovoltaic Research. National Renewable Energy Laboratory. *Nature*, *567*(7749), 511-515.

O'Regan, B. C., & Durrant, J. R. (2009). Kinetic and energetic paradigms for dyesensitized solar cells: Moving from the ideal to the real. *Accounts of Chemical Research*, *42*(11), 1799–1808.

O'Regan, B., & Grätzel, M. (1991). A low-cost, high-efficiency solar cell based on dye-sensitized colloidal TiO_2 films. *Nature*, *353*(6346), 737–740.

Oliveira, J. P., Prado, A. R., Keijok, W. J., Ribeiro, M. R. N., Pontes, M. J., Nogueira, B. V, & Guimarães, M. C. C. (2020). A helpful method for controlled synthesis of monodisperse gold nanoparticles through response surface modeling. *Arabian Journal of Chemistry*, *13*(1), 216–226.

Padinger, F., Brabec, C. J., Fromherz, T., Hummelen, J. C., & Sariciftci, N. S. (2000). Fabrication of large area photovoltaic devices containing various blends of polymer and fullerene derivatives by using the doctor blade technique. *Opto-Electronics Review*, *8*(4), 280-283.

Pal, B., Rana, S., & Kaur, R. (2015). Influence of different reducing agents on the Ag nanostructures and their electrokinetic and catalytic properties. *Journal of Nanoscience and Nanotechnology*, *15*(4), 2753–2760.

Palmer, J. (1995). The measurement of transmission, absorption, emission, and reflection. In M. Bass, E. W. van Strylan, D. R. Williams and W. L. Wolfe (Eds.), *Handbook of optics* (1–25). New York: McGraw-Hill.

Park, M. H., Kim, T. H., & Yang, C. W. (2012). Thickness contrast of few-layered graphene in SEM. *Surface and Interface Analysis*, *44*(11–12), 1538–1541.

Parveen, K., Banse, V., & Ledwani, L. (2016). Green synthesis of nanoparticles: Their advantages and disadvantages. *AIP Conference Proceedings*, *1724*(1), 20048.

Patil, B. R. (2017). *Interfacial layers and semi-transparent electrodes for large area flexible organic photovoltaics*. Unpublished PhD dissertation, Denmark: University of Southern Denmark.

Patil, Y. B., Swaminathan, S. K., Sadhukha, T., Ma, L., & Panyam, J. (2010). The use of nanoparticle-mediated targeted gene silencing and drug delivery to overcome tumor drug resistance. *Biomaterials*, *31*(2), 358–365.

Patungwasa, W., & Hodak, J. H. (2008). pH tunable morphology of the gold nanoparticles produced by citrate reduction. *Materials Chemistry and Physics*, *108*(1), 45–54.

Peng, K. Q., & Lee, S. T. (2011). Silicon nanowires for photovoltaic solar energy conversion. *Advanced Materials*, *23*(2), 198–215.

Perera, F. (2018). Pollution from fossil-fuel combustion is the leading environmental threat to global pediatric health and equity: Solutions exist. *International journal of environmental research and public health*, *15*(1), 16.

Pimpang, P., & Choopun, S. (2011). Monodispersity and Stability of Gold Nanoparticles Stabilized by Using Polyvinyl Alcohol. *Chiang Mai Journal of Science*, *38*(1), 31–38.

Piwoński, I., Soliwoda, K., Kisielewska, A., Stanecka-Badura, R., & Ka, K. (2013). The effect of the surface nanostructure and composition on the antiwear properties of zirconia–titania coatings. *Ceramics International*, *39*(2), 1111–1123.

Polman, A., & Atwater, H. A. (2012). Photonic design principles for ultrahigh-efficiency photovoltaics. *Nature Materials*, *11*(3), 174–177.

Polte, J. (2015). Fundamental growth principles of colloidal metal nanoparticles - a new perspective. *CrystEngComm*, *17*(36), 6809–6830.

Ponken, T., Tagsin, K., Suwannakhun, C., Luecha, J., & Choawunklang, W. (2017). Preparation of Platinum (Pt) Counter Electrode Coated by Electrochemical Technique at High Temperature for Dye-sensitized Solar Cell (DSSC) Application. *Journal of Physics: Conference Series*, *901*(1), 012084.

Qin, Y., & Peng, Q. (2012). Ruthenium sensitizers and their applications in dye-sensitized solar cells. *International Journal of Photoenergy*, *2012*, 1–21.

Qiu, C., Bennet, K. E., Khan, T., Ciubuc, J. D., & Manciu, F. S. (2016). Raman and conductivity analysis of graphene for biomedical applications. *Materials*, *9*(11), 897.

Qu, D., Liu, F., Pan, X., Yu, J., Li, X., Xie, W., Xu, Q., & Huang, Y. (2011). Plasmonic core-shell nanoparticle enhanced optical absorption in thin film organic solar cells. *Conference Record of the IEEE Photovoltaic Specialists Conference*, 000924–000928.

Rahman, M. M., Chandra Deb Nath, N., & Lee, J. (2015). Electrochemical Impedance Spectroscopic Analysis of Sensitization-Based Solar Cells. *Israel Journal of Chemistry*, *55*(9), 990–1001.

Rasheed, A. K., Khalid, M., Rashmi, W., Gupta, T. C. S. M., & Chan, A. (2016). Graphene based nanofluids and nanolubricants - Review of recent developments. *Renewable and Sustainable Energy Reviews, 63, 346-362*.

Reimann, S. M., & Manninen, M. (2002). Electronic structure of quantum dots. *Reviews of Modern Physics*, *74*(4), 1283.

Reina, A., Jia, X., Ho, J., Nezich, D., Son, H., Bulovic, V., Dresselhaus, M. S., & Kong, J. (2009). Large Area, Few-Layer Graphene Films on Arbitrary Substrates by Chemical Vapor Deposition. *Nano Letters*, *9*(1), 30–35.

Ren, N. F., Huang, L. J., Li, B. J., & Zhou, M. (2014). Laser-assisted preparation and photoelectric properties of grating-structured Pt/FTO thin films. *Applied surface science*, *314*, 208-214.

Ricci, R. W., Ditzler, M. A., & Nestor, L. P. (1994). Discovering the Beer-Lambert law. *Journal of Chemical Education*, *71*(11), 983–985.

Roy-Mayhew, J. D., & Aksay, I. A. (2014). Graphene materials and their use in dye-sensitized solar cells. *Chemical Reviews, 114*(12), 6323–6348.

Roy-Mayhew, J. D., Bozym, D. J., Punckt, C., & Aksay, I. A. (2010). Functionalized graphene as a catalytic counter electrode in dye-sensitized solar cells. *ACS Nano*, *4*(10), 6203–6211.

Sadikin, S. N., Rahman, M. Y. A., Umar, A. A., & Salleh, M. M. (2017). Effect of spin-coating cycle on the properties of TiO_2 thin film and performance of DSSC. *International Journal of Electrochemical Science*, *12*(6), 5529–5538.

Saito, R., Dresselhaus, G., & Dresselhaus, M. S. (1998). Physical Properties of Carbon Nanotubes. *Properties of Carbon Nanotubes*. London: Imperial College Press.

Sakurai, T., Trirongjitmoah, S., Nishibata, Y., Namita, T., Tsuji, M., Hui, S.-P., Jin, S., Shimizu, K., & Chiba, H. (2010). Measurement of lipoprotein particle sizes using dynamic light scattering. *Annals of Clinical Biochemistry*, *47*(5), 476–481.

Saleh, B. E. A., & Teich, M. C. (2007). *Fundamentals of Photonics* (2nd ed.) New York: Wiley.

Sampaio, P. G. V., & González, M. O. A. (2017). Photovoltaic solar energy: Conceptual framework. *Renewable and Sustainable Energy Reviews*, *74*, 590-601.

Sarkar, A. S., Rao, A. D., Jagdish, A. K., Gupta, A., Nandi, C. K., Ramamurthy, P. C., & Pal, S. K. (2018). Facile embedding of gold nanostructures in the hole transporting layer for efficient polymer solar cells. *Organic Electronics*, *54*, 148–153.

Scarselli, M., Castrucci, P., & De Crescenzi, M. (2012). Electronic and optoelectronic nano-devices based on carbon nanotubes. *Journal of Physics Condensed Matter*, *24*(31), 313202.

Sclafani, A., & Herrmann, J. M. (1996). Comparison of the photoelectronic and photocatalytic activities of various anatase and rutile forms of titania in pure liquid organic phases and in aqueous solutions. *Journal of Physical Chemistry*, *100*(32).

Sedghi, A., & Miankushki, H. N. (2015). The effect of drying and thickness of TiO_2 electrodes on the photovoltaic performance of dye-sensitized solar cells. *International Journal of Electrochemical Science*, *10*(4), 3354–3362.

Sedghi, A., & Miankushki, H. nourmohammadi. (2014). Effect of multi walled carbon nanotubes as counter electrode on dye sensitized solar cells. *International Journal of Electrochemical Science, 9*(4), 2029-2037.

Semonin, O. E., Luther, J. M., Choi, S., Chen, H. Y., Gao, J., Nozik, A. J., & Beard, M. C. (2011). Peak external photocurrent quantum efficiency exceeding 100% via MEG in a quantum dot solar cell. *Science*, *334*(6062), 1530–1533.

Shaikh, F. S., M. Shinde, N., Lee, D., M. Al-Enizi, A., Ho Kim, K., & S. Mane, R. (2019). Nanostructures in Dye-Sensitized and Perovskite Solar Cells. In *Nanostructures,* London: IntechOpen.

Shalini, S., Balasundaraprabhu, R., Satish Kumar, T., Prabavathy, N., Senthilarasu, S., & Prasanna, S. (2016). Status and outlook of sensitizers/dyes used in dye sensitized solar cells (DSSC): a review. *International Journal of Energy Research*, *40*(10), 1303–1320.

Sharma, K., Sharma, V., & Sharma, S. S. (2018). Dye-Sensitized Solar Cells: Fundamentals and Current Status. *Nanoscale Research Letters*, *13*(1), 381.

Shih, Y. C., Chu, A. K., & Huang, W. Y. (2012). Hierarchical structured TiO_2 photoanodes for dye-sensitized solar cells. *Journal of Nanoscience and Nanotechnology*, *12*(4), 3070–3076.

Shivaraman, S., Barton, R. A., Yu, X., Alden, J., Herman, L., Chandrashekhar, M. S. V., Park, J., McEuen, P. L., Parpia, J. M., Craighead, H. G., & Spencer, M. G. (2009). Free-standing epitaxial graphene. *Nano Letters*, *9*(9), 3100–3105.

Shmavonyan, G., Sevoyan, G., & Aroutiounian, V. (2013). Enlarging the surface area of monolayer graphene synthesized by mechanical exfoliation. *Armenian Journal of Physics*, *6*(1), 1-6.

Shockley, W., & Queisser, H. J. (1961). Detailed balance limit of efficiency of p-n junction solar cells. *Journal of Applied Physics*, *32*(3), 510–519.

Siegel, J., Kvítek, O., Ulbrich, P., Kolská, Z., Slepička, P., & Švorčík, V. (2012). Progressive approach for metal nanoparticle synthesis. *Materials Letters*, *89*, 47–50.

Sigma-Aldrich. (2016). *Gold Nanoparticles : Properties and Applications*. Sigma Aldrich.Retrieved from: http://www.sigmaaldrich.com/materials-science/nanomaterials/gold-nanoparticles.html.

Skulason, H. S., Gaskell, P. E., & Szkopek, T. (2010). Optical reflection and transmission properties of exfoliated graphite from a graphene monolayer to several hundred graphene layers. *Nanotechnology*, *21*(29), 295709.

Slepička, P., Kasálková, N. S., Siegel, J., Kolská, Z., & Švorčík, V. (2020). Methods of gold and silver nanoparticles preparation. *Materials*, *13*(1), 1.

Smestad, G., Bignozzi, C., & Argazzi, R. (1994). Testing of dye sensitized TiO_2 solar cells I: Experimental photocurrent output and conversion efficiencies. *Solar Energy Materials and Solar Cells*, *32*(3), 259–272.

Snaith, H. J. (2010). Estimating the maximum attainable efficiency in dye-sensitized solar cells. *Advanced Functional Materials*, *20*(1), 13–19.

Sokolov, K., Chumanov, G., & Cotton, T. M. (1998). Enhancement of Molecular Fluorescence near the Surface of Colloidal Metal Films. *Analytical Chemistry*, *70*(18), 3898–3905.

Sood, A. K., Lund, I., Puri, Y. R., Efstathiadis, H., Haldar, P., Dhar, N. K., Lewis, J., … & Fritze, M. (2015). Review of Graphene Technology and Its Applications for Electronic Devices. *International Journal of Engineering Research and Technology*, *8*(2), 125-141.

Stauber, T., Peres, N. M. R. R., & Geim, A. K. (2008). Optical conductivity of graphene in the visible region of the spectrum. *Physical Review B - Condensed Matter and Materials Physics*, *78*(8), 085432.

Subtil Lacerda, J., & van den Bergh, J. C. J. M. (2016). Diversity in solar photovoltaic energy: Implications for innovation and policy. *Renewable and Sustainable Energy Reviews*, *54*, 331–340.

Sugano, Y., Sato, K., Fukata, N., & Hirakuri, K. (2017). Improved separation and collection of charge carriers in micro-pyramidal-structured silicon/PEDOT:PSS hybrid solar cells. *Energies*, *10*(4), 420.

Sun, S., Gao, L., & Liu, Y. (2010). Enhanced dye-sensitized solar cell using graphene- TiO_2 photoanode prepared by heterogeneous coagulation. *Applied Physics Letters*, *96*(8), 083113.

Sundaram, R. S., Steiner, M., Chiu, H. Y., Engel, M., Bol, A. A., Krupke, R., Burghard, M., Kern, K., & Avouris, P. (2011). The graphene-gold interface and its implications for nanoelectronics. *Nano Letters*, *11*(9), 3833–3837.

Suttiponparnit, K., Jiang, J., Sahu, M., Suvachittanont, S., Charinpanitkul, T., & Biswas, P. (2011). Role of Surface Area, Primary Particle Size, and Crystal Phase on Titanium Dioxide Nanoparticle Dispersion Properties. *Nanoscale Research Letters*, *6*(1), 1–8.

Swinehart, D. F. (1962). The Beer-Lambert law. *Journal of Chemical Education*, *39*(7), 333–335.

Tai, Q., & Zhao, X.-Z. (2014). Pt-free transparent counter electrodes for cost-effective bifacial dye-sensitized solar cells. *Journal of Materials Chemistry A*, *2*(33), 13207–13218.

Tang, S., Wang, H., Zhang, Y., Li, A., Xie, H., Liu, X., Liu, L., Li, T., Huang, F., Xie, X., & Jiang, M. (2013). Precisely aligned graphene grown on hexagonal boron nitride by catalyst free chemical vapor deposition. *Scientific Reports*, *3*(1), 2666.

Tang, Y. B., Lee, C. S., Xu, J., Liu, Z. T., Chen, Z. H., He, Z., Cao, Y. L., Yuan, G., Song, H., Chen, L., Luo, L., Cheng, H. M., Zhang, W. J., Bello, I., & Lee, S. T. (2010). Incorporation of graphenes in nanostructured TiO_2 films via molecular grafting for dye-sensitized solar cell application. *ACS Nano*, *4*(6), 3482–3488.

Taniguchi, N., & Others. (1974). On the basic concept of nanotechnology. *Proc. Intl. Conf. Prod. Eng. Tokyo, Part II, Japan Society of Precision Engineering* (18–23).

Thanh, N. T. K., Maclean, N., & Mahiddine, S. (2014). Mechanisms of nucleation and growth of nanoparticles in solution. *Chemical Reviews*, *114*(15), 7610–7630.

Thavasi, V., Renugopalakrishnan, V., Jose, R., & Ramakrishna, S. (2009). Controlled electron injection and transport at materials interfaces in dye sensitized solar cells. *Materials Science and Engineering R: Reports*, *63*(3), 81–99.

Trügler, A. (2016). *Optical Properties of Metallic Nanoparticles: Basic Principles and Simulation*. Switzerland: Springer.

Turkevich, J. (1985). Colloidal gold. Part I - Historical and preparative aspects, morphology and structure. *Gold Bulletin*, *18*(3), 86–91.

Turkevich, J., Stevenson, P. C., & Hillier, J. (1951). A study of the nucleation and growth processes in the synthesis of colloidal gold. *Discussions of the Faraday Society*, *11*, 55–75.

Tyas, L. K., Suryana, R., Nurosyid, F., & Ilahi, N. A. (2017). Comparison of Titanium Dioxide (TiO_2) nanoparticle-nanofiber and nanofiber-nanoparticle on the application of dye-sensitized solar cell (DSSC). *Journal of Physics: Conference Series*, *795*(1), 012019.

Umale, S. V, Tambat, S. N., Sudhakar, V., Sontakke, S. M., & Krishnamoorthy, K. (2017). Fabrication, characterization and comparison of DSSC using anatase TiO_2 synthesized by various methods. *Advanced Powder Technology*, *28*(11), 2859–2864.

Velázquez-Martínez, S., Silva-Martínez, S., Jiménez-González, A. E., & Maldonado Álvarez, A. (2019). Synthesis of Mesoporous TiO_2 Spheres via the Solvothermal Process and Its Application in the Development of DSSC. *Advances in Materials Science and Engineering*, *2019*, 724-730.

Wallace, P. R. (1947). The band theory of graphite. *Physical Review*, *71*(9), 622.

Wang, J. T. W., Ball, J. M., Barea, E. M., Abate, A., Alexander-Webber, J. A., Huang, J., Saliba, M., Mora-Sero, I., Bisquert, J., Snaith, H. J., & Nicholas, R. J. (2014). Low-temperature processed electron collection layers of graphene/TiO_2 nanocomposites in thin film perovskite solar cells. *Nano Letters*, *14*(2), 724-730.

Wang, X., Christopher, J. W., & Swan, A. K. (2017). 2D Raman band splitting in graphene: Charge screening and lifting of the K-point Kohn anomaly. *Scientific Reports*, *7*(1), 1–9.

Wang, Y., Ni, Z., Hu, H., Hao, Y., Wong, C. P., Yu, T., Thong, J. T. L., & Shen, Z. X. (2010). Gold on graphene as a substrate for surface enhanced Raman scattering study. *Applied Physics Letters*, *97*(16), 163111.

Wang, Y., Tanabe, Y., & Yagyu, H. (2018). Analysis of Synthesis Mechanism of Gold Nanoparticles Using Glass Microfluidics. *Multidisciplinary Digital Publishing Institute Proceedings*, *2*(13), 702.

Wang, Y. Y., Ni, Z. H., Yu, T., Shen, Z. X., Wang, H. M., Wu, Y. H., Chen, W., & Wee, A. T. S. (2008). Raman studies of monolayer graphene: The substrate effect. *Journal of Physical Chemistry C*, *112*(29), 10637–10640.

Wang, Y., Zhen, S. J., Zhang, Y., Li, Y. F., & Huang, C. Z. (2011). Facile fabrication of metal nanoparticle/graphene oxide hybrids: A new strategy to directly illuminate graphene for optical imaging. *Journal of Physical Chemistry C*, *115*(26), 12815–12821.

Wang, Yanan, Zhou, V., Xie, Y., Zheng, X.-Q., & Feng, P. X.-L. (2019). Optical contrast signatures of hexagonal boron nitride on a device platform. *Optical Materials Express*, *9*(3), 1223–1232.

Wang, Z., Zhang, J., Yin, Z., Wu, S., Mandler, D., & Zhang, H. (2012). Fabrication of nanoelectrode ensembles by electrodeposition of Au nanoparticles on single-layer graphene oxide sheets. *Nanoscale*, *4*(8), 2728–2733.

Watkins, P. K., Walker, A. B., & Verschoor, G. L. B. (2005). Dynamical monte carlo modelling of organic solar cells: The dependence of internal quantum efficiency on morphology. *Nano Letters*, *5*(9), 1814–1818.

Weerasinghe, H. C., Huang, F., & Cheng, Y. B. (2013). Fabrication of flexible dye sensitized solar cells on plastic substrates. *Nano Energy*, *2*(2), 174-189.

Wei, N., Cui, H., Song, Q., Zhang, L., Song, X., Wang, K., Zhang, Y., Li, J., Wen, J., & Tian, J. (2016). Ag_2O nanoparticle/TiO_2 nanobelt heterostructures with remarkable photo-response and photocatalytic properties under UV, visible and near-infrared irradiation. *Applied Catalysis B: Environmental*, *198*, 83-90

Wenham, S. R., Green, M. A., Watt, M. E., & Corkish, R. (2013). Applied photovoltaics, second edition. In *Applied Photovoltaics, Second Edition*, Taylor and Francis, *9781849770491*, 1-323.

Willets, K. A., & Van Duyne, R. P. (2007). Localized Surface Plasmon Resonance Spectroscopy and Sensing. *Annual Review of Physical Chemistry*, *58*(1), 267–297.

Winzer, T., Knorr, A., & Malic, E. (2010). Carrier multiplication in graphene. *Nano Letters*, *10*(12), 4839–4843.

Wu, Jiang Bin, Lin, M. L., Cong, X., Liu, H. N., & Tan, P. H. (2018). Raman spectroscopy of graphene-based materials and its applications in related devices. *Chemical Society Reviews*, *47*(5), 1822–1873.

Wu, J, Lan, Z., Hao, S., Li, P., Lin, J., & Huang, M. (2008). Progress on the electrolytes for dye-sensitized solar cells. *Pure and Applied Chemistry*, *80*(11), 2241–2258.

Wu, Jihuai, Lan, Z., Lin, J., Huang, M., Huang, Y., Fan, L., Luo, G., Lin, Y., Xie, Y., & Wei, Y. (2017). Counter electrodes in dye-sensitized solar cells. *Chemical Society Reviews*, *46*(19), 5975–6023.

Wu, Jihuai, Li, Y., Tang, Q., Yue, G., Lin, J., Huang, M., & Meng, L. (2014). Bifacial dye-sensitized solar cells: A strategy to enhance overall efficiency based on transparent polyaniline electrode. *Scientific Reports*, *4*(1), 4028.

Wuithschick, M., Birnbaum, A., Witte, S., Sztucki, M., Vainio, U., Pinna, N., Rademann, K., Emmerling, F., Kraehnert, R., & Polte, J. (2015). Turkevich in New Robes: Key Questions Answered for the Most Common Gold Nanoparticle Synthesis. *ACS Nano*, *9*(7), 7052-7071.

Xu, K., Cao, P., & Heath, J. R. (2009). Scanning tunneling microscopy characterization of the electrical properties of wrinkles in exfoliated graphene monolayers. *Nano Letters*, *9*(12), 4446–4451.

Xu, Q., Gu, S. X., Jin, L., Zhou, Y. E., Yang, Z., Wang, W., & Hu, X. (2014). Graphene/polyaniline/gold nanoparticles nanocomposite for the direct electron transfer of glucose oxidase and glucose biosensing. *Sensors and Actuators, B: Chemical*, *190*, 562–569.

Xu, X., Caswell, K. K., Tucker, E., Kabisatpathy, S., Brodhacker, K. L., & Scrivens, W. A. (2007). Size and shape separation of gold nanoparticles with preparative gel electrophoresis. *Journal of Chromatography A*, *1167*(1), 35-41.

Yang, N. (2017). The Preparation of Nano Composites and Their Applications in Solar Energy Conversion. *Springer Theses*, *53*(9).

Yang, N., Zhai, J., Wang, D., Chen, Y., & Jiang, L. (2010). Two-dimensional graphene bridges enhanced photoinduced charge transport in dye-sensitized solar cells. *ACS Nano*, *4*(2), 887–894.

Yang, Y. C., Wang, C. H., Hwu, Y. K., & Je, J. H. (2006). Synchrotron X-ray synthesis of colloidal gold particles for drug delivery. *Materials Chemistry and Physics*, *100*(1), 72–76.

Yang, Y., Qiang, Y. H., Song, J., Xing, Z., & Song, C. B. (2015). Enhanced charge-transfer performance of photoelectrode based on interface modification in dye-sensitized solar cells. *International Journal of Electrochemical Science*, *10*(7), 5479-5487.

Yao, G. Y., Liu, Q. L., & Zhao, Z. Y. (2018). Studied localized surface plasmon resonance effects of au nanoparticles on TIO_2 by FDTD simulations. *Catalysts*, *8*(6), 236.

Ye, M., Wen, X., Wang, M., Iocozzia, J., Zhang, N., Lin, C., & Lin, Z. (2015). Recent advances in dye-sensitized solar cells: From photoanodes, sensitizers and electrolytes to counter electrodes. *Materials Today*, *18*(3), 155–162.

Yella, A., Lee, H. W., Tsao, H. N., Yi, C., Chandiran, A. K., Nazeeruddin, M. K., Diau, E. W. G., … & Grätzel, M. (2011). Porphyrin-sensitized solar cells with cobalt (II/III)-based redox electrolyte exceed 12 percent efficiency. *Science*, *334*(6056), 629–634.

Yen, M.-Y., Teng, C.-C., Hsiao, M.-C., Liu, P.-I., Chuang, W.-P., Ma, C.-C. M., Hsieh, C.-K., … & Tsai, C.-H. (2011). Platinum nanoparticles/graphene composite catalyst as a novel composite counter electrode for high performance dye-sensitized solar cells. *Journal of Materials Chemistry*, *21*(34), 12880.

Yu, S. Y., Chen, Y. J., & Liaw, J. W. (2015). Faraday-Tyndall effect of gold colloids. *4th International Symposium on Next-Generation Electronics, IEEE ISNE* 2015, 1–3.

Yue, G., Wu, J., Xiao, Y., Huang, M., Lin, J., Fan, L., & Lan, Z. (2013). Platinum/graphene hybrid film as a counter electrode for dye-sensitized solar cells. *Electrochimica Acta*, *92*, 64–70.

Zanetti-Ramos, B. G., Fritzen-Garcia, M. B., de Oliveira, C. S., Pasa, A. A., Soldi, V., Borsali, R., & Creczynski-Pasa, T. B. (2009). Dynamic light scattering and atomic force microscopy techniques for size determination of polyurethane nanoparticles. *Materials Science and Engineering: C*, *29*(2), 638–640.

Zayat, M., Garcia-Parejo, P., & Levy, D. (2007). Preventing UV-light damage of light sensitive materials using a highly protective UV-absorbing coating. *Chemical Society Reviews*, *36*(8), 1270.

Zeng, H., Long, M. Q., Ori, O., Putz, M. V., & De Sousa, J. S. (2015). Computational Modeling of Physical and Chemical Properties of Nanomaterials. *Journal of Nanomaterials*, 2015, 1–2.

Zhang, S. (2018). *Study of fluorine-doped tin oxide (FTO) thin films for photovoltaics applications*. Unpublished PhD Dissertation, Grenoble Alpes: Universite Grenoble Alpes.

Zhang, X., Chen, Y. L., Liu, R. S., & Tsai, D. P. (2013). Plasmonic photocatalysis. *Reports on Progress in Physics*, *76*(4), 046401.

Zhang, Z., Ito, S., O'Regan, B., Kuang, D., Zakeeruddin, S. M., Liska, P., Charvet, R., … & Péchy, P. (2007). The electronic role of the TiO_2 light-scattering layer in dye-sensitized solar cells. *Zeitschrift Für Physikalische Chemie*, *221*(3), 319–327.

Zhao, X. (2018). *Mechanical Properties of Graphene and Graphene-based Nanocomposites*. Unpublished PhD dissertation, UK: The University of Manchester.

Zheng, T., Bott, S., & Huo, Q. (2016). Techniques for accurate sizing of gold nanoparticles using dynamic light scattering with particular application to chemical and biological sensing based on aggregate formation. *ACS Applied Materials & Interfaces*, *8*(33), 21585–21594.

Zhu, H., Wei, J., Wang, K., & Wu, D. (2009). Applications of carbon materials in photovoltaic solar cells. *Solar Energy Materials and Solar Cells*, *93*(9), 1461–1470.

Zuber, A., Purdey, M., Schartner, E., Forbes, C., Van der Hoek, B., Giles, D., Abell, A., Monro, T., & Ebendorff-Heidepriem, H. (2016). Detection of gold nanoparticles with different sizes using absorption and fluorescence based method. *Sensors and Actuators B: Chemical*, *227*, 117–127.

APPENDICES

Appendix I: HOPG module used in graphene exfoliation

Appendix II: J-V measurement set up in a dark room